Transient engine simulations using the stochastic reactor model for driving cycle performance studies

Reddy Babu Siddareddy, MSc

A dissertation submitted to the
Department of Thermal Technology of Silesian University of Technology
for the degree of Doctor of Engineering

Academic Supervisor
Prof. dr hab. inż. Wojciech Adamczyk

Industry Supervisor
dr inż. Michał Pasternak

September 2025

Abstract

Optimising existing internal combustion (IC) engines remains a key engineering priority in the areas of fuel economy, utilisation of alternative fuels, and exhaust emissions reduction as the emission standards continue to become stringent worldwide. The optimisation of IC engines requires the evaluation of their performance parameters and exhaust emissions under transient conditions as found during actual driving cycles. However, physical testing on test benches is both costly and time-consuming, creating a need for reliable, real-time simulation tools supporting the development of modern IC engines.

This work introduces a simulation toolchain framework for real-time transient engine simulations. The toolchain integrates a 0D Stochastic Reactor Model (SRM) with tabulated chemistry into Model-in-the-Loop (MiL) and Hardware-in-the-Loop (HiL) platforms using the Functional Mock-up Interface (FMI) standard. By encapsulating the SRM within a Functional Mock-up Unit (FMU), the framework enables cross-platform simulations, bridging the gap between physical modelling accuracy and practical applicability in engine development workflows. The developed toolchain enables real-time transient engine simulations in MiL/HiL platforms and in stand-alone mode, and is considered a physics-based driving cycle simulator. It can simulate engine-out emissions and performance parameters under driving cycles such as the Worldwide harmonised Light vehicles Test Procedure (WLTP) and the Non-Road Transient Cycle (NRTC). Through the use of an Artificial Neural Network (ANN)-based meta-model of the driving cycle simulator, the computational cost of simulations has been reduced well below real-time, while maintaining the accuracy of the physics-based model. The FMU-based structure allows seamless integration with different models of exhaust after-treatment systems, enabling full-path simulation from combustion to tailpipe emissions.

The toolchain was applied in both stand-alone mode and integrated MiL/HiL environments for Compression-Ignition (CI) and Spark-Ignition (SI) engines under transient driving conditions of WLTP and NRTC. The investigations for SI engines focused on simulating engine performance parameters and exhaust emissions during the cold-start phase of the driving cycle for engines fuelled with compressed natural gas. Applications for CI engines dealt with predicting driving-cycle to driving-cycle variability in exhaust emissions, including CO_2, NO_x, soot, unburned hydrocarbons and CO. The toolchain's application in MiL and HiL configurations was validated on the dSPACE system and demonstrated seamless integration into real-time development environments. The capability of co-simulation with after-treatment models was verified based on the coupling with a selective catalytic reduction catalyst model applied to simulating an ammonia–biodiesel-fuelled engine. Overall, results obtained from different applications indicate the strength and versatility of the toolchain developed for studying engine behaviour under transient conditions, where details of emissions formation and fuel effects are of importance. The developed tool can be applied for engine certification studies or calibration and further contribute to the development of virtual test benches or digital twins in both research and industrial contexts.

Contents

Chapter 1

Introduction

1.1 Background and motivation

In recent years, stricter emissions regulations and the push for hybrid and fully Electric Vehicles (EVs) have led to a significant decline in research, development, and funding for Internal Combustion (IC) engines. While EVs are expected to dominate most performance market segments, substantial heavy-duty applications, such as trucks, buses, freight vehicles, and agricultural machines, remain that necessitate high-energy density and extended ranges [1, 2]. Therefore, efforts to enhance the efficiency of existing engine technologies will continue. As we advance toward sustainable mobility, these efforts prioritise fuel efficiency, reduction of exhaust emissions, and increase the use of alternative low-carbon fuels, such as ammonia and alcohol-based fuels [3, 4]. Achieving efficient optimisation of modern IC engines usually requires extensive testing to evaluate a variety of operating strategies. This, when performed on test benches, is both costly and time-consuming, creating a need for reliable numerical tools that support the development process of IC engines. Such tools empower researchers and engineers to explore new combustion strategies, fuel injection systems, and after-treatment technologies, thus enabling the development of cleaner and more efficient IC engines. The knowledge from simulations is then vital for enhancing control strategies that ensure compliant engine operation, regular, effective, and safe, particularly in relation to actual driving conditions.

The combustion engine of a modern vehicle is mostly operated under transient conditions, such as cold starts, idling in traffic or driving on highways, which involve engine acceleration, deceleration, gear shifts, and load changes. Such time-varied or transient conditions are, for the purpose of vehicle certification, mimicked by different types of driving procedures such as the Worldwide harmonised Light vehicles Test Procedure (WLTP) [5] or the Non-Road Transient Cycle (NRTC) [6]. Accurate modelling and simulation of time-varying operating conditions during the transient driving cycle is essential to accurately predict the combustion progress and pollutant formation during real-world scenarios.

Because of the demand for low computational cost, numerical models for transient engine simulations frequently employ Mean Value Engine Models (MVEMs). These often rely on average or simplified assumptions that do not accurately reflect the complex, dynamic, and non-linear combustion and emission processes during transient events. This limitation hampers the ability to predict transient emissions and performance effectively, which is necessary for advanced engine control strategies aimed at meeting increasingly stringent emission standards and fuel economy regulations across a variety of driving cycles. For these reasons, more robust methods are needed, which, however, must still be computationally efficient to allow for an effective application during engine development. The Stochastic Reactor Model (SRM) of engine in-cylinder processes appears as a modelling approach suitable for fulfilling this objective.

The SRM is a zero-dimensional (0D) model of in-cylinder processes of IC engines. It assumes the gas inside the cylinder is represented as a group of notional particles. There can be a few hundred such particles, and each of them has a chemical composition, temperature, and mass, so each particle represents a point for species mass fraction and temperature. The particles can mix with each other and interact with the cylinder walls. The particle-based representation of the flow inside the cylinder (see, Probability Density Function (PDF) method for turbulent reactive flows [7]) allows for direct solving of reaction kinetics without approximation, which is beneficial for predicting pollutant formation. In turn, the mixing process between particles must be modelled to mimic the action of turbulence as occurs in actual engines. By introducing randomness to the mixing process, particles acquire different compositions and temperatures, mimicking the mixture inhomogeneity found in real-world engines. Besides mixing and chemical reactions, the particles are subjected to remaining engine cycle processes such as volume changes due to piston motion, heat transfer, and fuel injection (see Section 3.2). The particle-based formulation and stochastic mixing, along with the use of detailed reaction kinetics, are unique features of the SRM compared to classical 0D models of engine in-cylinder processes, which frequently use simplified models of pollutant formation and differentiate between up to a few zones. The effectiveness of the SRM has been demonstrated in various engine studies, including combustion in Reactivity Controlled Compression Ignition (RCCI), Spark-Ignition (SI), and Compression-Ignition (CI) [8, 9] engines [10, 11]. In particular,[8] introduced and validated a tabulated chemistry solver within the SRM framework, demonstrating accurate prediction of combustion and emission characteristics under diesel conditions, while achieving substantial reductions in computational time. In [12], the SRM approach was employed to model advanced diesel combustion, successfully capturing transient phenomena and enabling predictive calibration across varying engine operating conditions. Meanwhile, [13] utilised SRM for direct-injection engines to simulate diesel engine behaviour across a range of operating points, incorporating a genetic algorithm to optimise mixing time and align with experimental pressure data. Their findings affirmed that SRM can replicate turbulent mixing effects and enhance predictive accuracy for engine states beyond those used in model calibration. In [14], the 0D SRM was applied to capture cycle-to-cycle variations in SI engines.

The existing applications of the SRM dealt with simulations under steady-state conditions. However, the results obtained indicate that the SRM could also be relevant for studying engine operation under transient conditions. In the context of transient engine simulations, it is of interest not only to simulate engine in-cylinder processes alone but also to simulate the behaviour of the complete engine powertrain, with exhaust aftertreatment, to allow for developing engine control strategies or simulations that closely mimic conditions during actual vehicle testing for certification purposes. Such a capability can be reached by integrating the SRM with Model-in-the-Loop (MiL) or Hardware-in-the-Loop (HiL) simulation platforms.

MiL refers to a model representation of physical systems in a software form. With regard to combustion engines, MiL testing typically involves validating engine control algorithms against detailed engine simulation models before any physical hardware is introduced. This method is important for transient engine simulations, since it allows control strategies to be developed and refined under transient operating conditions, all within a safe and fully virtual environment [15, 16]. In turn, HiL refers to a system representing physical hardware, the Electronic Control Unit (ECU) and software models. With regard to combustion engines, HiL testing is a validation method where real engine control hardware is tested against simulation models running in real-time. For transient engine simulations, HiL provides a way of testing engine hardware and finding strengths and vulnerabilities when operating under transient conditions, without the need for a fully assembled test bench, ensuring that control units perform reliably under realistic operating conditions [17, 18].

To make MiL and HiL testing practical across diverse tools and techniques, a standardised way of packaging and exchanging models is required. This is achieved by employing the Functional Mock-up Interface (FMI) and Functional Mock-up Unit (FMU) technology. FMI / FMU provide modularity, interoperability, and reuse, which are crucial in MiL / HiL contexts where different teams or suppliers often develop subsystems using different tools. Because FMU encapsulates both the model (in a standard form) and, in the case of co-simulation, FMU, their solvers, they can be exchanged between tools without reimplementing the models [19, 20, 21]. On the performance/deployment side, FMI allow models to be run in real HiL setups with guarantees on timing, resource usage, and traceability. The published article [22] shows how a full model-based control workflow was used: high-level model via Modelica, then exported via FMU, then deployed on a production ECU, with successful validation in real conditions [20, 21, 23]. Also, techniques for co-simulation and state saving/restoring, error control in communication step sizes, and distributed simulation using FMU have been shown to maintain accuracy while reducing simulation time significantly, which is key for real-time HiL contexts.

Existing works and literature data indicate that, in different forms, IC engines will remain for some time, yet a key source of powering in utility vehicles and transportation [2]. Therefore, the work on their improvement continues and is targeted at improving their efficiency, reducing fuel consumption, thus CO_2, and exhaust emissions, and allowing fuel flexibility by using alternative low-carbon fuels. Achieving these targets can benefit from the application of numerical tools that enable transient engine simulations. Here, the use of a toolchain that would integrate the 0D SRM with MiL/HiL platforms via FMU technology appears promising because of the expected flexibility to work with different engines and fuels and in co-simulation with models for other components of vehicle systems. Furthermore, the 0D formulation of the SRM should enable a low computational cost while ensuring high accuracy of predicting pollutant formation due to the application of detailed reaction kinetics. Therefore, such an integrated toolchain should contribute to the development of cleaner and more efficient IC engine technologies, which is the motivation behind this work.

1.2 Problem statement and objectives

Despite effectively representing the combustion process of IC engines and accurately predicting exhaust emissions under steady-state conditions, the SRM has not been applied for the simulation of IC engines under transient operating conditions like those in WLTP or NTRC. Moreover, so far, the SRM has not conformed to FMI and FMU standards, which are essential for deploying them in control system environments like HiL and MiL. This interoperability gap, coupled with computational costs associated with using detailed reaction kinetics for combustion and pollutant formation, hampers the effectiveness of SRM in real-time simulations as demanded by HiL. Addressing these issues is crucial to unlocking the full potential of the SRM for comprehensive simulations under transient conditions. Regarding these gaps, the objective of this work is to develop a simulation toolchain that enables transient engine simulations based on the SRM technology. The framework should be designed for portability and adaptability in MiL and HiL environments, providing standard FMI/FMU interfaces for seamless integration into real-time workflows. This approach bridges the gap between physical accuracy and computational efficiency, making SRM simulations practical for contemporary engine testing, calibration, and virtual validation applications under transient conditions. The defined objective is graphically presented in Figure 1.1.

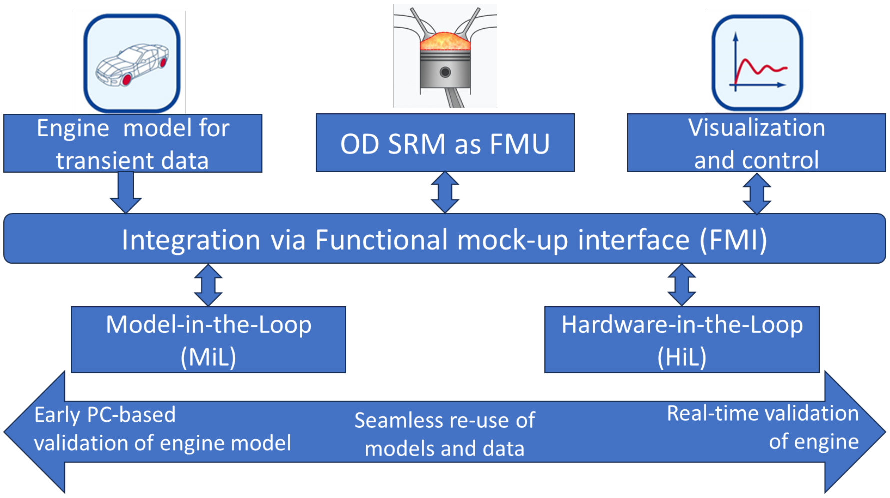

FIGURE 1.1: Concept of an integrated toolchain featuring 0D SRM, MiL/HiL, and FMI/FMU technology for transient driving cycle simulation studies.

To achieve the defined objective, the work focuses on the following specific technical goals.

- Develop FMU via FMI tailor-made for the SRM, to enable into into external simulation environments. The FMU encapsulates the SRM, allowing it's deployment within co-simulation platforms and real-time testing setups such as HiL and MiL. By adhering to the FMI specification, the framework ensures interoperability, modularity, and reusability across various simulation tools, thereby extending the applicability of the SRM beyond its native environment. The framework should allow the coupling of engine processes with the frameworks for exhaust aftertreatment to work as a co-simulation.

- Modify the existing SRM codebase to accommodate transient simulations by incorporating dynamic engine parameters such as speed, load, injection strategy, and valve timing that may vary during transient operation. Furthermore, design a framework to generate an FMU for the SRM using the FMI standard, including the necessary modifications to the SRM source code and the implementation of the FMI-compliant interface.

- Develop the capability to export the transient engine data simulation capable SRM for use with external simulation or power-train platforms, including MiL and HiL.

- Streamline the framework to minimise computational costs, ensuring real-time feasibility on stand-alone, MiL and HiL platforms while retaining combustion and emissions prediction capabilities of the SRM.

- Verify and validate the developed toolchain with reference models or experimental data to assess its capability to simulate engine performance parameters and exhaust emissions during transient operation and for both SI and CI engines, on MiL and HiL platforms, and in co-simulation with the aftertreatment system.

- Develop an Artificial Neural Network (ANN) based meta-model of the driving cycle simulator to allow for ultra-fast calculations that would eliminate restrictions resulting from the small time step of simulations in HiL applications.

Through these objectives, the research aims to bridge the gap between very accurate and detailed representation of a physical combustion modelling and practical real−time application in engine control development environments, ultimately contributing to improved engine performance, emissions compliance, and faster development cycles.

1.3 Structure of the thesis

This thesis is organised into the following five chapters, each addressing a specific aspect of the work. The content of the chapters is partially adopted from the already published works [24, 25, 26, 27].

- Chapter 1: Introduction. This chapter provides the background and motivation for transient engine simulations, identifies key challenges, states the problem, outlines the research objectives, and defines the scope and limitations of the work. A brief discussion of the research questions and the structure of the thesis is also included.
- Chapter 2: Literature review. In this chapter, the background and characteristics of transient engine simulation are discussed. It underlines the necessity of time accurate simulation tools in power-train development in transient, real-world driving situations. It provides an overview of the most recent state-of-the-art simulation techniques. A focused discussion on engine modelling across different dimensions (0D, 1D, 3D CFD) including trade-offs in accuracy, complexity and computational efficiency. Finally, the chapter reviews the use of the FMI/FMUs in the simulation workflows with a focus on automotive applications. It ends with MiL and HiL platforms, showcasing their involvement in the real-time validation, control development, and virtual calibration with the transient simulation model.
- Chapter 3: Methods and tools. This chapter describes the technical development of the simulation toolchain, which is build around the SRM, detailed chemistry for modelling combustion and emissions formation and FMU technology. This chapter also explains the design and implementation of the FMI/FMU export layer, as well as the interfacing of third-party systems such as MiL systems, and HiL platforms. The developed toolchain is presented in Section 3.8, where it is shown to result from the integration of

different sub models described in Sections 3.2 to 3.7 which is the main contribution of this work and enables transient real-time engine simulations, features which were not available earlier.

- Chapter 4: Results and discussion. This chapter presents verification and validation studies of the developed simulation framework. Case studies include diesel, Compressed Natural Gas (CNG), and gasoline engines operating under various transient driving cycles such as WLTP and NRTC. The chapter compares simulation results with reference data and demonstrates integration and real-time execution of the simulations on MiL and HiL platforms.
- Chapter 5: Summary. This chapter summarizes the key contributions of the work, highlights the findings, and discusses the implications for transient engine simulation and control development. Suggestions for future research and potential enhancements are also provided.

Chapter 2

Literature review

2.1 Background

To comply with vehicle certification regarding exhaust emissions, IC engines must be tested and optimised for the application under transient operating conditions that occur in real-world scenarios. This facilitates engineers' and developers' use of simulation techniques, allowing a more realistic representation of engine behaviour during a transient run, which is usually represented by driving cycle models such as the WLTP [28]. Accurately performing transient engine simulations presents several technical challenges. One major issue is the complexity of engine subsystems and their physical processes, with frequently non-linear interactions. Components such as turbochargers, EGR systems, intake throttles, and variable valve timing mechanisms interact in ways that require high-fidelity models with fine temporal resolution. These interactions often involve delays and feedback loops that must be resolved over small time steps to maintain numerical stability and physical accuracy [29]. Simulating complete engine systems requires capturing the relevant physical processes behind the engine system components. In addition to physical modelling challenges, transient simulations must also meet real-time computational constraints, especially when used in MiL or HiL environments. These applications require asynchronous execution to balance solver performance with input/output demands. Maintaining chemical and thermodynamic fidelity while achieving real-time performance is a persistent challenge. To address this, researchers have developed different simulation techniques, which reduce computational load while preserving the essential physics of simulated processes.

This chapter provides a brief overview of commonly used simulation tools and techniques in the context of their application for driving cycle simulation studies. The first part of the chapter reviews models for simulating engine in-cylinder processes. Next, simulations employing FMI/FMU technology are presented, followed by a presentation of MiL/HiL environments.

2.2 Engine modelling

Modelling of in-cylinder processes became a basis in modern powertrain development to understand, predict, and optimise IC engines' performance parameters and pollutant formation under transient conditions. The engine models vary in dimensionality, complexity, and fundamental methodology of simulations, spanning from physics-based techniques to data-driven algorithms. Each type of model achieves certain objectives, balancing tradeoffs among computing efficiency, accuracy, and the complexity of the model. These models are frequently classified based on the dimensionality criterion. Here, one can distinguish between zero-dimensional, One-Dimensional (1D), Quasi-Dimensional (QD) and multidimensional, referred to frequently as Three-Dimensional (3D) Computational Fluid Dynamics (CFD). Furthermore, from the point of view of application for transient simulations, one can also list empirical and data-driven models, and ANN models.

0D models

The 0D engine models rely on conservation laws of mass and energy without resolving spatial variations of in-cylinder processes. Typically, they simulate average thermodynamic properties over engine cycles, which makes them particularly suitable for systems-level simulation and real-time applications [30, 31]. They are also preferred for Model Predictive Control (MPC) and virtual calibration applications, where a balance between accuracy and simulation speed is desired [30, 32]. The primary advantages of OD engine models include their low computational cost and simplicity of implementation.

The SRM-based approach, introduced in Section 1.1, also belongs to the family of 0D models. However, though being 0D, the SRM enables capturing the effects of turbulence and mixture inhomogeneity in composition and temperature that are found in actual engines. These are the features usually not offered by other 0D-based models. 0D SRM models have been successfully applied to study CI and SI engines [12, 13, 33, 34, 11]. For SI engines, the versatility of SRM has been demonstrated by [14], by evaluating knock tendency and Cycle-to-Cycle Variability (CCV). When employing the tabulated chemistry approach [33] in simulating combustion and emissions formation, they, besides high accuracy of results, demonstrated also high computational efficiency. This feature makes them an attractive modelling approach for applying to transient simulations and real-time, potentially.

Multidimensional models

0D models are computationally efficient and simple to use, but cannot describe spatial gradients of in-cylinder properties. 1D, QD and 3D CFD models, collectively denoted here as multidimensional ones, help to overcome these limitations by modelling in-cylinder processes in a more detailed manner, by taking into account, in different levels of detail, complex combustion physics, turbulence, heat transfer, spray dynamics and chemical kinetics, lame propagation, and pollutant formation [35, 36, 37], which can help in examining the geometric sensitivities [35, 36, 37]. The multidimensional modelling (usually 3D CFD) is a compromise that trades off speed for accuracy when the simulation goal requires high-resolution, physically detailed results [38, 39]. n turn, 1D models are essential in IC engine simulations for balancing physical accuracy with computational efficiency [35, 36]. Their ability to resolve wave dynamics and chemical reactions makes them well-suited for predicting engine performance under transient conditions.

Empirical and data-driven models

The empirical engine modelling refers to a generic approach, where models are created based on experimental data. Usually, these methodologies utilise large experimental measurement data, via classical machine learning methods and regression-based approaches to learn complex data relationships, providing methods for fast prediction, where physical modelling is impractical [40]. Traditional empirical methods, such as performance mapping and inverse heat release techniques, enable quick predictions at the component level but are limited to calibrated data, with no reliable predictions for data outside the calibrated data [41].

ANN models

In contrast to empirical and data driven models, ANNs, Support Vector Machines (SVMs), Recurrent Neural Networks (RNNs), and Online Deep Learning (ODL), can learn non-linear relationships, proving effective for transient emissions [36, 42]. Among these, ANN models are inspired by the working of a biological neuron, which enables it to learn the complex relationships between data. ANNs are applied to learn non-linear interactions among combustion dynamics, air-path behaviour, and control systems, including effects such as EGR feedback on intake pressure and oxygen concentration [41, 43, 44]. ANN models requires substantially large data and multiple test case scenarios to learn the patterns [36, 42]. Secondary response models such as RNNs, a variant of ANNs can help to improve temporal learning though it requires careful tuning to prevent over-fitting and to generalize the predictive model [45, 46]. When incorporated into hybrid models combined with physics-based and empirical models into ANN enables online recalibration and control tuning, for example by MPC under the transient conditions [47].

2.3 FMI/FMU

Definition and purpose

While numerical tools for the simulation of engine in-cylinder processes offer representations of the engine working cycle performance, they usually do not facilitate system-level integration. To allow for testing and development across different control systems, vehicle dynamics, and embedded hardware, a standardised interface is needed. To fill this gap, the FMI and, more specifically, its implementation as a real-time FMU, provide a solution to encapsulate engine models in portable units. This enables simulation tools to communicate and work in cooperation, providing real-time capabilities in MiL and HiL platforms. The subsequent paragraphs and sections introduce FMI/FMU and show how it interconnects the engine models with full system validation platforms.

The FMI is a standard that allows engineers and developers to share and run dynamic system models among different software tools. It supports two main ways of using these models: one where the integrated tool handles all calculations, called model exchange, and another where the model carries its own solver, called co-simulation. This flexibility of FMI helps teams work together across platforms without relying on a single proprietary system [48]. FMU is an archive that follows the FMI standard and can be imported into simulation environments for integration with third-party tools for simulations. An FMU typically includes three main components [48].

- A model description file (XML) detailing inputs, outputs and behaviour.
- Binary executables for different platforms.
- Optional source code to allow rebuilding and optional resources that may required by the executables for the simulations.

The purpose of FMI/FMU is multi-fold [48],

- It enables multiple engineers and developers share their developed simulation tool as FMU to integrate with other parts of the system without revealing intellectual property and sensitive details.
- Supports modular development, allowing reuse across design phases.
- Facilitates cross-domain integration.
- Promotes standardisation to reduce integration costs.

Integration with third party tools

The root of FMI's success is its tool-neutral architecture, allowing FMU to be created, imported, and simulated across a wide range of platforms. This flexibility supports both model exchange and co-simulation setups [49].

The binary executables for FMU can be generated by a variety of platforms such as Simulink, OpenModelica, and Dymola for control and physical systems, LabVIEW and SimulationX for instrumentation applications, Python and C++ via wrapper libraries such as FMILibrary or FMI++ for customized simulation software.

Simulations with FMUS became the industry standard. Platforms such as MATLAB/Simulink, dSPACE, SpeedGoat, Electrobit, IPG Automotive, and many others offer FMU integration [50].

Application in automotive systems

Automotive systems are increasingly complex and interdisciplinary, requiring reliable simulation frameworks. FMI/FMU offers a robust method for virtual prototyping, system validation, and early software testing. In automotive systems, the FMU standard finds application in a few main areas [51, 52].

- Virtual ECUs (VECUs): Automotive software can be tested against FMUs that mimic sensor or actuator behaviour, enabling early detection of integration issues.
- Vehicle Dynamics and advanced driver assistance systems: FMUs of mechanical subsystems (e.g., suspensions) are coupled with control models to analyse behaviour during manoeuvrers or emergency events.
- HIL and SIL Testing: FMUs are embedded in test benches to replicate subsystem responses, aiding verification of embedded control software.

2.4 MiL and HiL testing platforms

Definition and purpose

The integration tools and standards, such as FMI/FMU, provide the fundamental basis for modularity, interoperability and distributed simulation frameworks. In turn, the potential of the engine models and combustion solvers can be verified within the simulation-based testing platforms. Developers and engineers can easily integrate the models in testing platforms as modular components such as FMUs. The testing platforms are available under a broader term X-in-the-Loop (XiL), where X refers to a software, plant model, component-level control algorithm, hardware component as a model or hardware component itself. With the above-mentioned components and models, XiL is broadly classified into Software-in-the-Loop (SiL), Plant-in-the-Loop (PiL), MiL and HiL. Whereas SiL and PiL focuses on larger system level that represents a whole software or plant itself. This work focuses on developing a simulation toolchain framework for transient engine simulations aimed at engine development and optimization. So, in this work choses MiL and HiL as testing platforms, since engine-level studies naturally integrate within the larger vehicle system where SiL and PiL are typically applied at system level [53]. MiL is primarily used during the initial stages of development to ensure that control strategies behave as expected. HiL testing follows, bridging the gap between simulation and real-world testing by exposing the hardware to dynamic inputs and outputs from a virtual engine model. This layered approach reduces development time, cost, and risk, especially for complex systems like [54, 55].

Architecture and components

The architecture of MiL and HiL systems typically includes a controller model or hardware ECU, and a real-time simulation platform. In MiL, both the plant and controller are software models, often developed in software platforms like MATLAB/Simulink. In HiL, the controller is replaced with actual hardware, while the plant remains simulated [56]. Key components of a MiL setup include models representing the physical hardware, individual models' control algorithms, and system-level control algorithms. Key components of a HiL setup include a real-time simulator (e.g., dSPACE ASM models, NI VeriStand models), interface hardware for analogue or digital data and communication protocols, and a vehicle dynamics model representing engine behaviour. This modular architecture allows for flexible integration and iterative testing. For example [56] developed a modular ICE model for Engine Management Systems (EMS) verification using MiL and HiL, achieving high accuracy and stability in real-time simulations.

Application in engine development

MiL and HiL are instrumental in developing and validating EMS. MiL enables early testing of engine control algorithms and models. Once control algorithms and models are validated and verified, control algorithms implemented on ECUs and models will be replace by actual hardware in engines and tested under HiL environment to ensure control algorithms and hardware would work under transient conditions. This stage ensures both algorithm and hardware components interact as intended and work reliably under real-word scenarios [57, 58].

2.5 Summary

Transient engine simulation has become a vital tool in modern power-train development, enabling engineers to predict and optimise engine performance under transient, real-world conditions. 0D SRM with tabulated chemistry for combustion and pollutant formation strikes a valuable balance between computational speed and physical accuracy in simulating engine performance parameters and exhaust emissions. By utilising the FMI/FMU cross-platform integration capability, 0D SRM can be deployed within MiL and HiL testing environments. This integration supports real-time validation, controller development, and virtual calibration, ensuring reliable, accurate emissions simulations in real-time under transient driving cycle conditions.

Chapter 3

Methods and tools

3.1 Background

This chapter introduces the overall methodology followed in developing the simulation toolchain employing the SRM, which is appropriate for real-time applications and FMI/FMUbased integration for driving cycle simulation studies. The chapter is organised into modular development steps, starting with an overview of the SRM and tabulated chemistry approach for simulating combustion and pollutant formation. After that, aspects of integrating the SRM with FMU are presented. Next, the model's needs for transient driving cycle simulations are discussed based on WLTP and NRTC. Subsequently, the integration of the SRM with FMU technology into MiL/HiL frameworks is presented. This is followed by a presentation of the ANN-based meta-model of driving cycle simulation. Finally, the last section presents the complete toolchain resulting from the integration of different model components, which is a major contribution of this work.

3.2 The Stochastic Reactor Model (SRM)

The SRM is a zero-dimensional model of physical and chemical in-cylinder processes in IC engines. The SRM adopted for this study was previously validated in several published research works [10, 34, 11, 33, 59] that are the foundation of the description presented in this section. The description provides an overall concept of the SRM and its formulation that is followed by a presentation of key processes modelled, such as fuel injection, mixing, heat transfer, flame propagation (SI engines) and turbulence. The description of the turbulence is limited here to the model relevant for simulating SI engines. The presentation of the model for CI engines can be found in [12, 60, 61].

In the SRM, the gas within the cylinder is regarded as a collection of notional particles. The particles are allowed to interact by mixing with each other and exchanging heat with the walls of the cylinder. Each such notional particle is characterised by temperature, mass and species concentration. Thus, in a sense, each particle can be understood as a realisation of the flow at a certain time and location in the actual combustion chamber. The particles can mix with each other or exchange heat with the wall, which results in changes in their properties. Finally, the particles are subjected to chemical reactions according to the applied reaction mechanism. All the particle-based processes are calculated sequentially using an operator splitting loop method [24]. Mixing between particles is a modelled process, using different types of mixing models. The common feature of these models is the necessity of modelling the mixing time scale, which governs the frequency at which particles mix with each other and decides finally about mixture inhomogeneity [25].

A schematic visualisation of the SRM concept is shown in Figure 3.1 The upper and lower parts of the figure represent the operator splitting loop and particle-based representation of the in-cylinder mixture for CI and SI engines, respectively. Additionally, the QD-based flame propagation model for SI engines is presented along with an exemplary distribution of particle properties.

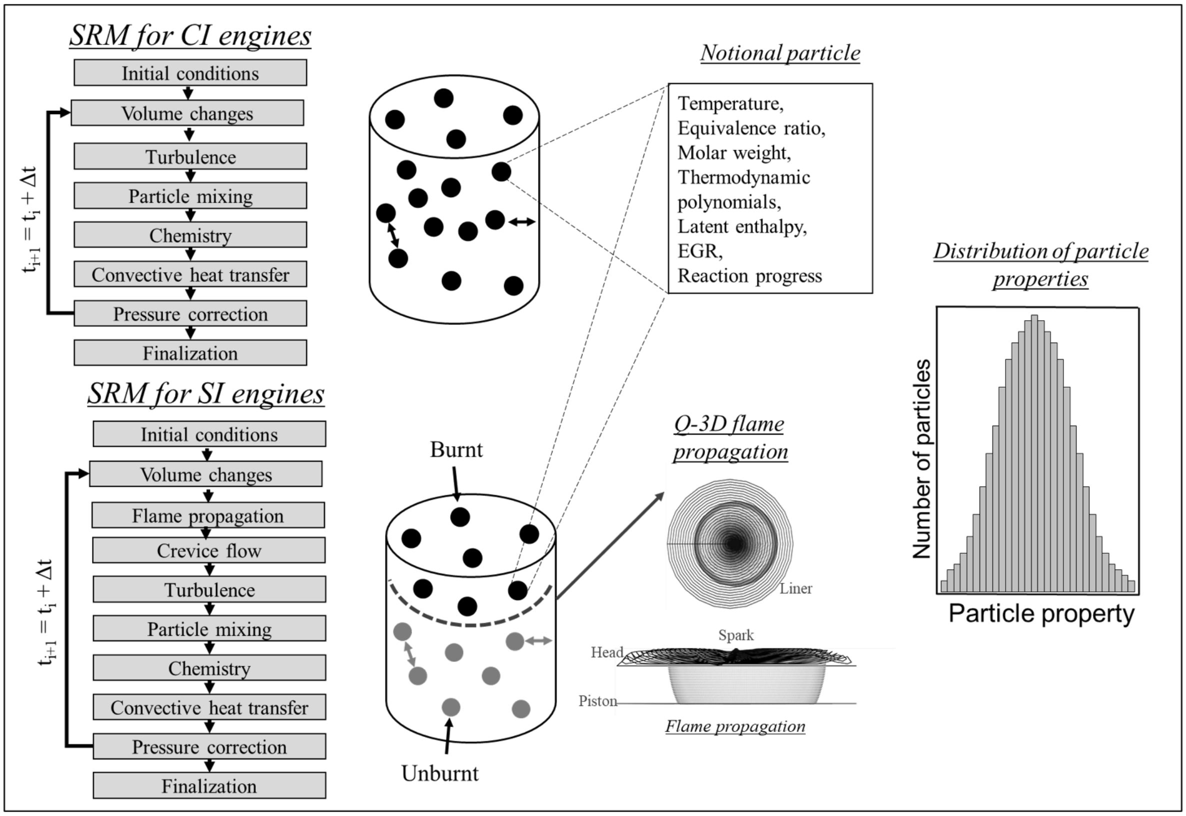

FIGURE 3.1: Schematic visualisation of the SRM concept for CI and SI engine processes [24].

3.2.1 Overall formulation

In the SRM, the temperature $T(t)$ and species concentrations $Y_i(t)$ are treated as random variables that can vary within the cylinder and determine the composition of the gas mixture using probability density function (PDF). The in-cylinder mixture is thus represented by a PDF in phase space, and the particles constitute the realisation of this distribution. In practice, all stochastic particles in the SRM represent a portion of the in-cylinder mass, and rather than a PDF, a mass density function (MDF) is used; the MDF can be considered as a mass-based discretisation of the PDF. The solution for the mass fractions and temperature is obtained from the transport equation for the MDF. These data are further used to calculate other engine quantities, such as pressure and heat release rate. The joint vector $\boldsymbol{\varphi}(t)$ of the local scalar variables is defined as

$$\boldsymbol{\varphi}(t) = (Y_1, \dots, Y_{N_S}, T; t) \equiv (\varphi_1, \dots, \varphi_{N_S}, \varphi_{N_S+1}; t), \tag{3.1}$$

where N_S denotes the number of chemical species involved in the reaction mechanism. The respective joint scalar MDF is given by

$$F_{\boldsymbol{\varphi}}(\boldsymbol{\psi}; t) = F_{\boldsymbol{\varphi}}(\psi_1, \dots, \psi_{N_S}, \psi_{N_S+1}; t). \tag{3.2}$$

In Equation 3.2, $\psi_1, \dots, \psi_{N_S}, \psi_{N_S+1}$ are realizations of the random variables $\varphi_1, \dots, \varphi_{N_S}, \varphi_{N_S+1}$. It is assumed that the scalar variables are statistically homogeneous, i.e., their probabilities do not depend on spatial position. This means that within the cylinder, the MDF is spatially constant. Following these assumptions, the evolution in time of the MDF is described by the following transport equation

$$\frac{\partial}{\partial t} F_{\boldsymbol{\varphi}}(\boldsymbol{\psi}, t) + \frac{\partial}{\partial \psi_i} \left(Q_i(\boldsymbol{\psi}) F_{\boldsymbol{\varphi}}(\boldsymbol{\psi}, t) \right) = \textit{mixing term}. \tag{3.3}$$

The terms in Equation 3.3 describe how the MDF varies in time depending on calculated engine in-cylinder processes, including chemical processes, convective heat loss, piston motion-induced volume changes, and fuel injection.

These terms are computed using the energy and species conservation equations, which for CI engines can be written as follows [62]

$$Q_i = \frac{W_i}{\rho} \sum_{j=1}^{N_R} \omega_{i,j} \frac{\dot{m}_f}{m} (Y_{i,f} - Y_i) \quad i = 1, \dots, N_{Species} \quad ; \quad j = 1, \dots, N_{Reactions}. \tag{3.4}$$

$$Q_{NS+1} + \frac{1}{\rho c_p} \frac{dp}{dt} + \frac{hgA}{mc_p}(T - T_W) - \frac{1}{c_p} \sum_{i=1}^{N_S} h_i W_i \sum_{j=1}^{N_R} \omega_{i,j} + \frac{1}{c_p \rho V} \sum_{i=1}^{N_S} \dot{m}_f Y_{i,f} (h_{i,f} - h_i). \tag{3.5}$$

In Equations 3.4 and 3.5, ω_{ij} and Y_i represent the molar formation rate and mass fraction of species i due to reaction j, respectively; subscript f denotes fuel-specific terms. W_i is the molar mass of species i, ρ the density, T the mean gas temperature, T_w the cylinder wall temperature, c_p the specific heat at constant pressure, h_g the heat transfer coefficient, A the wall area, h_i the species enthalpy, and p the pressure. N_R and N_S denote the number of reactions and species.

Global quantities, such as mass m, volume V, and pressure p are treated as spatially uniform. Volume is computed from engine geometry, while pressure follows the equation of state.

3.2.2 Fuel injection

In the code version used in this work, the injected fuel is assumed to vaporise immediately upon injection, meaning the injected rate corresponds to a vaporised rate. The energy for vaporisation is drawn from the surrounding gas, as a result of mixing. The amount of that gas/mixing mass is denoted by m_{mix}. New particles are added to the MDF, and the injected fuel alters the temperature and composition of existing particles via added source terms. The mixing mass is calculated assuming equal pressure between fuel and ambient gas [63, 64].

$$m_{\text{mix}} = m_f \cdot \frac{h_f^{\text{liq}}(T_f) - h_f^{\text{gas}}(T)}{h_m(T_u) - h_m(T_m)}. \tag{3.6}$$

Species-wise handling is performed for multi-component fuels, with final temperature T_u derived from fuel thermophysical data.The subscripts f and v denote fuel and vaporisation, respectively. If the fuel is a mixture of several species, each species is treated individually with respect to Equation 3.6, since each molecule has a specific vaporisation temperature. The final temperature of both the injected fuel and the mixing mass, after completion of the process, will be equal to the vaporisation temperature (T_v) at the given pressure. This temperature is determined from the liquid properties of the injected fuel, which are provided as input to the SRM [64].

3.2.3 Flame propagation

For SI engine simulations, a two-zone approach within the SRM is adopted for combustion modelling. Stochastic particles are divided into burnt and unburnt zones, with interactions restricted within each zone. The mass transfer from the unburnt to the burnt zone is governed by turbulent flame propagation, which can be described using empirical correlations, modelled by [65] as shown in Equation 3.7.

$$\frac{s_t}{s_l} = 1 + C\left(\frac{u'}{s_l}\right)^n . \tag{3.7}$$

An extended correlation proposed by [66] and implemented in SRM by [67], accounts for additional thermochemical effects expressed as in Equation 3.8.

$$\begin{aligned}\frac{s_t}{s_l} = \Bigg\{ &\left[b - a\left(1 + \left(\frac{u'}{s_l}\right)^{1.5}\left(\frac{\delta}{l}\right)^{0.5}\right)^{-0.4}\frac{(T_{ad} - T_u)\,\delta\,u'}{T_{ad}\,l\,s_l}\right] \\ &+ d\left[\left(\frac{u'}{s_l}\right)^2 + \left(\frac{\delta}{l}\right)^{-0.25}\left(\frac{u'}{s_l}\right)^{-2.25}\right]^{0.5}\Bigg\}.\end{aligned} \tag{3.8}$$

Both approaches (Equation 3.7 and Equation 3.8) propose a correlation between the turbulent s_t and the laminar flame speed s_t. The fluctuation of the turbulent velocity is noted as u' in both correlations. The constant C in equation 3.7 is a function of the turbulent length scale l_l and the laminar flame thickness δ_l. The model constant n in Equation 3.7 is tunable in the range [0.5 – 1.0]. In 3.8 T_u represents the unburned zone temperature and T_{ad} is the adiabatic flame temperature. All the other values in 3.8 are assigned by the user and their reference values are reported in Table 3.1 [65, 66].

TABLE 3.1: Default constants in the flame propagation model given by Equation 3.8.

Constant	**Symbol**	**Value**
Flame thickness ratio	δ	0.6
Thermal expansion coefficient	α	4.0
Empirical constant	b	0.665
Density ratio exponent	d	0.967
Model constant	C_m	1.654
Turbulence scaling factor	C_θ	0.7
Turbulent viscosity coefficient	–	0.09

The laminar flame speed s_l is precomputed and stored in a look-up table as a function of equivalence ratio ϕ, temperature, pressure, and EGR rate, using averaged properties of the unburnt zone. Spark initiation is modelled using a quasi-dimensional flame tracking approach, as described by [37], and illustrated in Figure 3.2, which shows the evolution of a spherical flame front applicable to both conventional and PPE configurations.

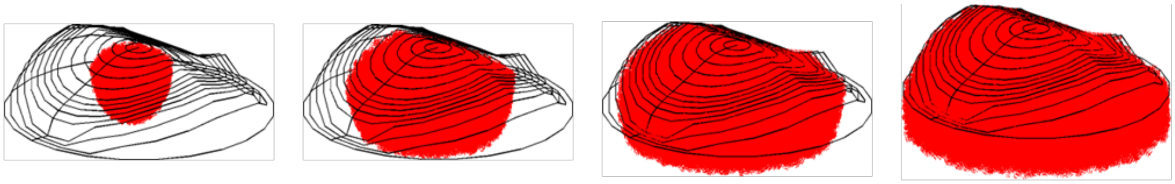

10 CAD aTDC 15 CAD aTDC 20 CAD aTDC 30 CAD aTDC

FIGURE 3.2: Exemplary evolution of the flame front simulated by the SRM [68]

3.2.4 Turbulence modelling

Turbulence models are used to compute the change in turbulent kinetic energy and then its dissipation, which is subsequently used to determine the mixing time that is the main modelled parameter for the SRM. There are a few models for calculating turbulent kinetic energy available for the SRM [63]. In this section, as an example, the K-ϵ turbulence model for simulating SI engine combustion is presented, which is based on the work reported in [69]. The model was used in the simulations presented in Section 4.5.

The model uses a series of differential terms that characterise the production and dissipation of k in a cylinder-shaped geometry with a tumble flow motion around the cylinder's cross-axis to compute the change of turbulent kinetic energy ($\frac{dK}{dt}$). Equation (3.9) lists the production terms for k as valve inflow, axial flow, tumble flow motion, direct injection, compressibility, and dissipation.

$$\begin{aligned}\frac{dk}{dt} = {} & \left(\frac{dk}{dt}\right)_{\text{valve}} + \left(\frac{dk}{dt}\right)_{\text{axial}} + \left(\frac{dk}{dt}\right)_{\text{tumble}} \\ & + \left(\frac{dk}{dt}\right)_{\text{direct injection}} + \left(\frac{dk}{dt}\right)_{\text{compressibility}} + \left(\frac{dk}{dt}\right)_{\text{dissipation}} .\end{aligned} \tag{3.9}$$

Equation (3.10) describes the change of angular momentum of the tumble flow motion L_{TF}. Inflow through the valves and spin-up from the piston's acceleration can both generate angular momentum. Shear forces and outflow from the system cause angular momentum to decay.

$$\begin{aligned}\frac{dL_{TF}}{dt} = {} & \left(\frac{dL_{TF}}{dt}\right)_{\text{valve inflow}} + \left(\frac{dL_{TF}}{dt}\right)_{\text{spin-up}} \\ & - \left(\frac{dL_{TF}}{dt}\right)_{\text{outflow}} - \left(\frac{dL_{TF}}{dt}\right)_{\text{shear}}\end{aligned} \tag{3.10}$$

In the above ρ is the gas density, D_C is the cylinder bore, H_S is the instantaneous height between the cylinder head and piston, and u is the turbulent viscosity.The contribution of tumble flow motion decay to production of turbulent kinetic energy k is described by Equation ((3.11)).

$$\left(\frac{dk}{dt}\right)_{\text{tumble}} = \frac{1}{1024} \cdot \frac{\rho \cdot L_{TF}^2 \cdot H_S^2}{D_C^4}. \tag{3.11}$$

Equation ((3.12)) is used to compute the turbulent viscosity ν_t based on turbulent kinetic energy and dissipation, where C_μ is modelled parameter with a default value of 0.09.

$$\nu_t = C_\mu \cdot \frac{k^2}{\varepsilon}. \tag{3.12}$$

The last term in Equation ((3.9)) characterises how dissipation ε destroys turbulent kinetic energy. Acording to [70] the dissipation is inversely related to the integral length scale L and proportionate to the turbulent kinetic energy k. Dissipation ε can therefore be calculated using Equation ((3.13)). Where C_ε is the model parameter and L denotes integral length scal-its's modelling is presented in [26, 60].

$$\varepsilon = C_\varepsilon \cdot \frac{k^{3/2}}{L}. \tag{3.13}$$

From the turbulent kinetic energy, the turbulence fluctuation u' is determined, which, along with the turbulent length scale l, enters the turbulent flame propagation model [26]. Furthermore, knowing k, l and ε the scalar mixing time τ_ϕ, which is main modelled parameter for the SRM, can be calculated according to Equation 3.14

$$\tau_\phi = C_\phi \cdot \left(\frac{k}{\varepsilon}\right), \tag{3.14}$$

where the constant C_ϕ relates the scalar mixing time τ_ϕ with the turbulent mixing time τ_t and can be adjusted parameter depending on the application.

3.2.5 Particle mixing

In this thesis particle mixing model used proposed by [71] and further improved by [72] is used. The model was implemented in [62] in the SRM code and updated to consider the particle weights $W_{(q)}$ and $W_{(p)}$ of the notional particles (q) and (p). As per [60] the calculation of the median of scalar ϕ of two randomly selected particles (q) and (p) is shown in Equation ((3.15)). The Curl mixing model implementation in SRM is investigated by [62, 73, 64]

$$\begin{aligned} \frac{d\phi_{(p)}(t)}{dt} &= \frac{W_{(q)} \cdot \phi_{(q)}(t) - W_{(p)} \cdot \phi_{(p)}(t)}{W_{(q)} + W_{(p)}}, \\ \frac{d\phi_{(q)}(t)}{dt} &= \frac{W_{(p)} \cdot \phi_{(p)}(t) - W_{(q)} \cdot \phi_{(q)}(t)}{W_{(q)} + W_{(p)}}. \end{aligned} \tag{3.15}$$

3.2.6 Stochastic heat transfer

Heat transfer o the wall is calculated based on the heat transfer coefficient calculated according to Woschni's model [74] give by Equation 3.16.

$$h_g = 3.26 \cdot d^{-0.2} \cdot p^{0.8} \cdot T^{-0.53} \cdot \left(C_1 c_m + C_2 \frac{V T_0 p_0 V_0}{p - p_{\text{mot}}} \right). \tag{3.16}$$

In Equation (3.16), h_g is heat transfer coefficient, C_1 and C_2 are heat transfer coefficients, d, p, v and T are cylinder bore, pressure, volume and temperature respectively. c_m is the mean piston speed and p_{mot} is the motored cylinder pressure.

From Equation (3.16) , the total heat transferred to the wall is calculated. To account for the fluctuations in the heat transfer due to inhomogeneity in the temperature of the in-cylinder mixture and walls in actual combustion chambers, the stochastic fluctuations are introduced into the model. Particles exchange heat with the wall probabilistically, where heat transfer magnitude and particle selection depend on the modelled parameter C_{ht} and random sampling. In practice, via C_{ht}, one can increase or decrease the number of particles that participate in the heat transfer process. This allows mimicking the inhomogeneity of the heat transfer, and consequently, in temperature, in actual engines.

3.3 Tabulated chemistry

Tabulated chemistry employing the Combustion Progress Variable (CPV) approach [9] to simulate combustion and emission formation provides a practical way to incorporate complex reaction kinetics into engine simulations without incurring extensive computational cost. Instead of solving a large system of chemical reactions during runtime, combustion chemistry and emission source terms are precomputed from a chosen detailed reaction kinetics mechanism and stored in look-up tables.

Within the SRM, this tabulated approach is based on parametrising the combustion progress in relation to EGR rate, pressure, unburned zone temperature, and equivalence ratio. This method operates under the assumption that a well-defined progress variable can effectively reconstruct the thermochemical state throughout the entire reaction trajectory using the CPV model [9, 33]. In this study, the progress variable is defined via latent enthalpy. Combustion chemistry and emission source terms are precomputed and stored in a look-up table, which is accessed during runtime.

In this thesis, tabulated chemistry is employed as a key enabler of the transient simulations using the SRM-based framework. The CPV tables were generated using a mechanism validated in earlier studies for surrogate fuels, ensuring accurate representation of ignition delays, flame speeds, heat release, and exhaust emissions [14, 33, 59]. By embedding these precomputed reaction kinetics into the SRM, the framework keeps physical realism and reduces computational cost, making it suitable for integration with MiL and HiL environments where real-time performance is essential. The reduction of computational costs is reached regardless of the underlying reaction mechanism size [33].

3.4 FMU and SRM integration

The SRM is compiled as an FMU to enable its integration with MiL/HiL environments. This method allows smooth interaction between the SRM and external models like MATLAB/Simulink or dSPACE ASM. The integration uses the FMI standard. The FMU acts as a container for the SRM computation core and follows standard signal exchange protocols. The resulting compiled model is here referred to as FMU/SRM.

3.4.1 FMU architecture and implementation

The FMU was built using the FMI 2.0 standard, which supports co-simulation mode. In this setup, the SRM works as an independent solver that takes input signals and sends output variables at fixed communication intervals. The FMU interface includes a few components.

- Input ports for changing parameters such as engine speed, start/stop Crank Angle Degrees (CAD)s, intake and exhaust manifold pressures and temperatures, EGR rate, fuel mass per injection, and air-fuel ratio (ϕ).
- Control signal ports for valve timing, updates to the injection strategy, and combustion phasing.
- Output ports for metrics generated by the SRM, including peak pressure, IMEP, torque, and cycle-resolved emissions exhaust emissions.

The FMU was created by pairing the SRM solver code with an FMI-compliant XML manifest and binary interface. We compiled the SRM model as a dynamic-link library (DLL) in Windows environment or shared object (SO) in Linux environment and linked it with the FMU using a build automation tool that supports FMI standards, such as FMU SDK or CMake. The co-simulation master, like Simulink or the ASM real-time engine, managed time synchronisation and solver step alignment to ensure accurate communication.

3.4.2 Data exchange and real-time scheduling

When starting up, the FMU reads static conditions from SRM setup files. After this startup phase, transient data exchange begins. The FMU consistently receives updated input signals from the external simulation master (MiL or HiL), which replaces initial conditions and allows for cycle-resolved updates.

The FMU operates in asynchronous mode to ensure real-time performance and predictable behaviour. In this setup, each subsystem SRM, control unit, and environment model-updates independently to avoid global synchronisation delays. If SRM computations fall slightly behind during a cycle, the FMU provides the most recent completed outputs to maintain continuity and prevent gaps in the control loop. We monitor output signals for consistency over time, seamless hand-off, and physical reasonableness. Real-time execution tests showed that when the SRM solver was packaged within an FMU, it met the latency and throughput needs for closed-loop controller interaction in HiL setups. Simulation workflow and data exchange are schematically presented in Figure 3.3, while details of SRM/FMU integration are described in next subsection.

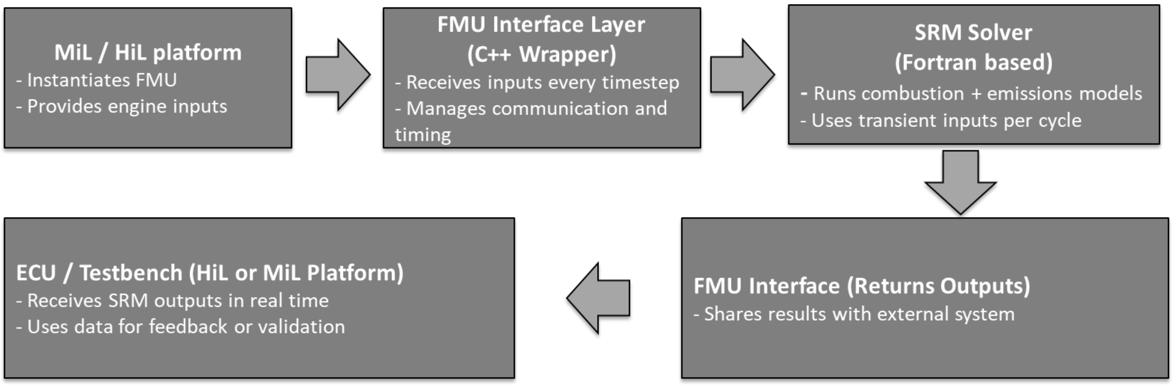

FIGURE 3.3: Simulation workflow with FMU-based SRM.

3.4.3 FMU wrapper and SRM solver integration

The integration involves developing an FMU in C++ that serves as an FMI-compliant wrapper around the SRM solver written in Fortran. The FMU provides standard interfaces (functions defined by the FMI 2.0 specification) and passes computational tasks to Fortran through cross-language linking. The step-by-step integration breakdown is as follows.

- The Fortran-based SRM solver provides routines for initialisation, input handling, combustion cycle computation, and extraction of performance and emissions results.
- On the C++ side, the FMU wrapper implements the standard FMI 2.0 interface functions, ensuring that input/output handling, time-stepping, and model instantiation

follow the FMI specification. This allows the SRM to be seamlessly linked with external simulation platforms such as Simulink or dSPACE environments.

- Linking C++ and Fortran: Compile the Fortran SRM functions into a shared library (.DLL, .so, or .Dylib) based on the platform. The Fortran functions use an extern "C" linkage specification to maintain name compatibility with C++. We pay close attention to how arguments are handled across languages, including variable types, array structures, and memory alignment, to ensure reliable data exchange. We use platform-specific dynamic linking, using dlopen on Linux/macOS and LoadLibrary on Windows to load the compiled Fortran libraries during runtime.
- Data Buffering: The FMU stores the last known outputs if the SRM is still solving, allowing for real-time data availability.
- Time Synchronization: The FMU does not advance if no change in operating parameters, such as engine speed for instance, is detected.
- Error Handling: The SRM can return convergence flags or warnings that the FMU logs through fmi2Status.

The configuration's benefits include keeping Fortran's computational strengths for chemistry and thermal modelling. The C++ FMU ensures real-time compatibility with MiL/HiL tools. Modular linking allows easy testing of different SRM solvers without rebuilding the whole FMU structure.

3.4.4 Framework for real-time transient simulations

Within this work, the SRM was reconfigured to simulate transient in-cylinder processes in real-time. Key input variables, including engine speed, valve timing on crank angle (CAD) basis, intake and exhaust manifold pressure and temperature, exhaust gas recirculation (EGR) rate, fuel mass per injection shot and air-fuel equivalence ratio (ϕ), are updated as time-resolved or cycle-resolved parameters. These changes reflect continuously evolving operating states during transient engine operation.

The SRM model connects with external simulation platforms such as MATLAB/Simulink or dSPACE ASM engine models through a MiL or HiL setup. Initial state variables are loaded through the setup files. After this, the FMI starts communication with the complete model. This interface continuously sends updated engine input parameters to the SRM, replacing the initialisation values and updating them for each subsequent cycle. After each combustion cycle, the SRM provides real-time engine-out performance parameters and exhaust emissions at the Exhaust Valve Opening (EVO). Engine metrics include maximum pressure, IMEP, torque, and the location of the combustion centre. Engine-out emissions would be according to fuel type. The list of available parameters can be extended upon request. The model setup is shown in Figure 3.4.

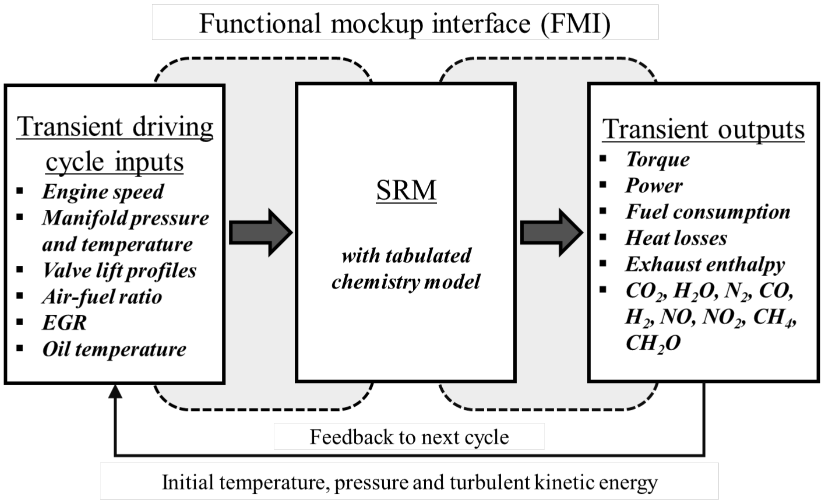

FIGURE 3.4: Concept of transient driving cycle simulations using the SRM embedded in FMI.

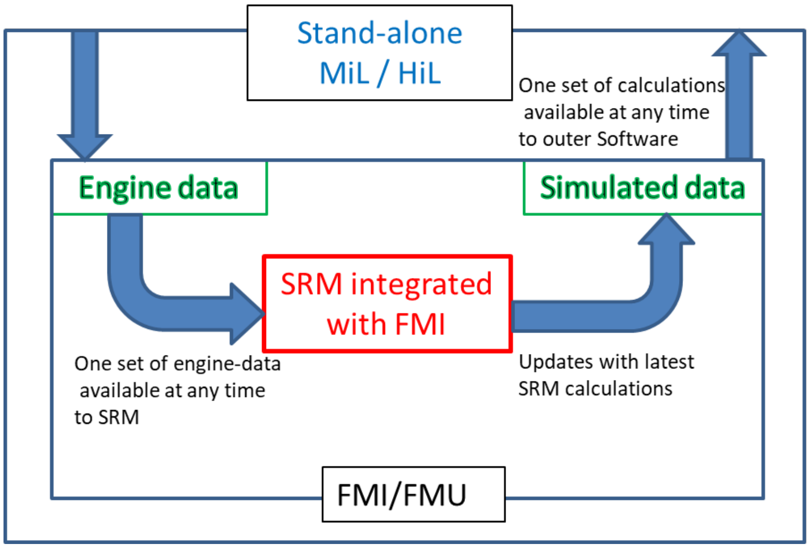

FIGURE 3.5: FMI/FMU and SRM interfacing.

The simulation setup is designed to accommodate subsystems that operate at different update rates, thereby maintaining responsiveness and data integrity. While MiL or HiL hardware components may have a sampling period of 1ms. So, enforcing a uniform 1ms time step across all components is not required. The scheduling approach allows the SRM and interfacing controllers to run at their own appropriate rates. A schematic of this interface is shown in Figure 3.5. This strategy reduces computational load and prevents fluctuations caused by synchronization. If SRM calculations for a given cycle are not completed in time, the outputs from the previous cycle are retained and passed to downstream systems. In this way, the setup preserves real-time and ensures continuity in control feedback loops.

3.5 Vehicle driving cycle procedures

Testing IC engine performance, fuel economy, and exhaust emissions under realistic driving conditions is an essential task in vehicle development and certification. Standard driving cycles are employed to provide consistency, comparability, and compliance with regulations across varying test environments. In this thesis, the simulations are carried out using WLTP and NRTC driving cycles.

3.5.1 WLTP for on-road light vehicles

The WLTP is a globally adopted standard for testing fuel consumption and emissions of light-duty vehicles [5]. The WLTP, established under the United Nations Economic Commission for Europe (UNECE), better represents contemporary driving patterns than it's predecessor, the New European Driving Cycle (NEDC). Comprising four phases-Low, medium, high, and extra-high it replicates mixed urban, suburban, and highway driving patterns over a combined distance of 23.3km and a total duration of around 1800s as shown in Figure 3.6 [5]. WLTP Class 3 is particularly for vehicles having a power-to-mass ratio of more than 34 kW/ton and a maximum speed greater than 135 km/h. It includes a combination of acceleration, deceleration, cruising, and idling stages that stress the transient response of power-trains and after-treatment systems.

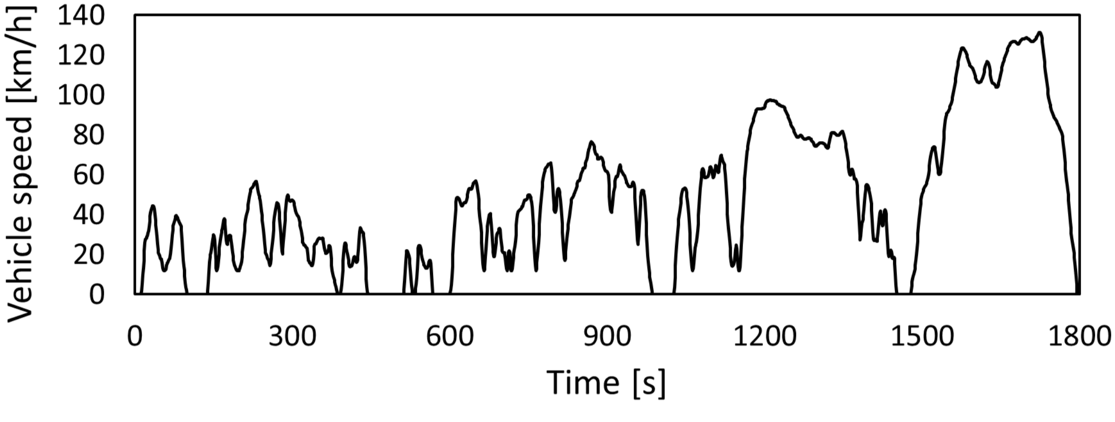

FIGURE 3.6: WLTP driving cycle.

WLTP is obligatory for type approval and emissions certification, which constitutes the legal foundation for market entry and vehicle registration. The cumulative quantity of regulated pollutants-mainly NO_x, CO, HC, and Particulate Matter (PM)-released during the cycle establishes if a vehicle complies with emissions regulations [75]. Precise adherence to WLTP guarantees real-world representativeness, thus reducing the discrepancy between laboratory certification and on-road performance [76].

3.5.2 NRTC for off-road machinery

The Non-Road Mobile Machinery (NRMM), like agricultural tractors, construction equipment, and industrial power units, is tested under the non-road transient cycle (NRTC), which was established by the U.S. Environmental Protection Agency (EPA) and codified in ISO 8178 standards [77]. Unlike WLTP driving cycle, NRTC is aimed at testing the engine performance rather than the whole vehicle. The test refers to the normalised engine speed varying with time for 1200s as shown in Figure 3.7 [6, 78].

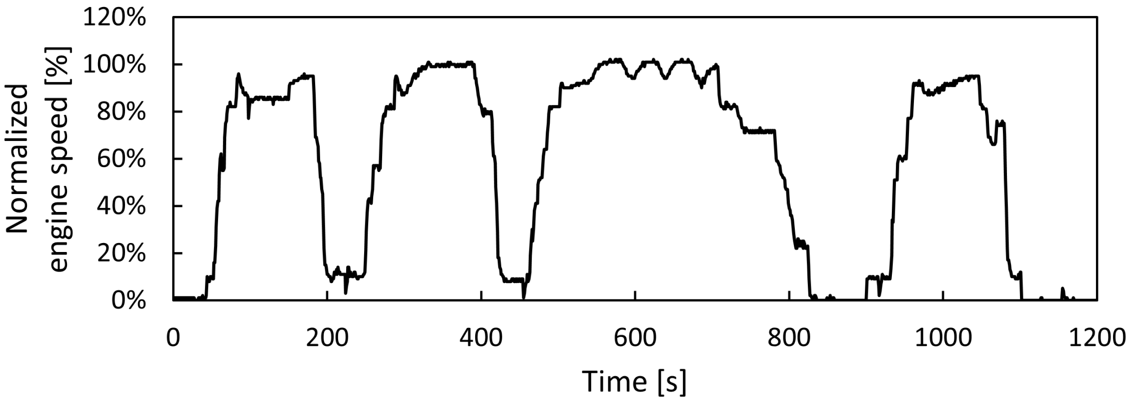

FIGURE 3.7: NRTC driving cycle with normalized engine speed.

The NRTC replicates very dynamic and non-repetitive engine load and speed profiles, reflecting real-world off-road use, with frequent transients, load reversals, and idle periods. In contrast to steady-state test. cycles, the NRTC includes both cold-start and hot-start operating segments, which better reflect field operations [77]. It plays a crucial role especially in certifying engines to meet tier 4, stage V, and other non-road emission standards. Due to the severe duty cycles of NRMM applications, the use of the NRTC guarantees that engines are designed with adequate strength to manage emissions even during extreme transient loads [79].

3.5.3 Uncertainty quantification in transient simulations

Uncertainty quantification is essential for comparing simulation and measurement data during transient engine operations. Both model-based and data-driven approaches encounter uncertainty from physical simplifications, noisy inputs, and limited calibration datasets [80, 81]. Models relying on steady-state data often misrepresented in transient behaviour, while look-up table methods may falter outside data boundaries [81]. Machine learning-based models also face generalization limits when training data lacks coverage of dynamic scenarios [82][27].

Emissions measurement uncertainties arise from both instrumental limitations, environmental variability during testing, and variability of the measured processes themselves. Factors such as sensor calibration errors, response time lag, ambient temperature effects, and exhaust dilution can all distort the accuracy of readings for pollutants like NO_x, CO, or hydrocarbons. According to [83], inconsistencies in sensor dynamics and placement, especially during transient conditions, can lead to measurement delays and damped signal profiles that differ from instantaneous emissions behaviour. Additionally, cold-start events, fuel vaporisation dynamics, and thermal lag in after-treatment systems often introduce significant discrepancies that are hard to capture with real-time measurement instruments.

Uncertainty quantification is essential when comparing simulation outputs to experimental emissions data. Typically, statistical validation metrics such as Root Mean Square Error (RMSE), correlation coefficient (R^2), and normalised mean bias to evaluate agreement [83, 84], are applied for that purpose. It's critical to align both datasets temporally and spatially-ensuring synchronisation of sampling rates and consistent boundary conditions. The analysed ranges of data reflect 95% confidence intervals commonly used in uncertainty analysis, as recommended by the IPCC and EDGAR inventory frameworks [85, 86]. For example, EDGAR reports global greenhouse gas emissions are accurate within -15% to +20% overall, while pollutants like N_2O and PM exhibit significantly higher uncertainty. When validating simulations, it's critical to account for both instrumental uncertainty and modelling assumptions. Even strong statistical correlations (e.g., $R^2 > 0.9$) may obscure systematic errors caused by unrecognised dynamics or sensor limitations [83]. Cross-validation,time-aligned signal comparison, and cycle-average assessments are recommended for robust analysis [84, 87]

TABLE 3.2: Uncertainty of measurement of various exhaust species.

Pollutant	**Uncertainty Range**	**Remarks**
CO_2	±10–15%	Based on fuel use; low measurement error [85]
NO_x	±20–40%	Combustion and transient-cycle sensitive [83]
HC	±25–50%	Cold-start and vaporisation effects [84]
CO	±20–30%	Depends on air–fuel ratio [83]
PM/Soot	±30–60%	Nucleation and oxidation variability [86]
CH_4	±30–50%	Often underestimated [85]
N_2O	±50–100%	High uncertainty in non-combustion sources [86]

To determine the quality/repeatability of the results simulated by the toolchain employing the SRM, a literature study was performed to define an accuracy window for each exhaust species of interest. That accuracy window defines ranges characteristic of experimental works that are to be reached by simulations. These accuracy windows for selected exhaust species are listed in the Table 3.2.

3.6 SRM/FMU in MiL/HiL testing platforms

This work adopts a co-simulation mechanism that combines an FMU/SRM with different integration environments depending on the application requirements, such as stand-alone (SA) and ASM-integrated MiL/HiL environments. These configurations enable a bidirectional data exchange between the FMU and surrounding simulation frameworks to perform a transient engine simulation.

3.6.1 MiL/HiL workflow in dSPACE ASM

The MiL/HiL frameworks adopted in this work for connecting with the presented in Section 3.4 FMU/SRM, are based on the dSPACE ASM system. The workflow of integrating the FMU/SRM is presented in Figure 3.8.

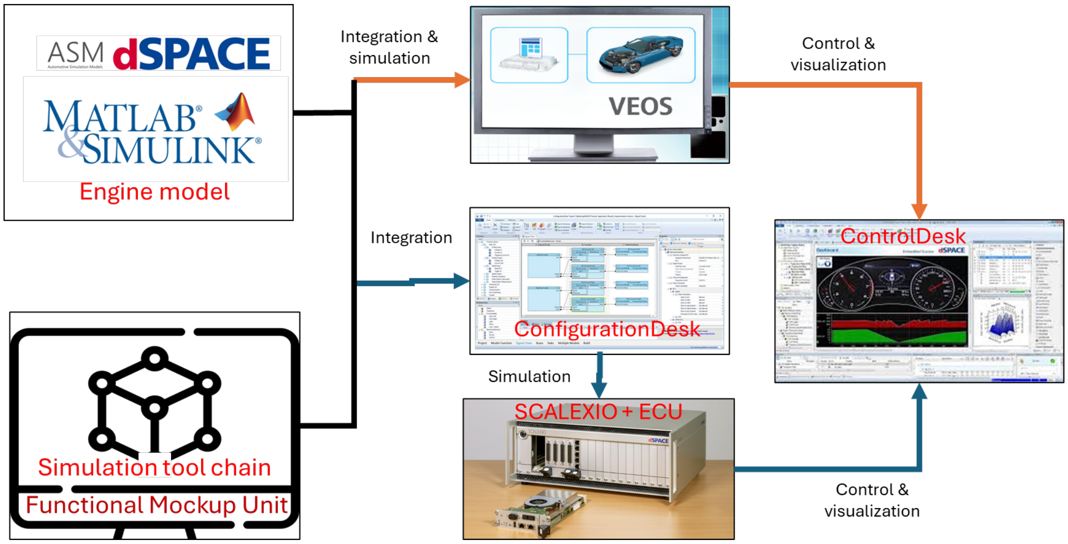

FIGURE 3.8: Simulation toolchain implementation in MiL and HiL.

For conventional real-time engine and vehicle-level simulation, the engine model is built on dSPACE ASM, which is essentially a collection of open Simulink models. ASM models comply with structured signal buses and use a standard set of interfaces to allow efficient linking to external models. The FMU is framed as an interface against the ASM model using a modelDescription.xml file, which defines the mapping of input/output variables according to FMI 2.0.

The simulation toolchain integration and simulation setup for MiL and HiL use a compiled Simulink Information Container (SIC) file, which encapsulates simulation logic and interface definitions. Both the FMU and the SIC are imported into VEOS for MiL execution, while for HiL, they are imported into ConfigurationDesk, dSPACE's PC-based environment for multi-model integration and real-time execution without hardware. VEOS/ConfigurationDesk automatically recognises the I/O ports on both the FMU and ASM model, allowing data exchange during run-time.

3.6.2 Components of the ASM

The ASM is a simulation environment based on Simulink in the MATLAB environment that is used to model the dynamics of vehicles and engine behaviour. The ASM model includes different plant sub-models and control units, allowing for a comprehensive simulation of engine systems. Transient data generated during simulations is exchanged between the ASM and the SRM through defined interface ports, thereby enabling an accurate representation of physical processes, such as combustion, emissions, and control response. The ASM model communicates with the SRM through a series of predefined ports, where each one corresponds to particular input or output signals as shown in Figures 3.9-3.12

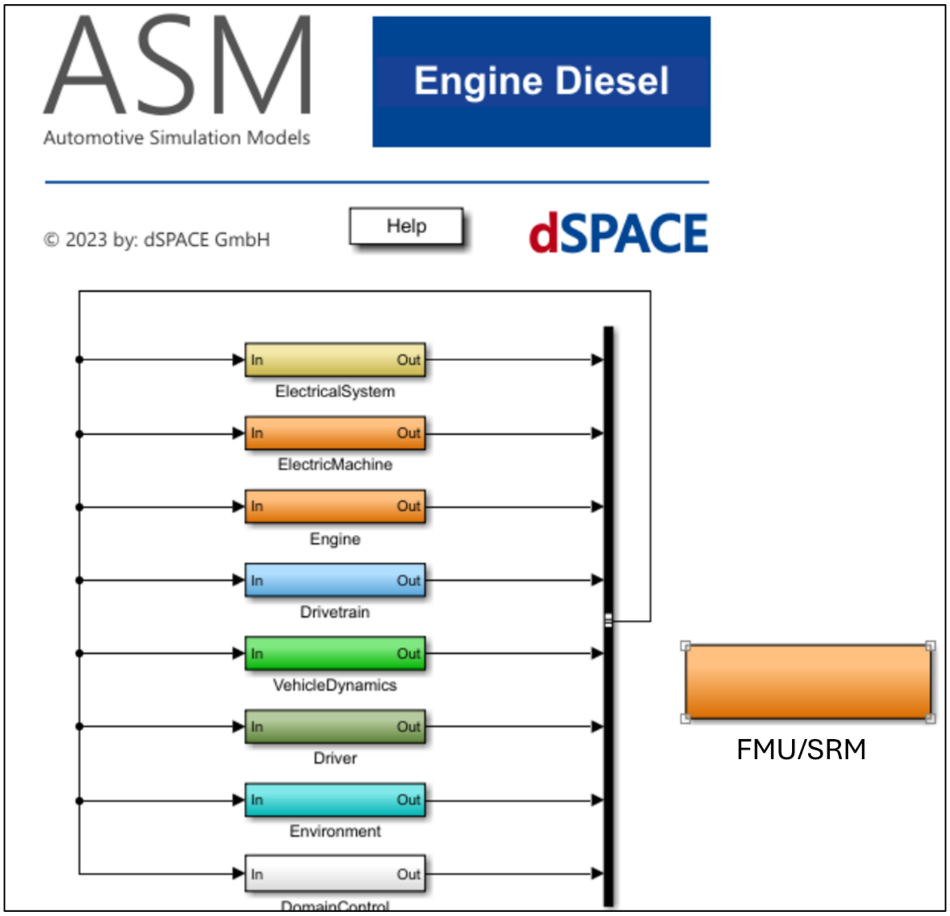

FIGURE 3.9: Interface for integrating FMU/SRM into ASM model [18, 63].

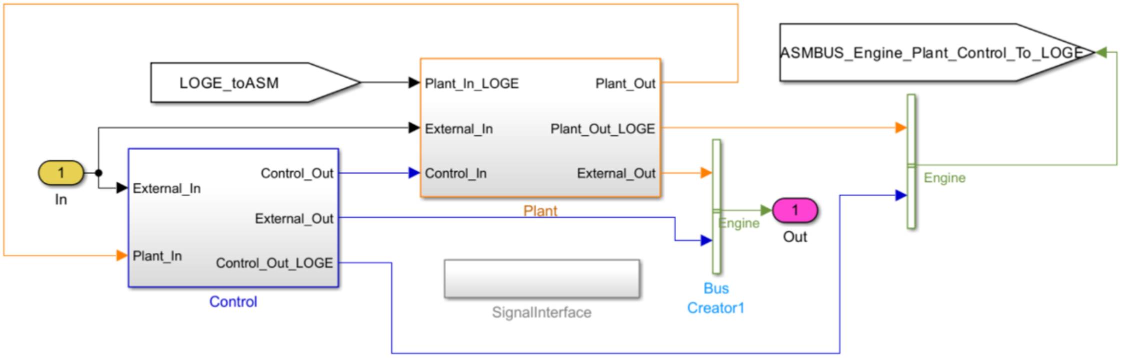

FIGURE 3.10: Interface links in the ASM engine model for FMU/SRM [18, 63].

For each of the required engine data by SRM will be connected to a port as shown in Figure 3.11 The ports are resolved by name through the use of the modelDescription.xml file, which provides consistent signal mapping between the ASM and SRM models. This XML

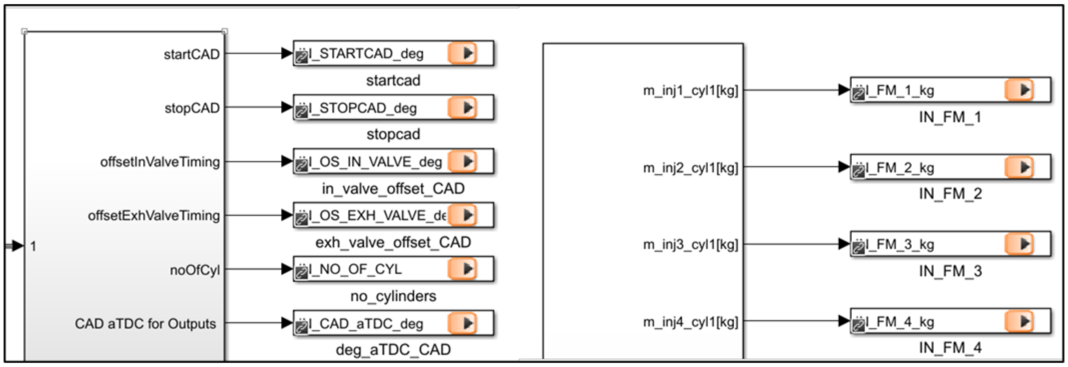

FIGURE 3.11: ASM ports for transient engine simulations based on the FMU/SRM framework.

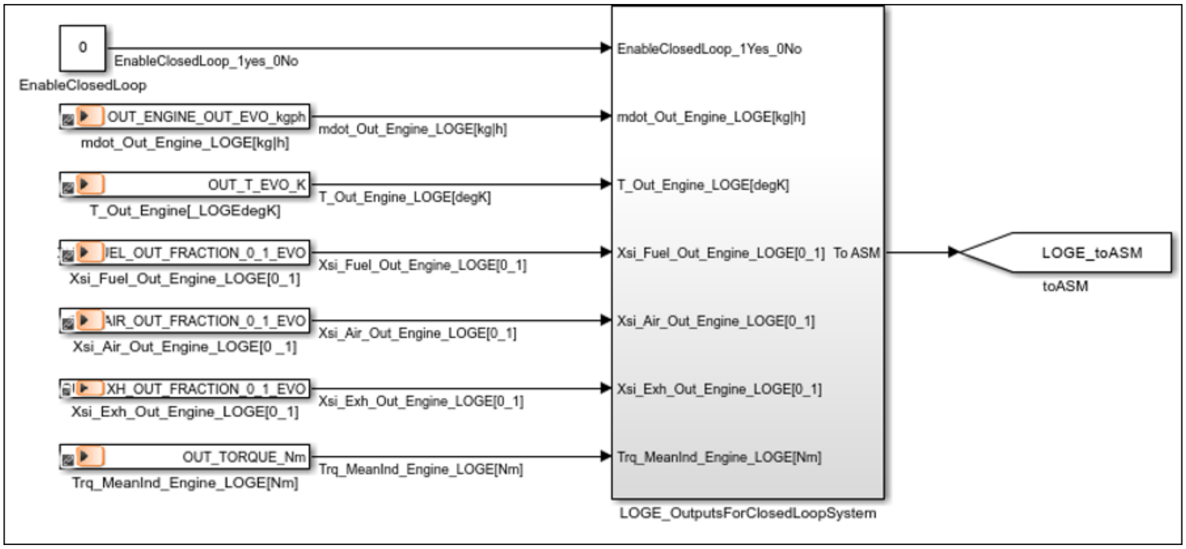

FIGURE 3.12: Ports from FMU/SRM to ASM as feedback.

setup serves as a liaison between the simulation layers, facilitating smooth data exchange. The MATLAB/Simulink integration with SRM facilitates modular development and testing of engine control strategies with ease of application in various simulation environments. The simulated engine output parameters will be feed-backed to ASM as illustrated in Figure 3.12. The ports are specified in the simulation architecture and resolved by name through the use of the modelDescription.xml file. This provides the mechanism to ensure that every signal is properly routed between the ASM and SRM parts, with data integrity and synchronisation intact. In HiL environments, the executable form of the ASM model executes in real time so that dynamic interaction with physical ECUs and real-world inputs is possible, whereas MiL simulations use virtual timing mechanisms.

3.6.3 Integration in MiL/HiL frameworks

For HiL simulations, the integrated environment of the ASM model with FMU/SRM executes on a SCALEXIO system. A SCALEXIO system (Figure 3.13) is a real-time computing platform that communicates with physical ECUs and sensors. This enables high-accuracy testing of engine control strategies in realistic conditions [18]. The soft ECUs in the ASM model are replaced with actual physical ECUs, and the model is compiled into a real-time executable that runs on a HiL-connected system, i.e., SCALEXIO. This setup enables the testing of control units under scenarios that are very close to real-world conditions, effectively closing the gap between virtual testing and real implementation (Figure 3.14).

FIGURE 3.13: SCALAXIO hardware platform used for the HiL simulations.

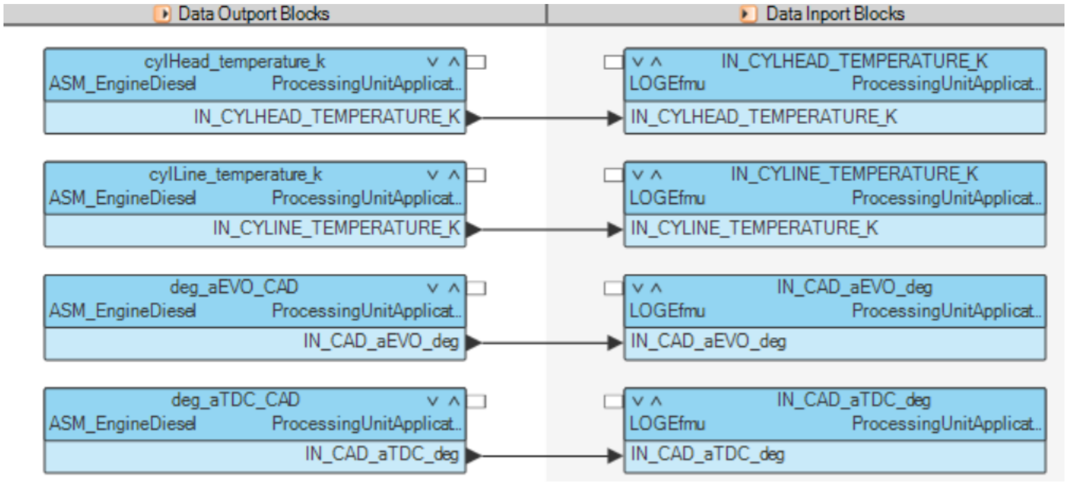

FIGURE 3.14: Integration of ASM model with simulation toolchain in real hardware environment SCALEXIO.

MiL simulations, on the other hand, are run in a virtual environment, usually on a conventional PC. The virtual environment is provided by dSPACE VEOS [18]. VEOS is the dSPACE platform for PC-based simulation of models and virtual ECUS (VECU) and network communication. It lets ASM models be connected via FMI to FMU/SRM (Figure 3.15). The ASM model supports both MiL and HiL simulation environments. In MiL simulations, the ASM model is translated into an executable code that runs in a virtual computation environment, thus allowing developers to test control algorithms without the need for physical hardware.

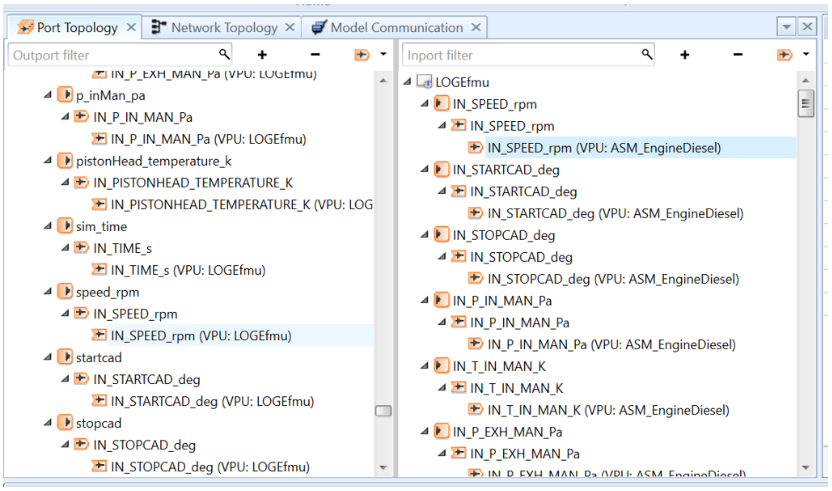

```
IN_P_EXH_MAN_Pa (VPU: LOGEfmu)
p_inMan_pa
  IN_P_IN_MAN_Pa
    IN_P_IN_MAN_Pa (VPU: LOGEfmu)
pistonHead_temperature_k
  IN_PISTONHEAD_TEMPERATURE_K
    IN_PISTONHEAD_TEMPERATURE_K (VPU: LOG
sim_time
  IN_TIME_s
    IN_TIME_s (VPU: LOGEfmu)
speed_rpm
  IN_SPEED_rpm
    IN_SPEED_rpm (VPU: LOGEfmu)
startcad
  IN_STARTCAD_deg
    IN_STARTCAD_deg (VPU: LOGEfmu)
stopcad
  IN_STOPCAD_deg
    IN_STOPCAD_deg (VPU: LOGEfmu)
```

```
LOGEfmu
  IN_SPEED_rpm
    IN_SPEED_rpm
      IN_SPEED_rpm (VPU: ASM_EngineDiesel)
  IN_STARTCAD_deg
    IN_STARTCAD_deg
      IN_STARTCAD_deg (VPU: ASM_EngineDiesel)
  IN_STOPCAD_deg
    IN_STOPCAD_deg
      IN_STOPCAD_deg (VPU: ASM_EngineDiesel)
  IN_P_IN_MAN_Pa
    IN_P_IN_MAN_Pa
      IN_P_IN_MAN_Pa (VPU: ASM_EngineDiesel)
  IN_T_IN_MAN_K
    IN_T_IN_MAN_K
      IN_T_IN_MAN_K (VPU: ASM_EngineDiesel)
  IN_P_EXH_MAN_Pa
    IN_P_EXH_MAN_Pa
      IN_P_EXH_MAN_Pa (VPU: ASM_EngineDiesel)
```

FIGURE 3.15: Integration of ASM model with FMU/SRM in virtual computational environment VEOS.

3.6.4 Simulations in stand-alone modes

A stand-alone simulation mode has been developed for debugging, verification, and comprehensive testing of transient simulations as well as for the case where transient driving cycle input data are available from measurements. Figure 3.16 illustrates the schematic flowchart of this setup.

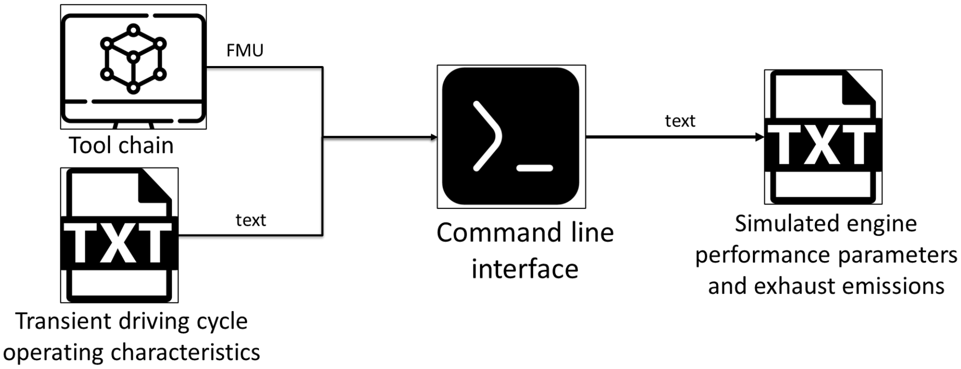

FIGURE 3.16: Toolchain's implementation in a stand-alone environment.

In this configuration, all transient engine conditions are sourced from text-based input files. The FMU/SRM is connected to these input files via FMI and operates in a command-line interface, ensuring platform independence and portability across both Windows and Linux systems.

This stand-alone mode is particularly advantageous for testing and rapid prototyping, especially when integration with Simulink/ASM is not required or not available. Additionally, this approach facilitates transient simulations without the need for a MiL or HiL environment. By importing these text files into a Simulink environment, the SRM FMU can also be executed within Simulink, thereby supporting both stand-alone and co-simulation environments. The stand-alone Simulink/SRM intergeneration environment is shown in Figure 3.17. In this configuration, the SRM can be directly imported as an FMU into a Simulink framework and can be connected to ports defined by modelDescription.xml.

3.7 ANN-based meta-model

In order to offset the computational resources associated with transient engine simulations with the developed toolchain, a meta-model employing an ANN has been developed. The purpose of this development was to provide a methodology for applications that could be simulated faster than real-time, such as testing other sub-models and their control algorithms, without requiring changes in the modelling of the in-cylinder processes. Hence, the

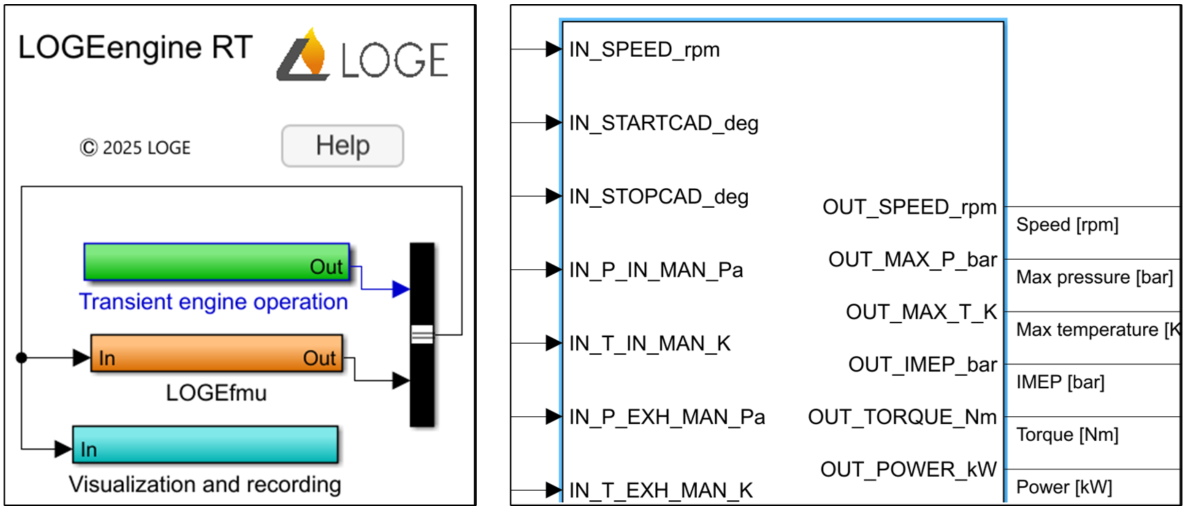

FIGURE 3.17: Simulation toolchain working in stand-alone mode and integrated in MATLAB/Simulink.

training of the ANN is carried out based on the physics-based model employing the SRM, and the whole development of the ANN is here considered preliminary.

In this work, a Keras' sequential class is employed [88] to construct a three-layer neural network, programmed in Python with the TensorFlow [89] and scikit-learn [90] libraries. The architecture of the network consists of an input layer with 128 neurons, followed by a second layer containing 64 neurons, and concluding with an output layer having same number neurons as the quantity of outputs. A Reflective Linear Unit (ReLU) is used as the activation function to enhance the network's performance, which allows for the introduction of non-linearity.The optimisation of the model was achieved through the Adam optimisation algorithm [91], which implements stochastic gradient descent.

The workflow of developing, training the meta-model, and its application is illustrated in Figure 3.18. The diagram illustrates the development process of a neural network model used to predict engine-out emissions and performance based on transient engine data from the physics-based toolchain and using the SRM. Initially, transient engine data and corresponding engine-out emissions and performance data are used to train the neural network. Once trained, the model is evaluated by using transient engine data to predict engine-out data, which is then compared to the toolchain's simulation data to check the prediction accuracy. If the assumed accuracy is not within the acceptable range, the process loops back for further training with updated data. The loop repeats until the accuracy meets the assumed threshold, which in this work was assumed to be 5.

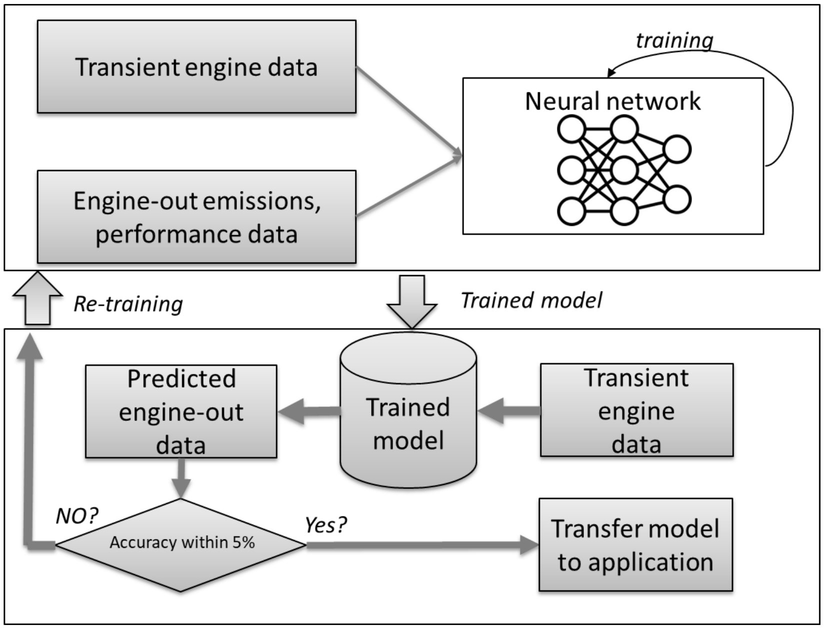

FIGURE 3.18: ANN training and prediction model.

3.8 Simulation toolchain

This section integrates the modelling components discussed in Sections 3.2-3.7 which is schematically illustrated in Figure 3.19. The principal contribution of this work lies in the development of a unified simulation framework, enabling real-time transient engine simulations by combining the SRM, tabulated chemistry for combustion and emissions formation, FMU interfaces, and surrogate ANN meta-model and the possibility to couple them within testing platforms such as MiL and HiL.

Generic structure

The simulation toolchain development aims to establish a physically detailed and computationally efficient transient engine real-time simulation framework. This is achieved through the integration of the SRM with the FMI and FMU standards. By enabling the SRM to handle transient inputs, such as variable engine speeds and injection strategies, transient simulations are possible. Exporting the enhanced SRM as an FMU ensures compatibility with MiL/HiL platforms, enabling a seamless system-level transient simulation environment. Such a defined toolchain is considered a physics-based driving cycle simulator.

To meet the demands of real-time execution, the framework is optimised for computational efficiency without sacrificing accuracy. Its validity is demonstrated through testing using driving cycle data on both CI and SI engines. These tests serve not only to confirm the model's realism but also highlight its flexibility across fuel types. The development of a

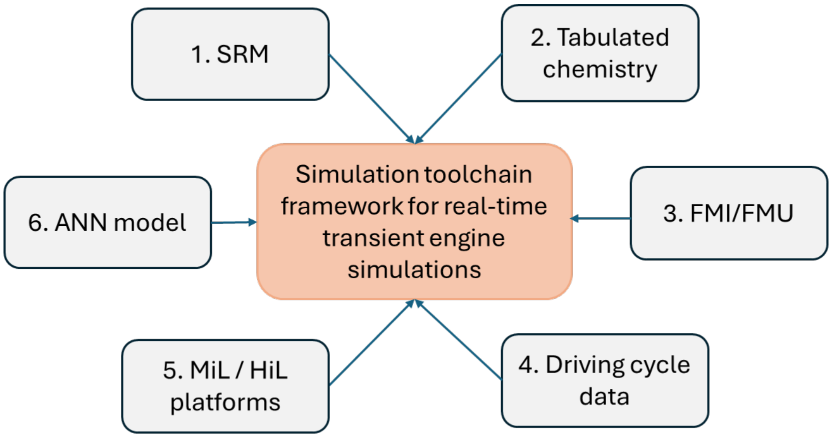

FIGURE 3.19: Components of the developed toolchain resulting in a physics-based driving cycle simulator.

surrogate ANN meta-model enables even faster simulations for beyond real-time simulation demands. Altogether, the architecture bridges the gap between high-accuracy combustion modelling and real-world application, advancing the field of engine simulation and control systems development. The Table 3.3 describes each component of the developed toolchain presented in Figure 3.19. Here, the toolchain refers to engine transient driving cycle simulations, but the development allows for using the framework with any type of transient data.

TABLE 3.3: Mapping of simulation toolchain elements to technical objectives.

Diagram element	**Role in in the toolchain**
SRM	0D model of engine in-cylinder processes
Tabulated chemistry	Modelling of combustion and pollutant Fuel surrogate formulation
FMI/FMU	Interfacing, modularity and system-wide compatibility
Driving cycle data	Inputs to run engine transient driving cycle
MiL/HiL platforms	Integrity with 3$^{\text{rd}}$ party testing platform
ANN meta-model	A surrogate meta-model for computational cost reduction

In the diagram in Figure 3.19, transient engine simulations sit at the centre, surrounded by seven interconnected components. While each element contributes a specialised capability like SRM for modelling of in-cylinder processes or tabulated chemistry for detailed but CPU efficient prediction of combustion and pollutant formation the true power of this ecosystem is unlocked through the FMU. FMU is the programmable interface that binds all these models into a unified simulation framework. By encapsulating each model into FMU, one creates modular, interoperable units that can be executed together, regardless of their origin or complexity. This modularity is what makes real-time transient simulations feasible.

For example, driving cycle data feeds transient input conditions into the FMU-based system. The SRM and tabulated chemistry models, wrapped as FMU, respond to these inputs with high-accuracy combustion and emissions outputs. The FMU framework ensures that all these components communicate seamlessly, whether the simulation runs on a MiL/HiL platform or is integrated with third-party tools. In essence, by programming FMU, the entire simulation toolchain is orchestrated into a synchronised, scalable, and portable simulation environment—making transient engine modelling not only possible but efficient and robust.

Toolchain configuration in dSPACE system

The simulation toolchain's working methodology is shown in Figure 3.19. In both MiL and HiL simulation setups, the dSPACE ASM Simulink model serves as the transient input provider to the SRM wrapped in an FMU.

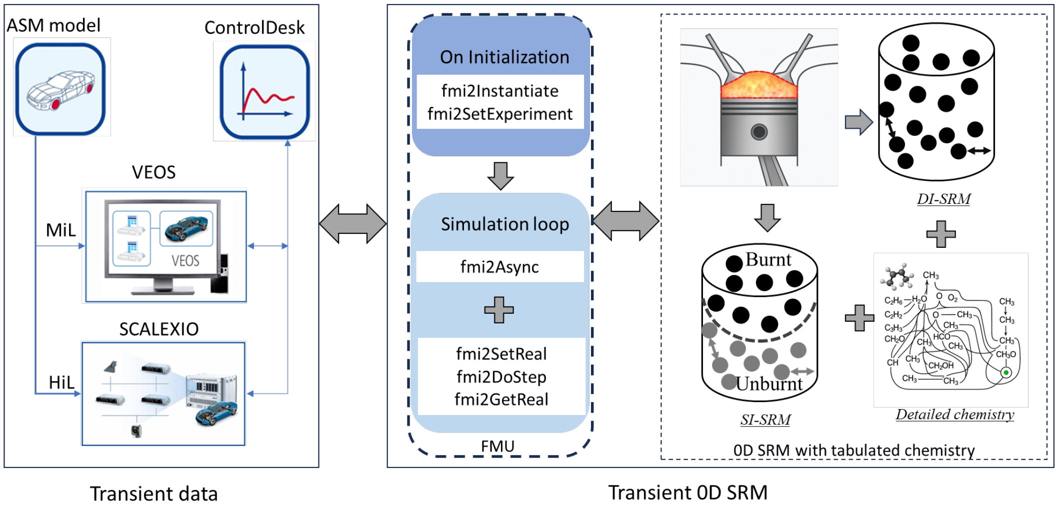

FIGURE 3.20: Toolchain configuration in MiL/HiL systems from dSPACE.

For MiL simulations, the Simulink model is exported as a 32-bit SIC file and integrated within VEOS, which acts both as the integrator and simulator. The FMU, containing the combustion solver, is linked to the ASM model through port name matching defined in the FMU's modelDescription.xml and the ASM output signal names. When names match, the connections are automatically established. The result is a virtual simulation environment where the ASM provides transient operating conditions and the FMU performs combustion calculations. This co-simulation is managed and monitored in dSPACE ControlDesk, which also allows toggling optional inputs, such as enabling or disabling feedback.

In HiL simulations, the same integration concept is applied, but with a real-time execution framework. The ASM model is exported as a 64-bit SIC file and integrated with the FMU-based transient 0D SRM using ConfigurationDesk. As in MiL, signal connections are resolved automatically by port name matching. The integrated model is deployed to real-time hardware, and simulations are executed in a deterministic environment. ControlDesk remains the user interface for data monitoring and interaction, enabling real-time control over optional FMU inputs. This setup ensures consistent integration logic across MiL and HiL.

Chapter 4

Results and discussion

4.1 Background

This chapter presents the simulation results applying the developed simulation toolchain as described in Section 3.8. The primary goal is to evaluate the accuracy, robustness, and computational performance of the developed simulation toolchain for simulating performance parameters and exhaust emissions of CI and SI engines operated under WLTP and NRTC transient driving cycles. The chapter begins by discussing the integration of the SRM-based engine model via FMU/FMI technology into MiL and HiL platforms, which defines a complete toolchain resulting in a physics-based driving cycle simulator. Next, the capability of predicting engine performance parameters and exhaust emissions from an on-road CI engine under the WLTP driving cycle is presented. Specifically, aspects of driving-cycle to driving-cycle variability in exhaust emissions are discussed. The next two sections dealt with using the toolchain to simulate SI engines operated during the cold-start phase of the driving cycle. The subsequent section is devoted to analysing the co-simulation of the engine and catalyst, which is considered a step towards system-level simulations. Finally, results obtained from the ANN-based meta-model of the physical driving cycle simulator employing the SRM are presented. The content of this chapter is based on the published results [24, 25, 26, 27].

4.2 MiL/HiL platforms-based engine simulations

This section evaluates the toolchain's real-time performance by integrating the simulating toolchain into both MiL and HiL platforms via FMI/FMU technology as introduced in Section 3.6. The goal is to demonstrate the functionality of the complete toolchain, including its integrity with the MiL/HiL platforms, and to qualitatively evaluate its performance.

4.2.1 Engine data and test case definition

The engine and driving cycle data utilised in this study are obtained from the dSPACE ASM package. The engine is a six-cylinder SI engine fuelled with gasoline and employs a port fuel injection system. The engine data were used to build the SRM of the engine in-cylinder processes. The transient load and speed demands on the engine are governed by a standardised driving cycle from the WLTP. By applying the driving cycle profile, the engine model is subjected to transient operating conditions that cover a representative range of vehicle usage scenarios, including idling, urban driving, and high-speed motorway operation. The SRM was built and configured according to the geometry data in Table 4.1. Simulations were conducted with Primary Reference Fuel (PRF) consisting of a blend of n-heptane (N-C7H16) and isooctane (I-C8H18). The fuel mixture used in this study has a mass fraction of 5.40% n-heptane and 94.60% iso-octane and represents commercial gasoline.

TABLE 4.1: Engine specification.

Parameter	**Unit**	**Value**
Bore	mm	79.8
Stroke	mm	75
Rod Length	mm	140
Compression Ratio	–	9.5:1

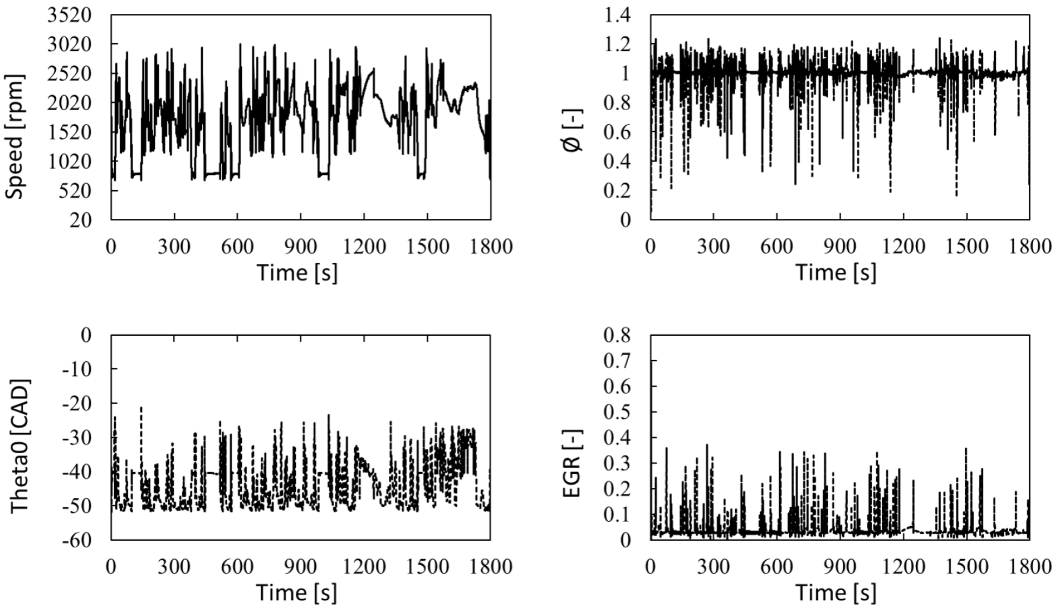

FIGURE 4.1: Simulated engine speed, equivalence ratio, spark timing and EGR during the WLTP driving cycle.

4.2.2 Exemplary results

The engine input parameters provided to the toolchain from the MiL and HiL models are shown in Figure 4.1. These inputs include engine speed, equivalence ratio, spark timing and EGR rate.

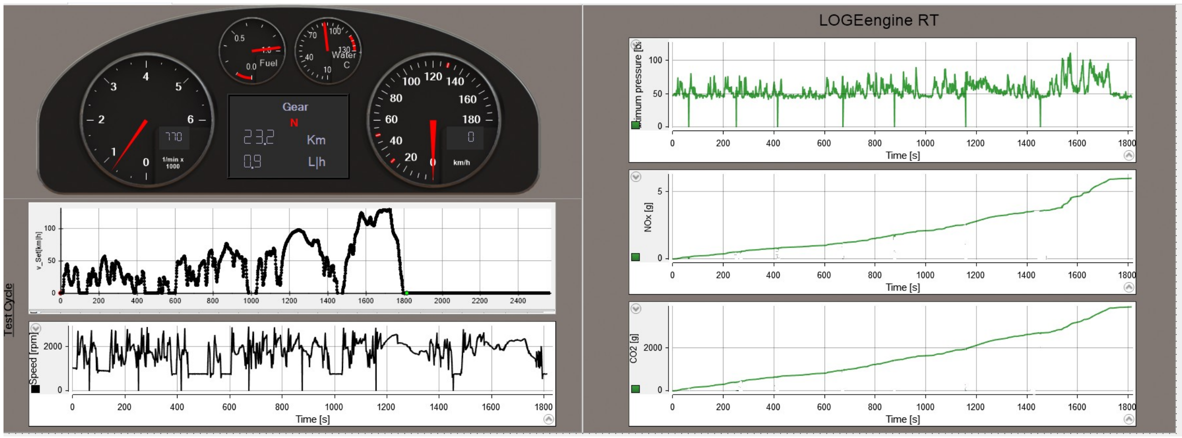

FIGURE 4.2: Dashborad view of the MiL/HiL simulations in dSPACE configurationDesk [18, 63].

Figure 4.2 illustrates the real-time execution environment of the MiL/HiL simulations using dSPACE ControlDesk, which is the recording utility that enables data logging during simulation runs. The dashboard view presents the live recording of engine-out emissions and key performance parameters during a transient WLTP cycle, and confirms the successful deployment and monitoring setup of the SRM-based FMU within the SCALEXIO or VEOS platform. These visualisations validate the integration and operational fidelity of the simulation framework under transient conditions.

Figure 4.3 presents simulated results for maximum in-cylinder pressure and the cumulative emissions of CO_2, CO, uHC and NO_x, over a 1800s WLTP driving cycle, using both MiL and HiL frameworks. The simulation results from MiL and HiL show close agreement, demonstrating consistency across both platforms.

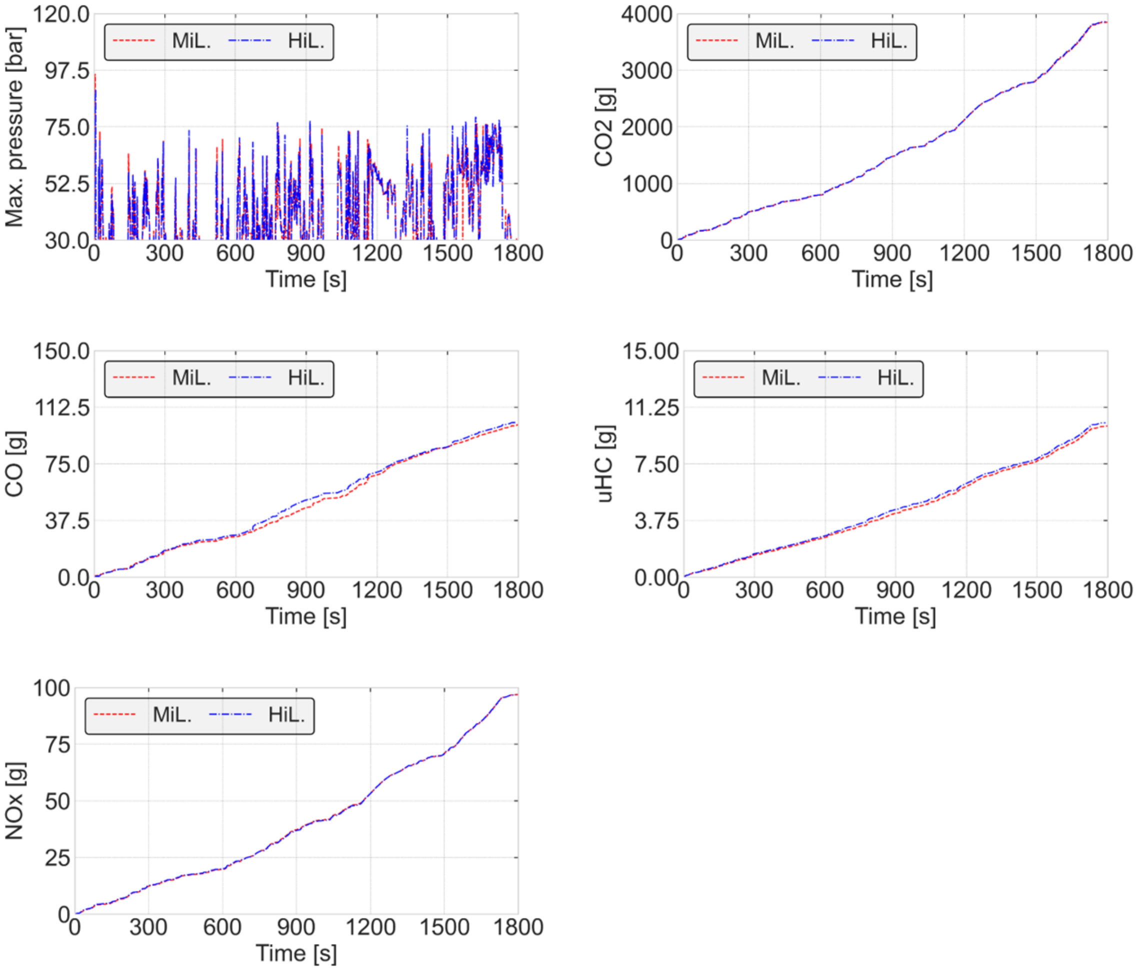

FIGURE 4.3: Results from MiL and HiL simulations of an SI engine.

4.2.3 Summary

This study demonstrates the integration of the SRM-based FMI/FMU framework into MiL and HiL platforms, enabling real-time engine simulations based on the methods outlined in Section 3.6. The engine model data were sourced from the dSPACE ASM package. The results confirm the flexibility and reliability of the developed toolchain across simulation environments, with consistent outputs observed between MiL and HiL. Minor discrepancies observed in cumulative emissions are attributed to the stochastic cycle-to-cycle variation that results in driving-cycle to driving-cycle variations, and here we simulated a single realisation of the driving cycle (see also the discussion in Section 3.5.3 and Section 4.3.5).

4.3 CI engine simulations under WLTP driving cycle

The purpose of this section is to demonstrate and evaluate the application of the developed toolchain to simulate CI engine operation under the WLTP driving cycle. This evaluation aims to assess the model's capability to accurately predict in-cylinder performance, combustion characteristics, and emissions behaviour under real-time transient operating conditions representative of regulatory certification testing. Furthermore, stochastic variability of predicted exhaust emissions under transient conditions is analysed in reference to the variability of corresponding measurement data. The data used in this study were adopted from the published journal article [44].

4.3.1 Engine specification and investigated steady-state operating points

The reference vehicle is a diesel-powered D-segment passenger car with a curb weight of 1500 kg. It is equipped with a manual transmission with 6 speeds and rear-wheel drive. The vehicle's engine is a 4–cylinder, 2.0L direct injection, CI engine that has both high-pressure and low-pressure exhaust gas re-circulation systems. More details about the reference engine can be found in the published work [44]. The engine specifications are outlined in Table 4.2.

TABLE 4.2: Specification of engine parameters of CI engine.

Parameter	**Unit**	**Value**
Bore	mm	83.0
Stroke	mm	92.35
Rod Length	mm	140.06
Pin Offset	mm	0.5
Compression Ratio	–	15.5:1

As a reference for SRM training, sixteen operating points were selected. These were representative of the engine operation under WLTP. The operating points (OP) are presented in Table 4.3. The operating conditions of the engine used for this investigation are outlined in Table 4.3. The engine map covers a speed range from 1000 to 3500rpm, and torque ranges from 0 to 250 $\text{N} \cdot \text{m}$. The relative stoichiometric ratio (λ) range spans from 1 to 5 down, and the exhaust gas recirculation (EGR) rate ranges from 0 up to 50%.

4.3.2 Reference diesel fuel and its surrogate

The engine is operated with B7 Diesel with a cetane number (CN) of 53.3. The fuel is blended with 7 vol-% of biodiesel. The diesel fuel is represented by a multi-component surrogate from LOGEfuel package [63]. The composition of the surrogate is outlined in Table 4.5. The properties of the surrogate are compared with the fuel used in the experimental work in

TABLE 4.3: Engine operating points for engine model training.

Operating point	Engine speed [rpm]	Torque [Nm]	λ [-]	EGR [%]
1	1000	79.046	1.51	31.88
2	1250	221.768	1.39	0.80
3	1250	142.819	1.32	19.47
4	1500	63.273	1.62	42.70
5	1500	0.046	4.61	49.07
6	1750	189.978	1.45	20.95
7	1750	316.898	1.49	5.78
8	1750	47.551	2.04	43.07
9	2000	47.445	1.93	43.83
10	2000	222.192	1.45	21.90
11	2000	316.605	1.42	10.80
12	2750	142.855	1.68	30.31
13	2750	253.173	1.55	11.86
14	3500	94.924	2.59	19.75
15	3500	15.781	4.40	30.79
16	3500	221.539	1.86	0.84

Table 4.4. The surrogate closely matches the CN, lower heating value (LHV) and C:H:O ratio of the experiment fuel.

TABLE 4.4: Comparison of reference Diesel fuel and its surrogate counterpart.

Parameter	Unit	Experiment	Surrogate
CN	–	52.5–52.9	53.0
LHV	MJ/kg	42.71	42.56
C:H:O	–	13.625:1.0:1.0	12.07:19.4:0.12

TABLE 4.5: Liquid volume fraction (LVF) of surrogate components.

Species	Unit	LVF
n-Decane	%	65.0
α-Methylnaphthalene	%	27.0
Methyl decanoate	%	8.0

4.3.3 Reference model results at steady-state conditions

The calibration was conducted for OPs listed in Table 4.3. The calibration relied on determining the constants of the turbulence model from which the mixing time was derived. It was targeted at finding one set of model parameters that would be valid for the entire engine matrix of operating points under consideration. The calibration procedure is beyond the scope of this work and is omitted.

The pressure profile from the steady-state training for the operating points 2 and 8 from Table 4.3 is shown in the upper left and right of Figure 4.4, respectively, and is compared against the reference pressure profiles. Simulation pressure matched well with the measured history. The Rate of Heat Release (RoHR) is shown in the lower left and right of the Figure 4.4, respectively. Although the simulation RoHR is having fluctuations, the overall trend is matching the reference RoHR. Similar accuracy was obtained in other operating points that resulted in an acceptable match between the simulated and reference data for maximum peak in-cylinder pressure and combustion centre (CA50) as presented in Figure 4.5

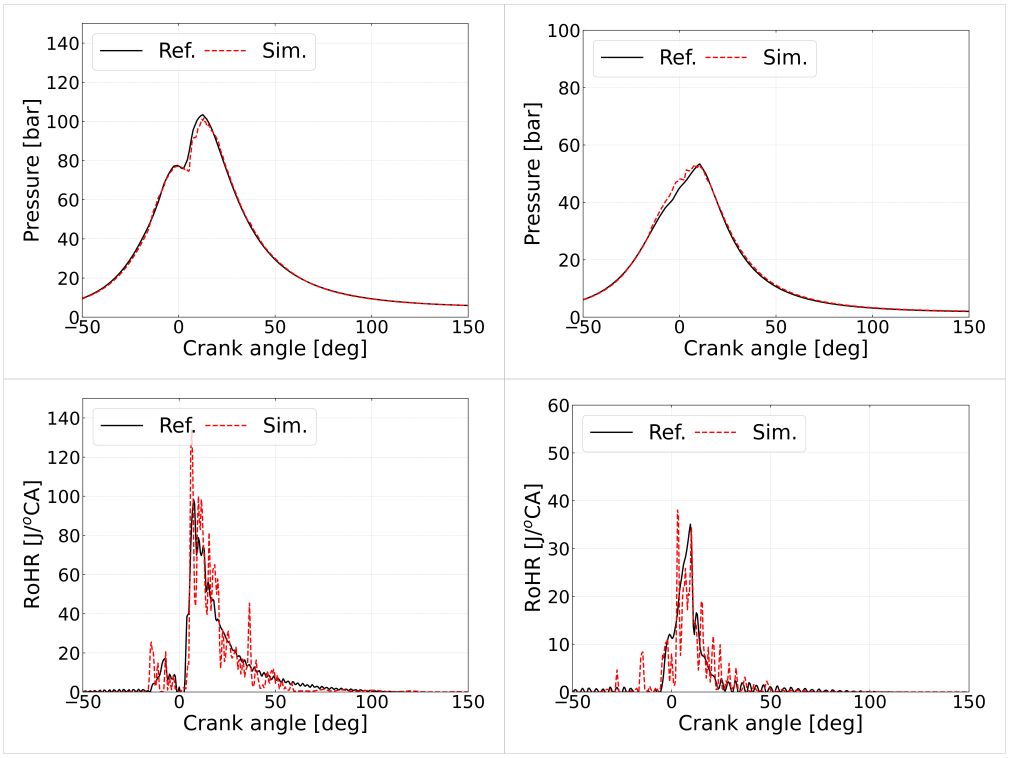

FIGURE 4.4: Comparison between the simulated and the reference pressure and RoHR profiles for operating points 2 and 8 from the Table 4.3.

Simulated exhaust emissions for all the operating points from Table 4.3 are shown in Figure 4.6. For operating points 1, 2, 3, 8, 9, 10, 12, 13, 14 and 16, the CO_2 agrees reasonably with the experimental values. For OP 6,7, and 11, which are among the high load points, the predicted CO_2 is lower than the reference value. Overall, the simulated CO is higher than the experimental one, except for the operating points 5, 8, 9 and 15. For operating points 5, 8 and 9, the experimental value is higher than the optimised CO value. For operating point 15, the predicted CO is almost equal to the experimental one. For all operating points, the simulated HC overpredicts the reference data. Reference NO_x is well matched by simulations for all operating points except for OP 2, 7 and 11, where simulated NO_x values are lower than the experimental values.

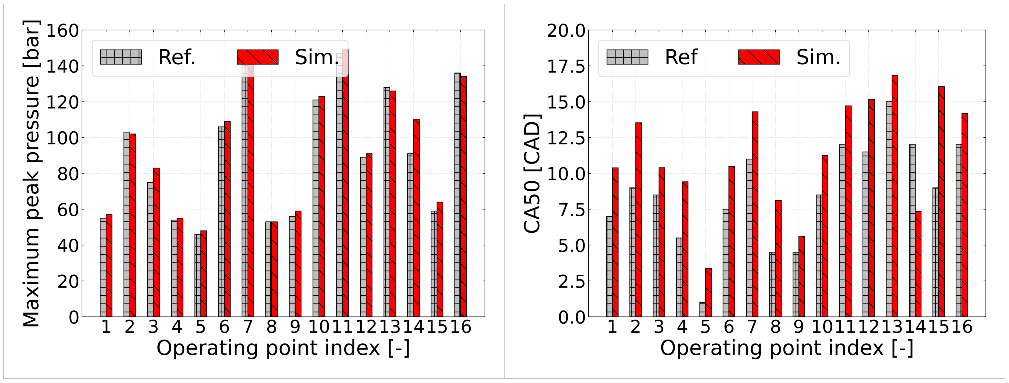

FIGURE 4.5: Simulated maximum peak cylinder pressure and combustion centre compared to the reference data.

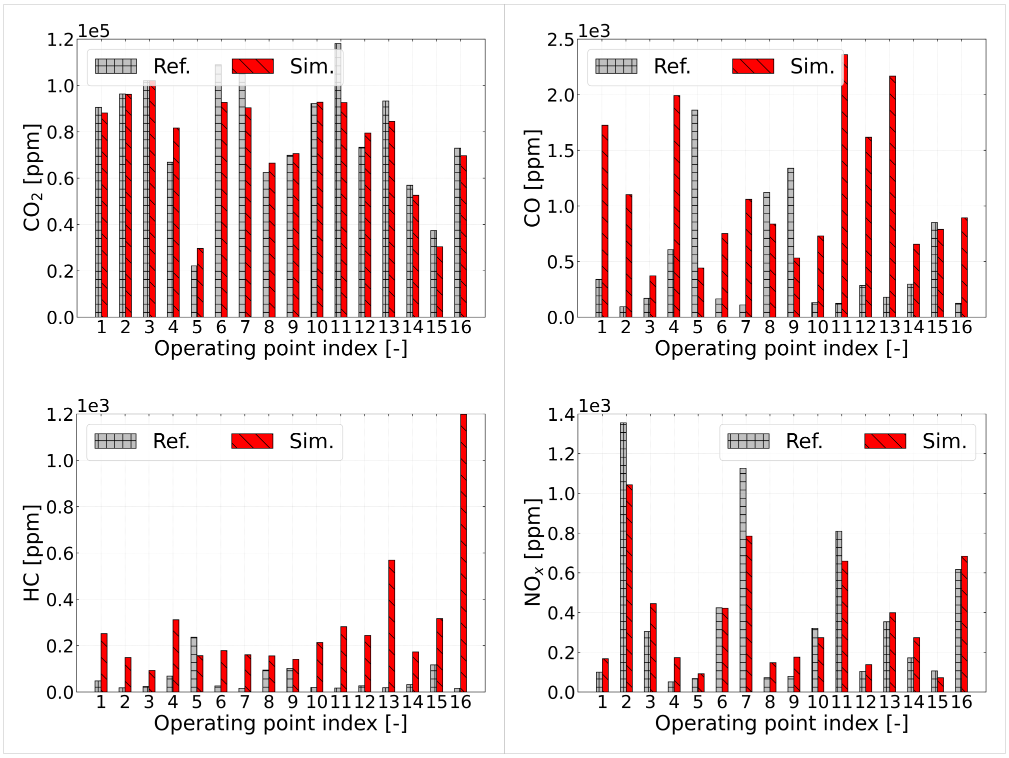

FIGURE 4.6: Simulated CO_2, CO, NO_x and HC compared to the reference data for all the operating points from Table 4.3.

4.3.4 Transient simulation results

The trained engine model is validated against reference data from the WLTP driving cycle.

The results for peak cylinder pressure (PCP) and CA50 are presented in Figure 4.7. Overall, good agreement between the simulated and reference data is obtained.

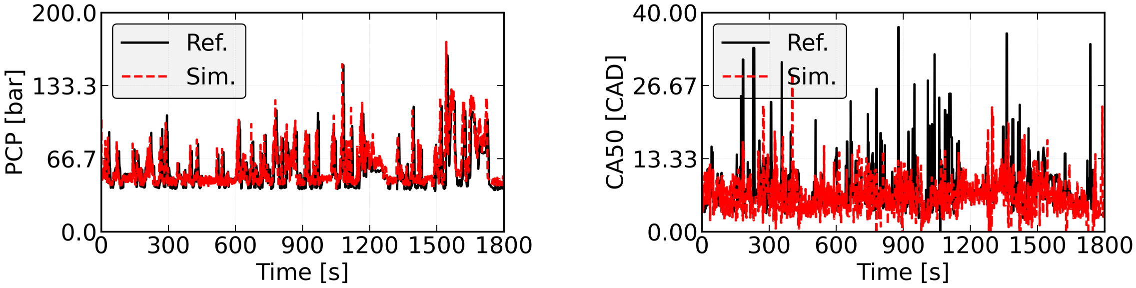

(A) (B)

FIGURE 4.7: Comparison between the simulated and reference results for PCP (A) and CA50 (B).

Figure 4.8-Figure 4.12 presents a comparison between the simulated and reference results for selected emissions, such as CO_2, CO, NO_x, HC and soot, during the WLTP cycle. Overall, quite good agreement is obtained. HC, CO and soot are underestimated during the majority of the cycle, but at around 1500s of the cycle, the concentrations increase, resulting in an increase of the cumulative values that at EVO show a somewhat reasonable match to the reference data. Some overestimation of NO_x is observed after low-pressure EGR is started at around 1200s in the driving cycle [44], but overall, the agreement is high.

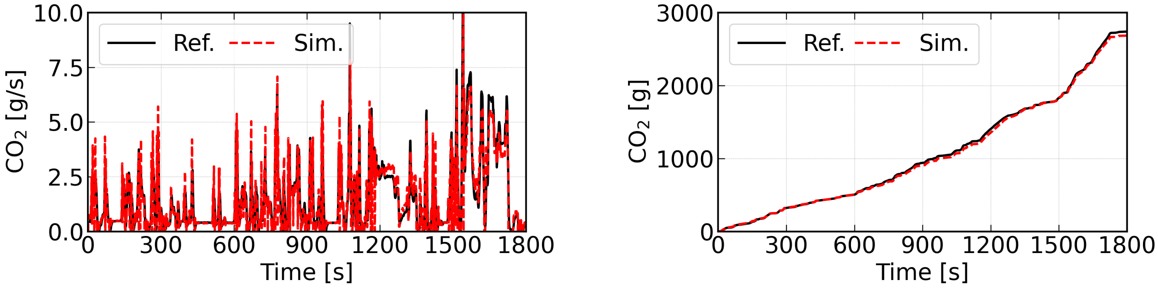

(A) (B)

FIGURE 4.8: Simulated and reference CO_2 as rate (A), and cumulative (B) data.

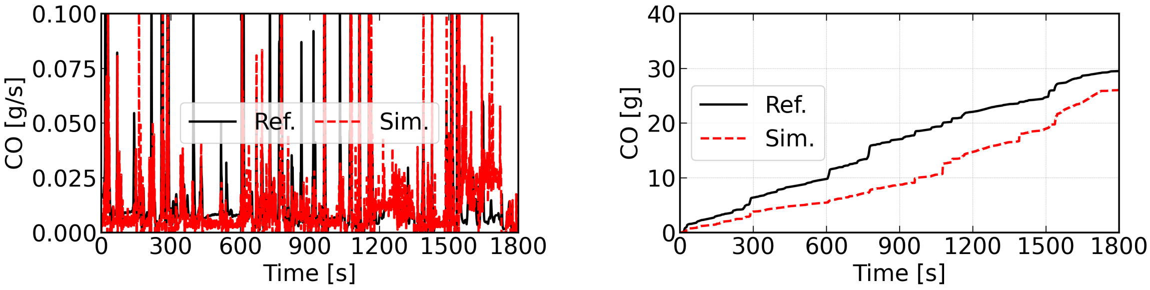

(A)

(B)

FIGURE 4.9: Simulated and reference CO as rate (A), and cumulative (B) data.

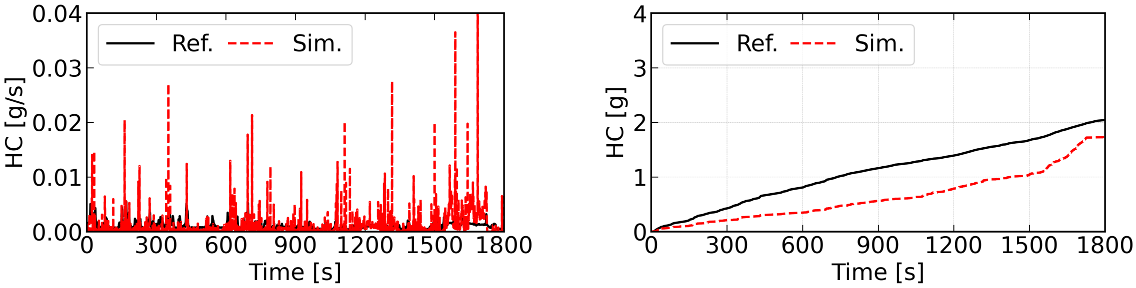

(A)

(B)

FIGURE 4.10: Simulated and reference HC as rate (A), and cumulative (B) data.

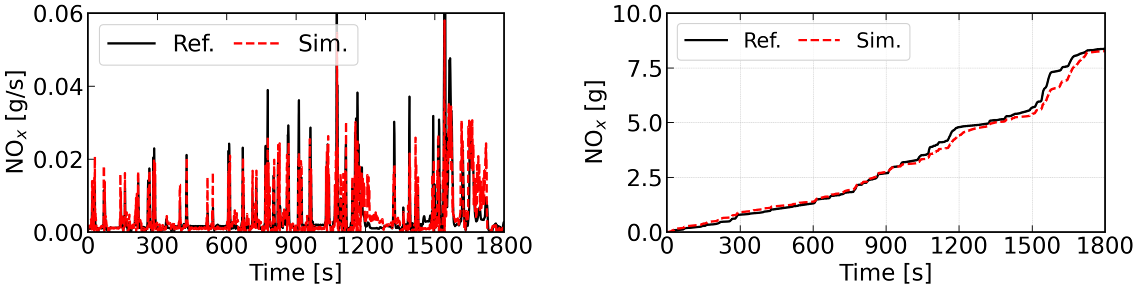

(A)

(B)

FIGURE 4.11: Simulated and reference NO_x as rate and cumulative data.

4.3.5 Analysis of stochastic variation of exhaust emissions

This section investigates the variability of the simulated exhaust emissions in reference to the variability of the measured data. Fifty identical simulations were conducted and compared against experimental accuracy windows (see also Section 3.5.3). The results for CO_2 and CO are presented in Figure 4.13 and Figure 4.14 shows results for NO_x and HC.

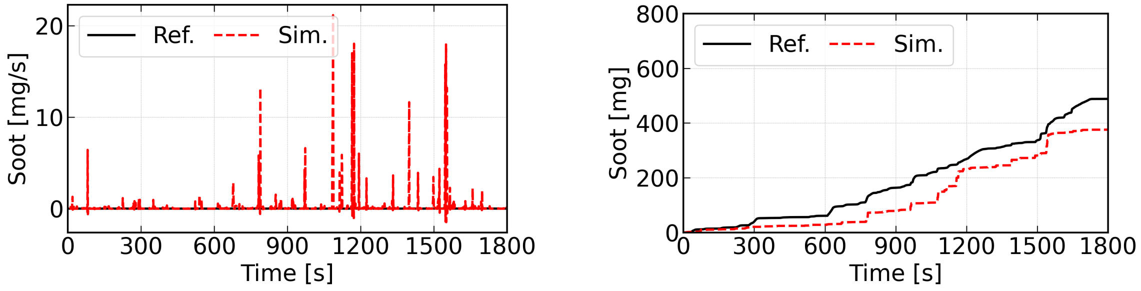

(A) (B)

FIGURE 4.12: Simulated and reference soot as rate and cumulative data.

Overall, for all considered exhaust species, all individual driving cycles at the end of the WLTP cycle (at 1800s) fall into the determined accuracy windows, which are 10%, 30%, 20%, 50% and 60% for CO_2, CO, NO_x, HC and soot, respectively.

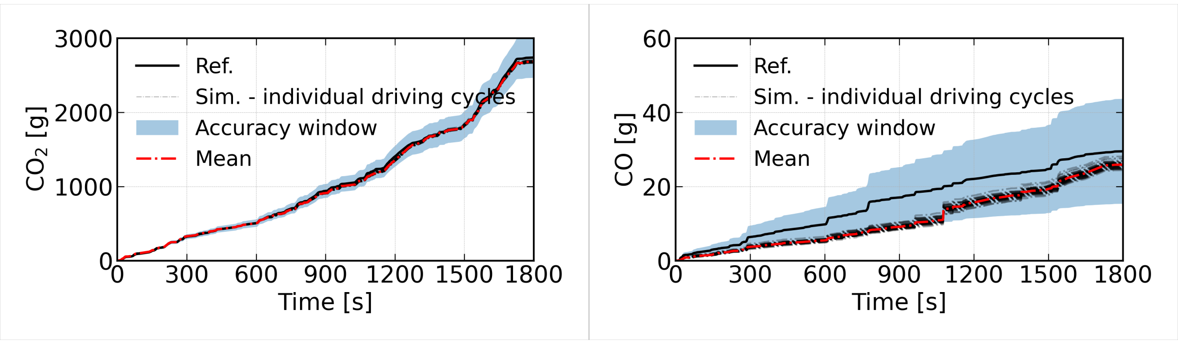

FIGURE 4.13: Cumulative histories of CO_2 and CO from consecutive fifty driving-cycles and their average history compared with reference data and plotted over the accuracy window of test-bench measurement.

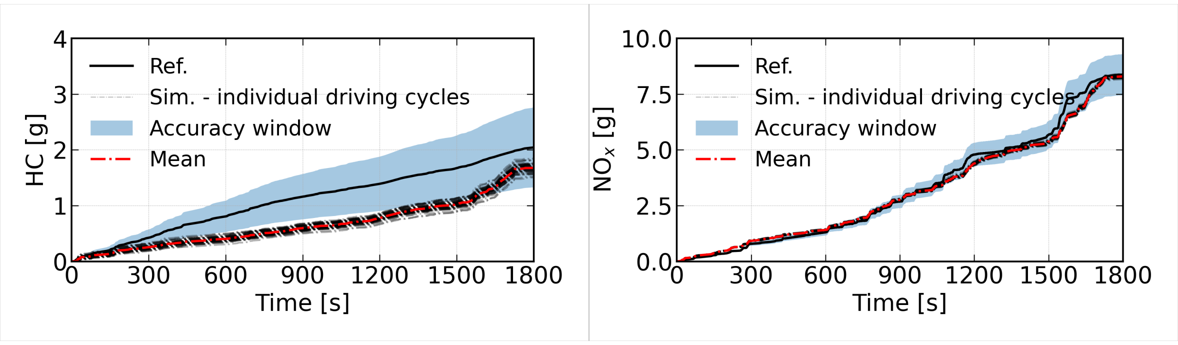

FIGURE 4.14: Cumulative histories of NO_x and HC from consecutive fifty driving-cycles and their average history compared with reference data and plotted over the accuracy window of test-bench measurement.

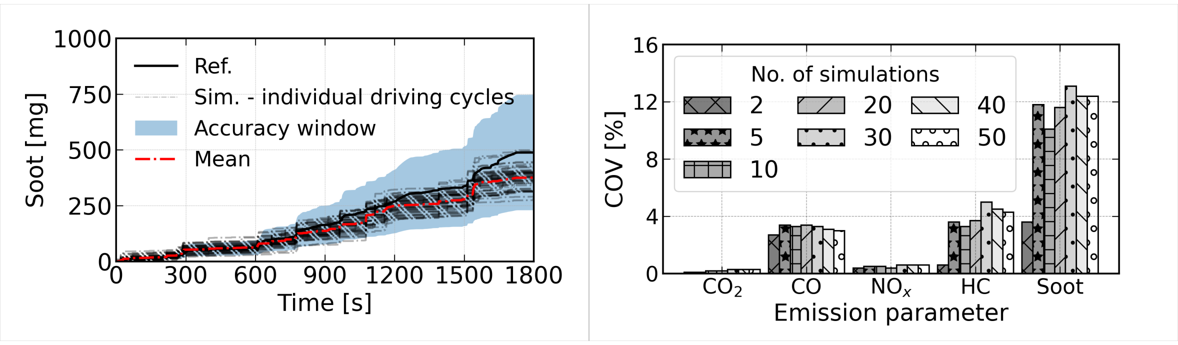

FIGURE 4.15: Cumulative histories of soot from consecutive fifty driving-cycles and its average history compared to the reference data and plotted over the accuracy window of test-bench measurement (left) and coefficient of variance for selected emissions (right).

Right of the Figure 4.15 presents a grouped bar chart showing the coefficient of variance (CV) in % for five considered emission species (CO_2, CO, NO_x, HC, and Soot), across different simulation counts (2, 5, 10, 20, 30, 40, 50 simulations). The CV is the standard deviation divided by the mean of an integrated (cumulative) emissions expressed as a percentage.

$$CV = \frac{\sigma}{\mu} \times 100. \tag{4.1}$$

In the equation 4.1 σ is the standard deviation and μ is the arithmetic mean, the equation 4.1 provides a normalised measure of variability that is independent of the scale of the mean. In the case of simulations, CV examines how much variation can be expected from the mean outcome to other outcomes for each subset of simulations. A low CV means that the simulation results are close to average (such as high consistency), while a high CV indicates stronger fluctuations (less stability or stronger sensitivity).

In Figure 4.15, on the right, each group of bars corresponds to a single species, with different hatch patterns representing different simulation counts. Numerical CV values are annotated above the bars for clarity. CO_2 exhibits very low CV ($\sim$ 0.1–0.3%), indicating highly consistent predictions across simulations. CO and NO_x show moderate variability (0.3–0.6%), with NO_x slightly more sensitive at some simulation counts. HC CV increases gradually ($\sim$ 1–5%), reflecting moderate-to-high sensitivity, while soot shows the highest CV ($\sim$ 10–13%), suggesting substantial stochastic effects or model sensitivity.

Increasing the number of simulations does not uniformly reduce variability. For most species, CV stabilises after $\sim$ 10–20 runs, but soot varies even at 50 simulations. Low CV (CO_2) indicates robust and predictable emissions, moderate CV (CO, NO_x, HC) suggests reasonable stability with some sensitivity. A high CV for soot indicates for high sensitivity of its prediction.

4.3.6 Summary

This section presents a comprehensive evaluation of a developed toolchain applied to a CI engine operating under the WLTP driving cycle.

Initial validation under steady-state operating points demonstrates strong agreement between simulated and experimental combustion metrics, including pressure profiles, RoHR, max pressure, and CA50. Emissions predictions for CO_2, CO, NO_x, and HC show reasonable accuracy.

The trained at steady-state conditions model was applied to simulate the transient engine behaviour under the WLTP cycle. Combustion metrics maintain good alignment with reference data. Emissions trends are well captured. CO_2 and CO match closely with experimental counterparts. Similarly, NO_x is also accurately predicted. Some discrepancy between the simulated and reference data is attributed to the effects of activating low-pressure EGR in the phases of the cycle. HC is consistently underestimated during the majority of the cycle, but its end-cumulative value is found within the accuracy window. Similarly to HC, soot emissions are over-predicted in rate but align cumulatively.

To quantify the stochastic variability of the obtained results from transient simulations, 50 consecutive runs of the WLTP cycle were conducted using identical engine data. Results show that a statistically stable mean for CO_2, CO, and NO_x can be achieved with 15 simulations, while HC and soot require 25 and 35 simulations, respectively. Simulated pollutants fall within experimentally defined accuracy windows, confirming the model's reliability for transient emissions prediction and offering practical guidance on simulation count for robust statistical analysis.

This systematic evaluation demonstrates the toolchain's capability to simulate CI engine behaviour under driving cycles with high accuracy and computational efficiency. As the simulation finishes in 30 minutes of a 30-minute driving cycle, this supports its use in real-time emissions prediction and virtual calibration workflows.

4.4 Simulation WLTP cold start of a CNG engine

This section applies and assesses the developed toolchain for simulating SI engine behaviour during cold start conditions under the WLTP driving cycle for passenger car applications using CNG as fuel. The cold-start phase significantly influences overall cycle emissions and fuel consumption in regulatory testing. The content of this section has been adopted from the published journal article [24].

This section extends the validation to a SI engine fuelled with CNG under cold-start conditions. Experimental reference data were collected from [92, 93], where controlled tests were carried out at four distinct ambient temperatures: −7 °C, 0 °C, 8 °C, and 20 °C. The developed simulation toolchain was applied to replicate these experiments, and its predictions were compared to the measured data at each temperature setting. Furthermore, additional investigations were conducted to assess how Natural Gas (NG) composition influences cold-start emissions. Three representative mixtures were studied: High-caloric Gas (H-Gas):- predominantly methane, exhibiting the highest stoichiometric air–fuel ratio and Wobbe index, Low-caloric Gas (L-Gas):- containing approximately 20% nitrogen, resulting in the lowest Wobbe index and a reduced energy density, Hydrogen-enriched gas:- containing 10% H_2, characterized by a higher Wobbe index and faster flame speeds. The impact of air–fuel ratio (λ) variations was also analysed. For each ambient temperature, λ was incrementally increased from stoichiometric conditions (λ=1.0) to lean mixtures (λ=1.3 and λ=1.6), enabling a systematic evaluation of lean-burn strategies on engine-out emissions and combustion performance. This section provides insights into how fuel properties and mixture settings interact with cold-start phenomena, which are critical for regulatory compliance and practical engine optimisation.

4.4.1 Engine specifications

The specifications of the engine are detailed in Table 4.6. While the engine is originally designed for gasoline use, it has been enhanced with a direct-injection system tailored for natural gas. By leveraging the high octane rating associated with natural gas, the compression ratio was raised from 10:1 to 13:1. The testing apparatus comprises a 250 kW dynamometer functioning at 6000 rpm, capable of conducting both transient and steady-state operations. Continuous monitoring of gas quality is implemented, allowing adjustments through controlled introductions of CO_2, N_2, and H_2. To replicate cold start scenarios, both the oil and coolant circuits are cooled to -7 °C utilising a specialised conditioning unit (refer to B of Figure 4.19). Additionally, the test bench is equipped with an open engine control system that facilitates the customisation of catalyst heating strategies. Measurement capabilities include the AVL AMA i60 for detecting emissions such as CO, CO_2, NO, NO_x, and unburned hydrocarbons; furthermore, a DX4000 FTIR system is employed to measure various gases including CO, CO_2, NO, NO_x, SO_2, NH_3, CH_2O, and CH_4.

TABLE 4.6: Engine characteristic.

Parameter	**Unit**	**Value**
Bore	mm	71.9
Stroke	mm	82.0
Rod Length	mm	137.0
Pin Offset	mm	0.5

4.4.2 Surrogate fuel

The composition of natural gas utilised in the experiment is detailed in Table 4.7, which presents one fuel characterised by a lower superior Wobbe index (Low Ws) and another with a higher superior Wobbe index (High W_s). A surrogate model in the form of CPV has been created based on an average natural gas composition derived from six distinct fuel samples collected during the experiment, and based on the reaction mechanism from [94]. Some more information about the generation of CPV and the laminar flame speed table is found in [24] that stands behind this section.

TABLE 4.7: Natural gas composition for reference and surrogate fuel.

Species / Property	**Low W_s**	**High W_s**	**Surrogate**
CH_4 [mol%]	96.74	97.03	96.85
C_2H_6 [mol%]	1.83	2.18	2.09
N_2 [mol%]	0.60	0.58	0.55
CO_2 [mol%]	0.63	0.11	0.40
H_2 [mol%]	0.00	0.00	0.05
CO [mol%]	0.20	0.10	0.06
AFR_{st}	16.58	16.89	16.71
LHV [MJ/kg]	48.03	47.99	47.06
W_S [MJ/m^3]	47.37	48.06	46.72

4.4.3 SRM configuration

The configuration of the SRM for this study, presented in Table 4.8, is based on the findings from previous research [95], with an adjustment to the particle count, which is increased to 200 to facilitate the demands of transient simulations. Furthermore, the number of cycles for the steady-state model training is established at 150 to accommodate the cyclic fluctuations observed in the experiments. This study employs the cyclic variation model [96], which assumes a Gaussian distribution for parameters such as spark timing (θ_{spark}), scalar mixing time (τ_{φ}), and turbulence frequency (u').

TABLE 4.8: SRM setup.

Parameter	**Value**
Number of particles [-]	200
Time step [^oCA]	0.5
Number of cycles [-]	150

The Woschni heat transfer model [74] used default model constants (C_1=2.2800 and C_2=0.0035), and the piston/head surface area multiplier was set to 1.52. Additionally, the crevice volume is configured to represent 4% of the cylinder clearance volume, which includes unburned mass that becomes trapped during the compression and combustion phases, subsequently released during the expansion stroke.

The K-k turbulence model [60, 61] is used. Its configuration is detailed in Table 4.9. The default values recommended by [97] are employed, with the scalar mixing time factor C_{φ} established at 1. The injection parameter (C_{inj}) is assigned a value of zero, as fuel mass is introduced during the opening of the intake valve, allowing us to disregard the effect of direct injection on turbulent kinetic energy (k).

TABLE 4.9: K-k turbulence model parameters.

Parameter	**value**
C_{inj}	2.2800
C_{comp}	0.0035
C_{tke}	2.2800
C_{diss}	0.0035
C_{len}	2.2800
C_{β}	0.0035
$C_{\Delta,1}$	2.2800
$C_{\Delta,2}$	0.0035
C_{ϕ}	0.0035

4.4.4 Engine steady state operating points

The steady-state operating points are detailed in Table 4.10. This table also presents the standard deviation of spark timing, denoted as σ_{ST}, along with the laminar time ($t_{laminar}$) associated with the early flame kernel model. These parameters were calibrated to align with the in-cylinder pressure observed during experiments. Laminar time characterises the propagation of the laminar flame immediately following spark ignition and remains constant across varying operating conditions. Notably, the standard deviation of spark timing tends to increase with greater torque levels.

TABLE 4.10: Steady-state operating point model training.

ID	Speed [rpm]	Torque [Nm]	σ_{ST} [°CA]	t_{laminar} [µs]
OP1	1050	40	2.1	600
OP2	2000	100	3.1	600
OP3	2500	170	4.1	600
OP4	3000	40	2.1	600
OP5	3000	140	3.1	600
OP6	3500	170	4.1	600
OP7	5000	40	3.1	600
OP8	5000	100	3.1	600
OP9	5000	170	4.1	600

4.4.5 Reference model results at steady state conditions

The steady-state results of the pressure and RoHR is Figure 4.16. The data presented reflect averaged results from 150 cycles of both experimental and simulated conditions. In general, the simulation provides a precise representation of the combustion behaviour observed in the experiments. As this chapter concentrates on the performance of the simulation toolchain under transient conditions, the results for the rest of the steady-state OPs are not presented here, and they are found in [24].

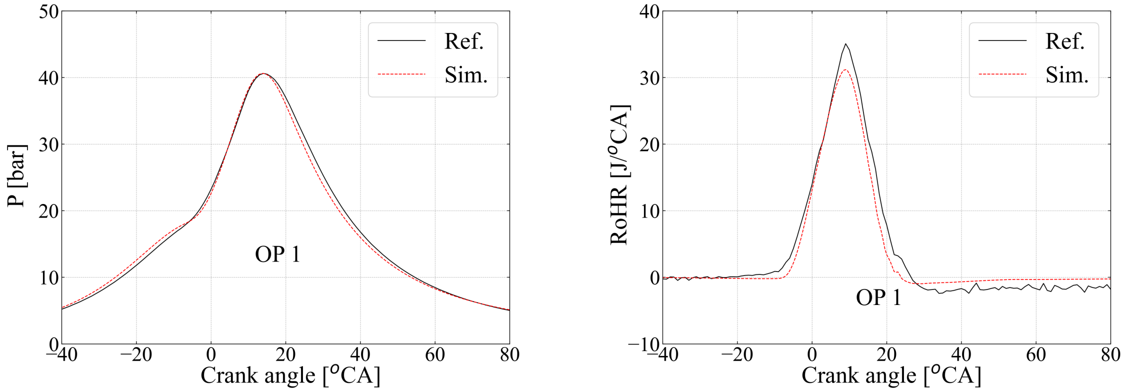

(A) (B)

FIGURE 4.16: Comparison between reference and simulated histories of in-cylinder pressure (A) and RoHR (B) for operating point 1.

Maximum pressure and CO_2 emissions are illustrated in Figure 4.17 A and B, respectively and for all operating points. The predicted values for both max. pressure and CO_2 emissions align closely with experimental results. However, notable discrepancies are observed in OP3. The reference result for OP3 is significantly higher than those recorded for other steady-state conditions, which contradicts expectations based on the provided fuel mass. Consequently, this experimental result is classified as an outlier.

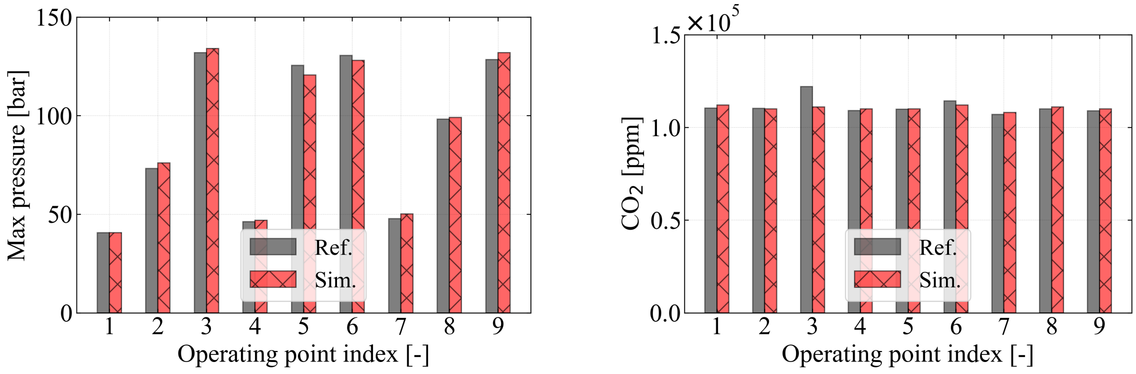

(A)

(B)

FIGURE 4.17: Comparison between reference and simulated maximum peak cylinder pressure (A) and CO_2 (B) for all operating points.

The predicted emissions of CO and NO_x are illustrated in sub-figures 4.18a and 4.18b of 4.18. The results indicate a strong correlation with the experimental data for CO, which exhibits levels between 6000 and 10000 ppm mole fraction. The predicted NO_x emissions align closely with the experimental findings at low-load and mid-load operating conditions. However, for operating points OP3 and OP6, the simulated NO_x values are significantly lower than expected.

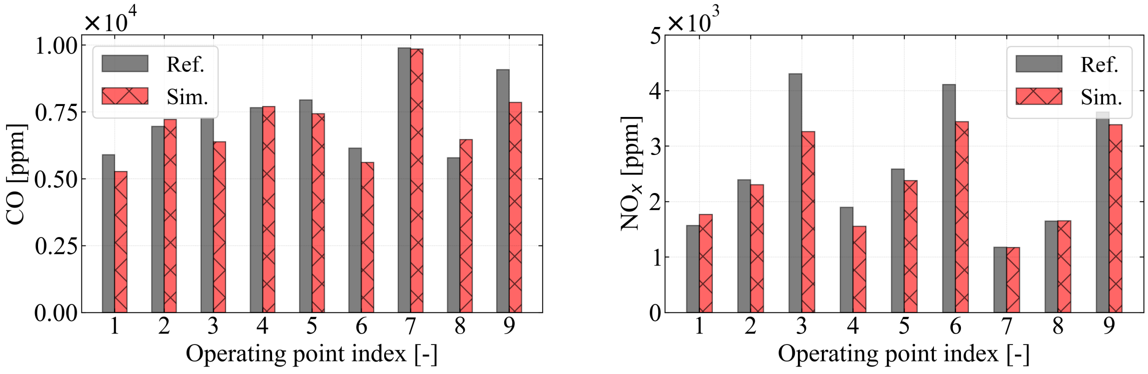

(A)

(B)

FIGURE 4.18: Comparison between reference and simulated CO (A) and NO_x (B) for all operating points.

4.4.6 Transient simulations

The driving cycle analysed is a simplified version of the WLTP, as illustrated in Figure 4.19. The simulations refer to the cold start tests at different ambient temperatures: 20°C, 8°C, 0°C, and -7°C. The histories of intake manifold pressure and temperature due to these different ambient temperatures are illustrated in Figures 4.20 and 4.21

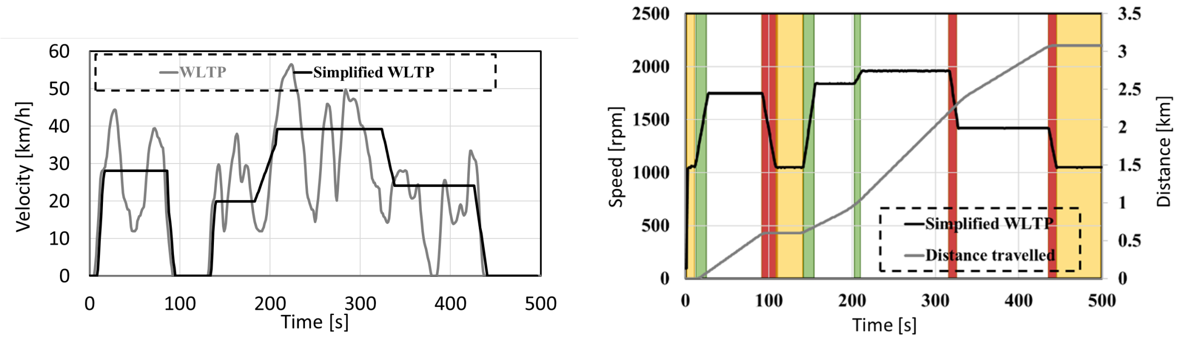

(A) (B)

FIGURE 4.19: (A) WLTP velocity profile compared to the simplified WLTP used in the current investigations. (B) CNG engine speed profile of the simplified WLTP cold start cycle. The yellow colour marks the idling phases, the green colour marks the acceleration phases, and the red colour marks the deceleration phases.

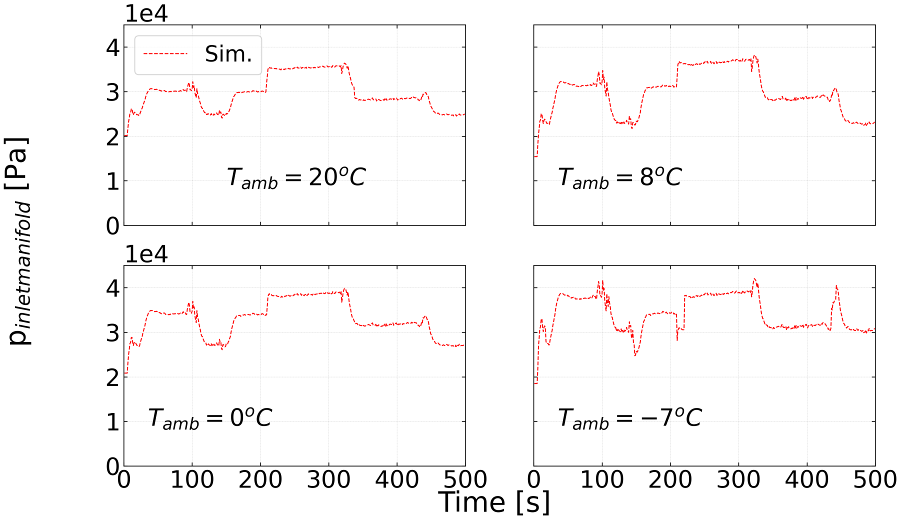

FIGURE 4.20: Simulated inlet manifold pressure at 20^{o}C, 8^{o}C, 0^{o}C and -7^{o}C ambient temperatures.

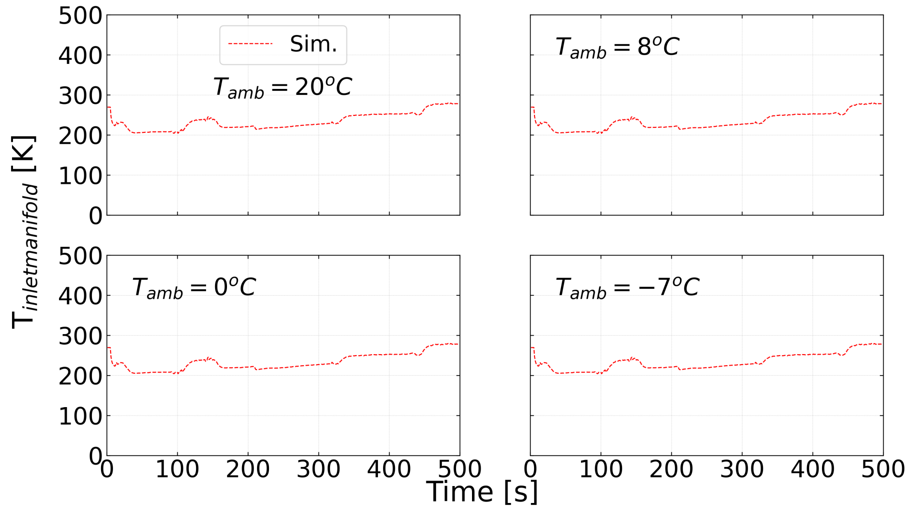

FIGURE 4.21: Simulated inlet manifold temperature at 20^{o}C, 8^{o}C, 0^{o}C and -7^{o}C ambient temperatures.

During a cold start lasting 500 seconds, the inlet manifold temperature increases due to the warming of the engine oil. The engine model accurately reflects the measured natural gas mass flow (mCNG) across all four ambient temperatures, as depicted in Figure 4.22. Notably, natural gas flow rises as ambient temperatures drop, attributed to heightened friction losses at lower temperatures.

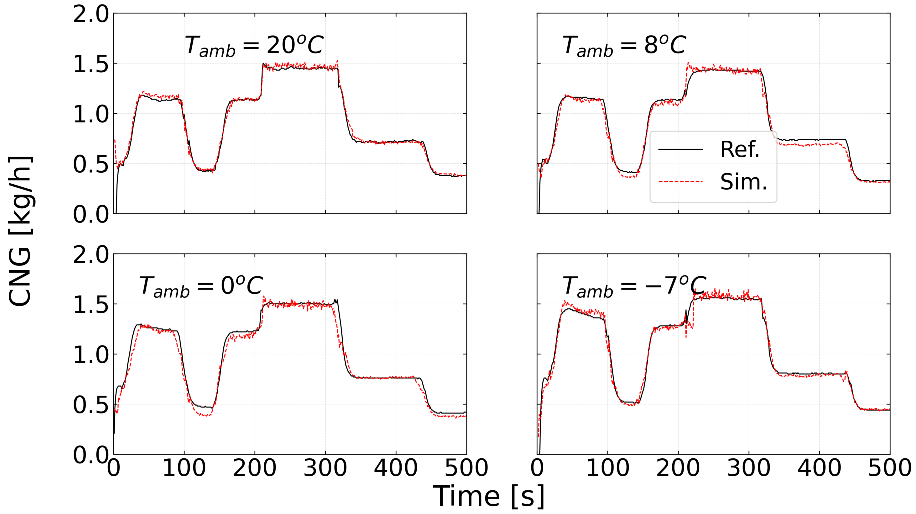

FIGURE 4.22: Comparison between simulated reference mass flow of CNG for different ambient temperatures.

Overall, the predicted CO_2 (Figure 4.23) is in the range of experimental data. However, at the second idling phase (occurring at 100 seconds), measured CO_2 decreases, which is not replicated by the model. Similarly, during both the second and third de-acceleration phases, the trends of the experimental data are not mirrored by the model.

The simulated CO (Figure 4.24) reasonably matches the measured counterpart. During initial idling phases, there is a notable rise and fall during subsequent acceleration phases that aligns with experimental observations. In contrast, fluctuations in CO occur significantly during the second idling phase. Furthermore, post-second and third deceleration phases see an increase in CO that is unpredicted by the model.

The simulated NO_x (Figure 4.25) aligns remarkably well with the experimental results. As the system transitions into the acceleration phase, there is a noticeable increase in NO_x. In the subsequent idling phase at 100 seconds, NO_x declines but stabilises within a range of 200-300 ppm. As ambient temperatures drop, a decrease in NO_x is observed, which is attributed to the influence of lower cylinder temperatures impacting the thermal NO_x formation path.

For CH_4 (Figure 4.26), there is a reasonable correlation with experimental data throughout both the initial idling and subsequent cruise phases. Nevertheless, the significant surge observed during the second idling phase and during both de-acceleration phases is not captured by the model. This discrepancy may be due to an intensified flame quenching effect occurring during these periods, leading to elevated unburned CH_4 emissions that are not accounted for in the model. The current model lacks a flame-wall quenching component and thus cannot simulate this phenomenon accurately. Additionally, at an ambient temperature of -7^{o}C, experimental observations indicate heightened unburned CH_4 emissions during both initial idling and acceleration phases, which potentially result from flame quenching against cold cylinder walls.

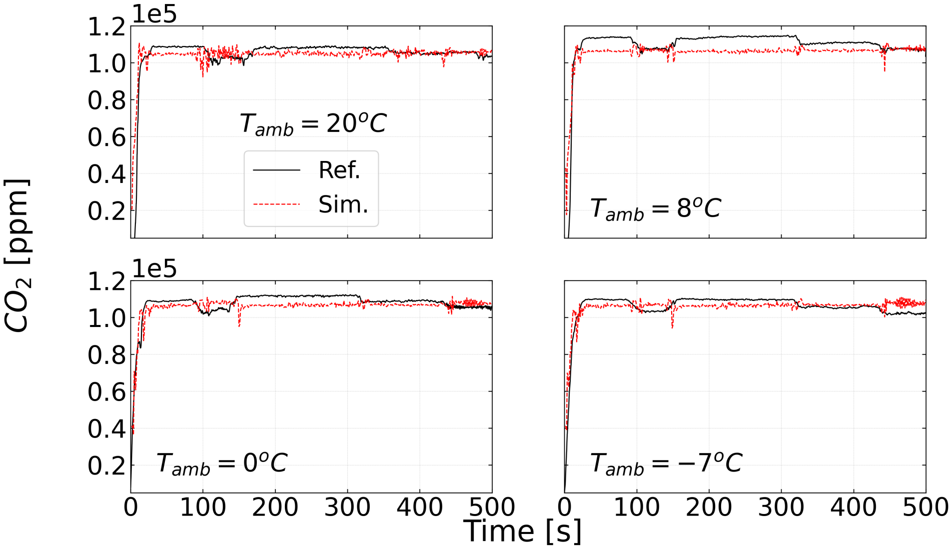

FIGURE 4.23: Simulated and reference CO_2 during the driving cycle and for different ambient temperatures.

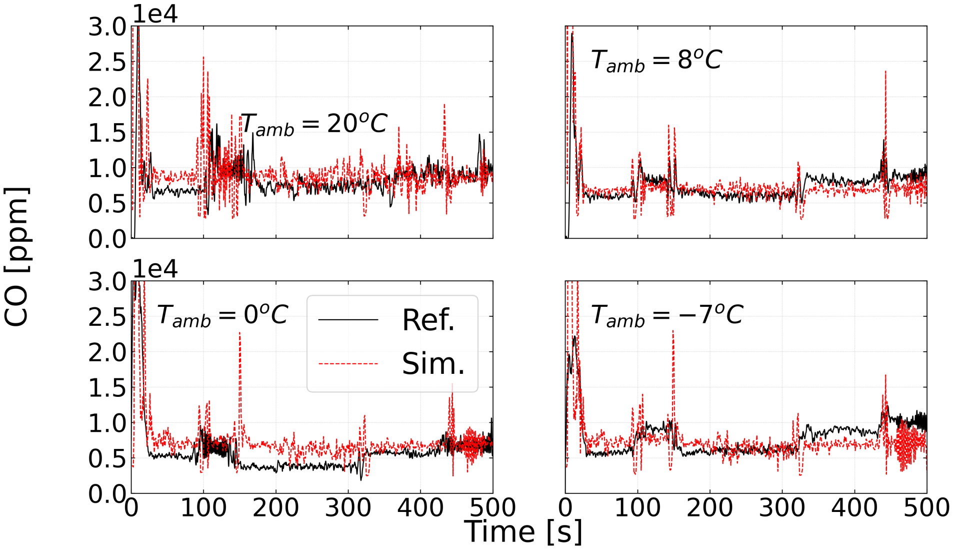

FIGURE 4.24: Simulated and reference CO during the driving cycle and for different ambient temperatures.

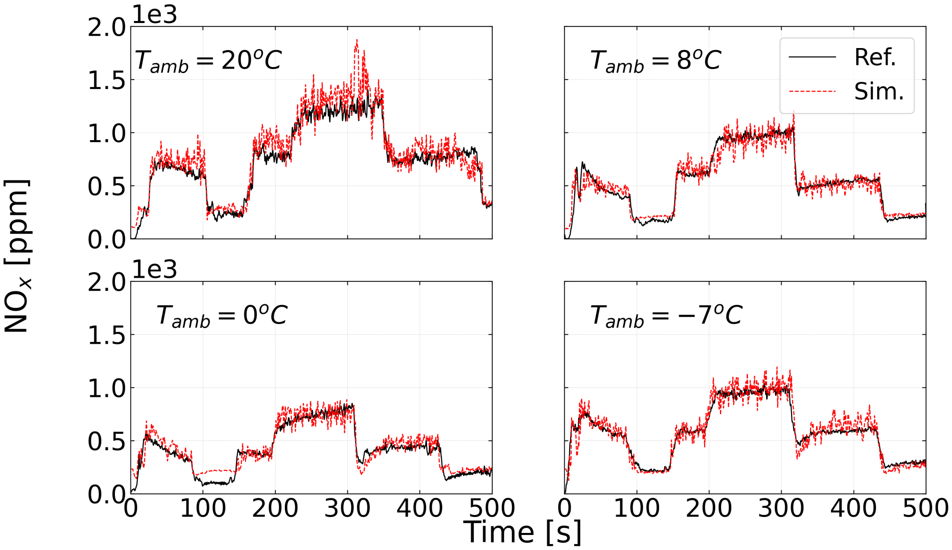

FIGURE 4.25: Simulated and reference NO_x during the driving cycle and for different ambient temperatures.

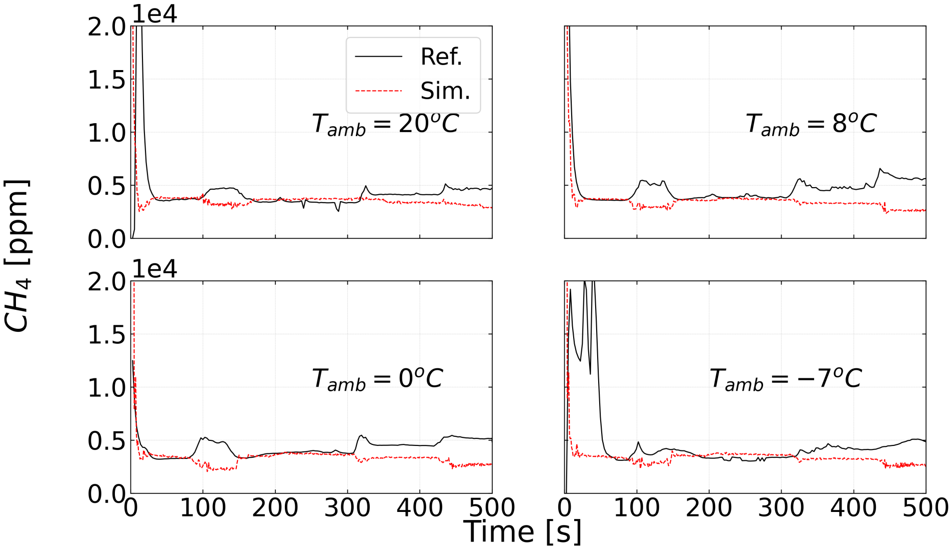

FIGURE 4.26: Simulated and reference CH_4 during the driving cycle and for different ambient temperatures.

The summary of the prediction of engine-out emissions is shown in Figure 4.27, which presents cumulative results at EVO. Overall, the engine model captures the trend of CO_2, NO_x, and CO emissions for different ambient temperatures. For CH_4, the model shows a slight increase for decreasing ambient temperatures, but is not able to closely capture the trend of the experimental data. The incorporation of flame-wall quenching could improve the predictability of the engine model at low ambient temperatures.

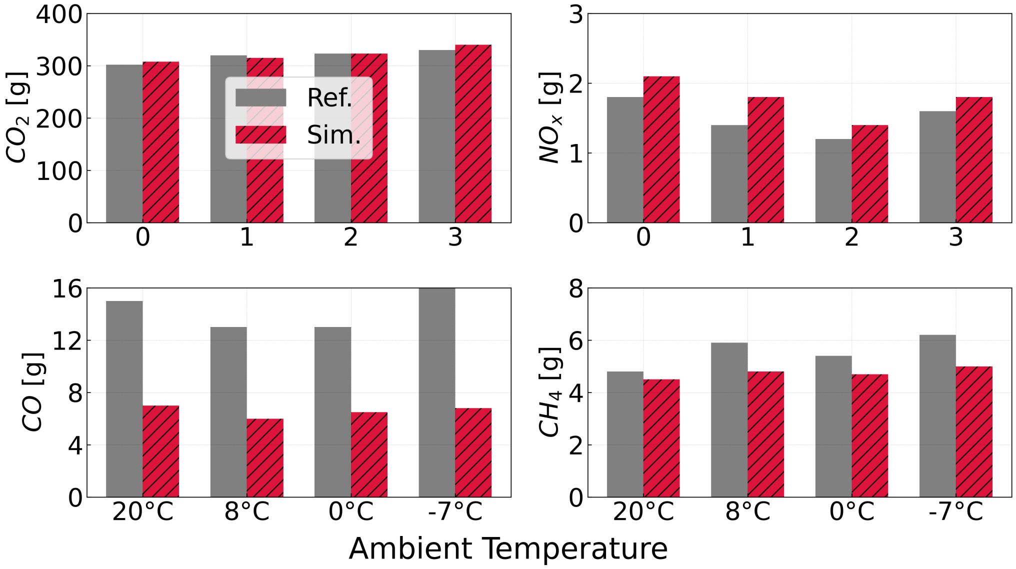

FIGURE 4.27: Simulated and reference emissions at EVO and for different ambient temperatures.

Effect of NG composition on engine-out emissions at different ambient temperatures

The influence of NG composition on emissions produced during cold start engine operations is examined for three distinct fuels, as outlined in Table 4.11. The High-caloric Gas (H-Gas) is characterised by its elevated methane (CH4) content. Conversely, the Low-caloric Gas (L-Gas) consists of 20% nitrogen (N2) within its mixture, exhibiting the lowest stoichiometric air-fuel ratio and Wobbe index. The third fuel variant incorporates 10% hydrogen (H2) in its formulation and boasts the highest Wobbe index among the three. To maintain consistent torque levels with the reference H-Gas fuel, adjustments are made to the fuel mass for both L-Gas and the 10% H2 blends. Notably, the relative air-fuel ratios remain identical across all three fuels.

TABLE 4.11: Natural gas compositions.

	H-Gas	**L-Gas**	**10% H_2**
CH_4 [-]	96.85	77.91	87.18
C_2H_6 [%]	2.09	1.68	1.88
N_2 [%]	0.55	20.0	0.05
CO_2 [%]	0.48	0.39	0.43
H_2 [%]	0.02	0.02	10.0
C_3H_8 [%]	0.01	0.01	0.01
AFR_{st} [-]	16.74	11.85	16.98
ρ [kg/m^3]	0.71	0.87	0.36
LHV [MJ/kg]	48.94	34.64	49.96
Ws [MJ/m^3]	46.72	36.61	47.35

The simulated exhaust temperature at EVO, as depicted in Figure 4.28, reveals that L-Gas fuel exhibits a lower temperature. This observation suggests reduced combustion temperatures within the cylinder. Additionally, there is a noticeable decline in exhaust temperature corresponding to lower ambient temperatures.

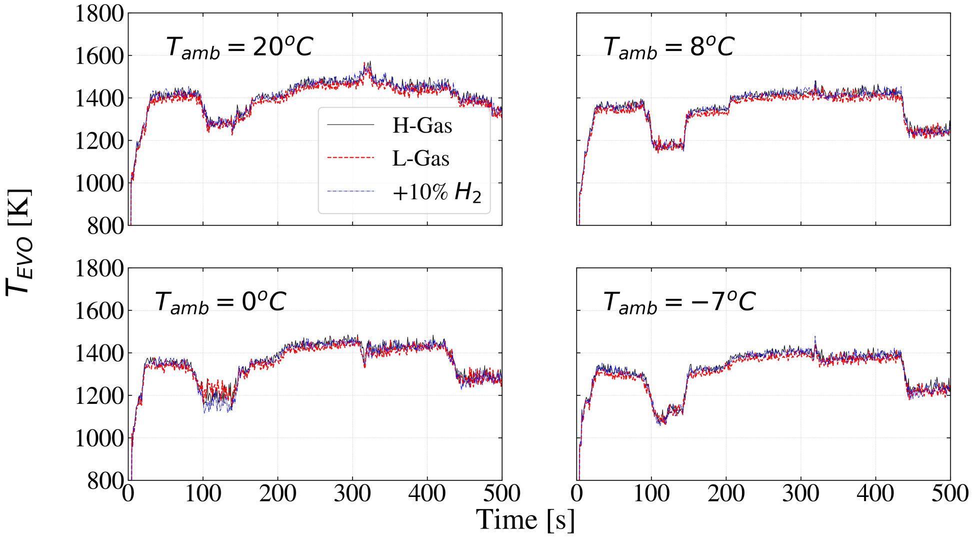

FIGURE 4.28: Comparison of exhaust temperature at EVO for H-Gas, L-Gas and 10% H_2 enriched natural gas for different ambient temperatures.

In Figure 4.29, the cumulative mass of CO_2 is illustrated. Across all four ambient temperatures, H-Gas fuel yields the highest CO_2 emissions due to its superior atom-based C/H ratio compared to the other fuels investigated (H-Gas: 1.0155/4.0008; L-Gas: 0.8169/3.2183; 10% H2: 0.9141/3.8011). At an ambient temperature of 20°C (and -7°C), the cumulative CO_2 mass recorded after a cold start lasting 500 seconds for H-Gas, L-Gas, and 10% H2 fuels is 305g (346g), 300g (340g), and 294g (334g) respectively. As ambient temperature decreases, the CO_2 mass increases due to increased fuel injection aimed at compensating for the elevated friction losses associated with colder engine oil.

The cumulative CO mass is shown Figure 4.30. For 20°C (-7°C) ambient temperature, the cumulative CO mass for H-Gas, L-Gas and 10% H2 fuels is 16g (15g), 16g (14.9g) and 16g (14.9g) respectively. Hence, no significant change of CO mass is found by changing the natural gas composition. For decreasing ambient temperature, the CO mass is decreasing, while it increases again for -7°C due to lower combustion efficiency during the initial 100 seconds of the cold start.

The cumulative NO_x mass is shown in Figure 4.31. For 20°C (-7°C) ambient temperature, the cumulative NO_x mass for H-Gas, L-Gas and 10% H_2 fuels is 2.02g (1.74g), 1.6g (1.3g) and 2.14g (1.87g) respectively. The NO_x mass is increasing the most during the high torque phase at 200 - 300 seconds because of the higher combustion temperature. The higher NO_x mass of the 10% H_2 fuel is because of advanced combustion and higher combustion temperature. The higher H_2 content in the natural gas increases the laminar burning velocity compared to H-Gas and L-Gas fuels, whereby the burn duration is reduced.

The cumulative CH_4 mass is shown in Figure 4.32. For 20°C (-7°C) ambient temperature, the cumulative CH4 mass for H-Gas, L-Gas and 10% H2 fuels is 4.56g (4.81g), 4.4g (4.6g) and 4.4g (4.6g) respectively. The higher CH_4 content for H-Gas fuel impacts the higher cumulative unburned CH_4 mass at the end of the cold start. For all three fuels, the CH_4 mass is increasing with lower ambient temperature because of lower combustion efficiency.

The cumulative H_2 mass is compared in Figure 4.33 for H-Gas, L-Gas and 10% H_2 enriched fuel at different ambient temperatures. For 20°C (-7°C) ambient temperature, the cumulative H2 mass for H-Gas, L-Gas and 10% H_2 fuels is 292mg (278mg), 286mg (269mg) and 356mg (344mg) respectively. The increased H_2 content for the 10% H_2 fuel is the reason for the higher cumulative H_2 mass after cold start.

The cumulative CH_2O mass is shown in Figure 4.34. For 20°C (-7°C) ambient temperature, the cumulative CH4 mass for H-Gas, L-Gas and 10% H2 is 7.7mg (14.3mg), 8.45mg (15.9mg) and 10.1mg (15.34mg) respectively. At 20 °C ambient temperature, the higher CH_2O mass for the 10% H_2 fuel is caused by a strong increase during the initial idling phase, while during the subsequent phases the change of CH_2O mass is similar to H-Gas and L-Gas fuels. With decreasing ambient temperature, the CH_2O mass continues to rise, while no clear trend depending on the natural gas composition can be observed. The strongest increase for

CH_2O mass is found during the first 100 seconds of the cold start, when the air-fuel mixture is fuel-rich, and the cylinder temperature is still low.

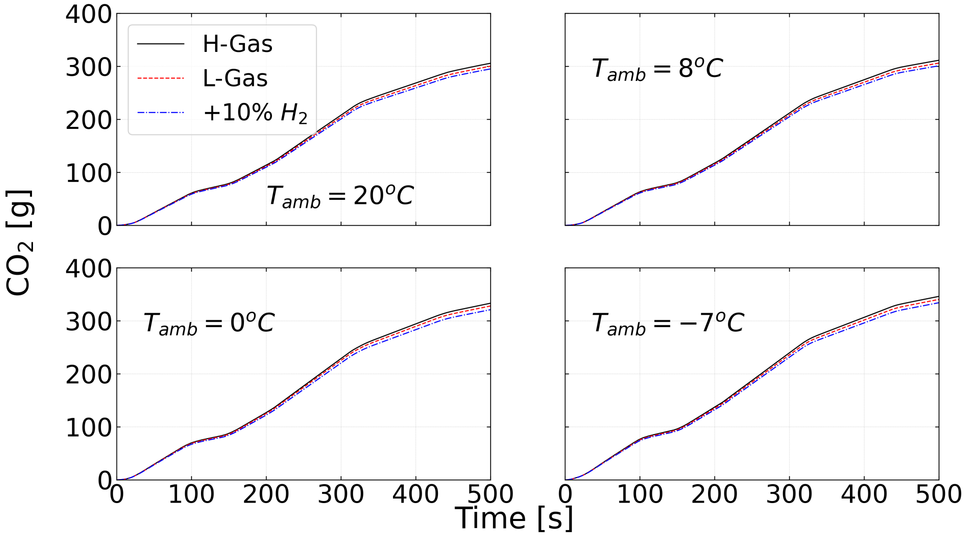

FIGURE 4.29: Comparison of cumulative CO2 mass for H-Gas, L-Gas and 10% H_2 enriched natural gas for different ambient temperatures.

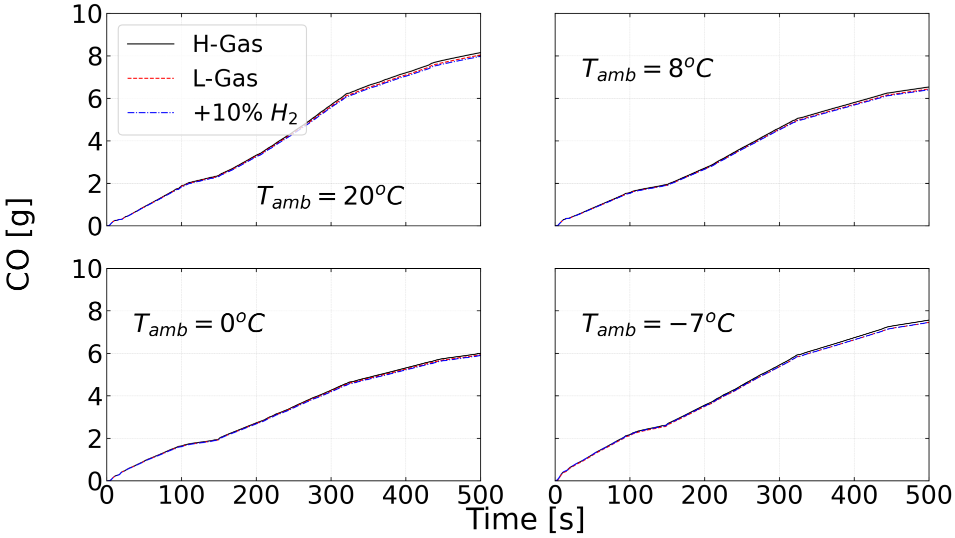

FIGURE 4.30: Comparison of cumulative mass of CO for H-Gas, L-Gas and 10% H_2 enriched natural gas for different ambient temperatures.

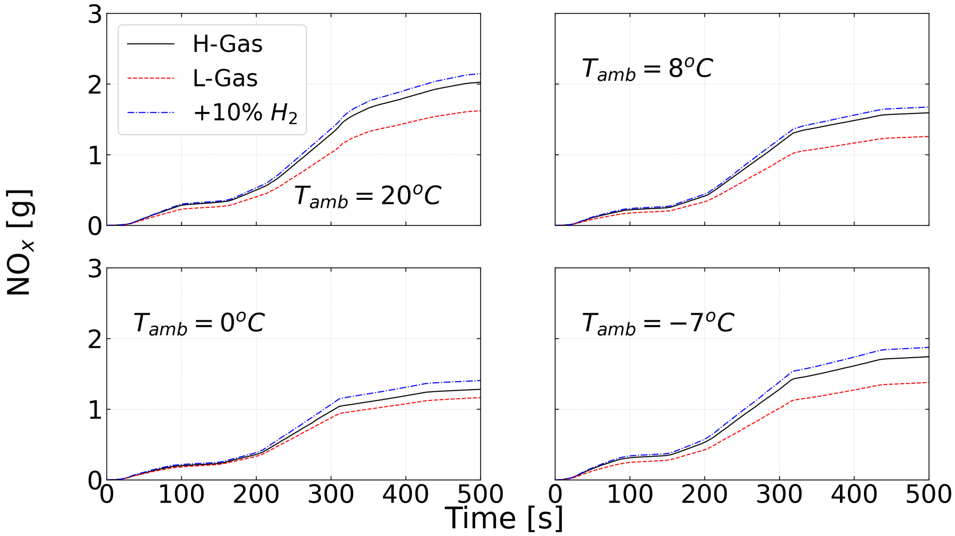

FIGURE 4.31: Comparison of cumulative mass of NO$_x$ for H-Gas, L-Gas and 10% H$_2$ enriched natural gas for different ambient temperatures.

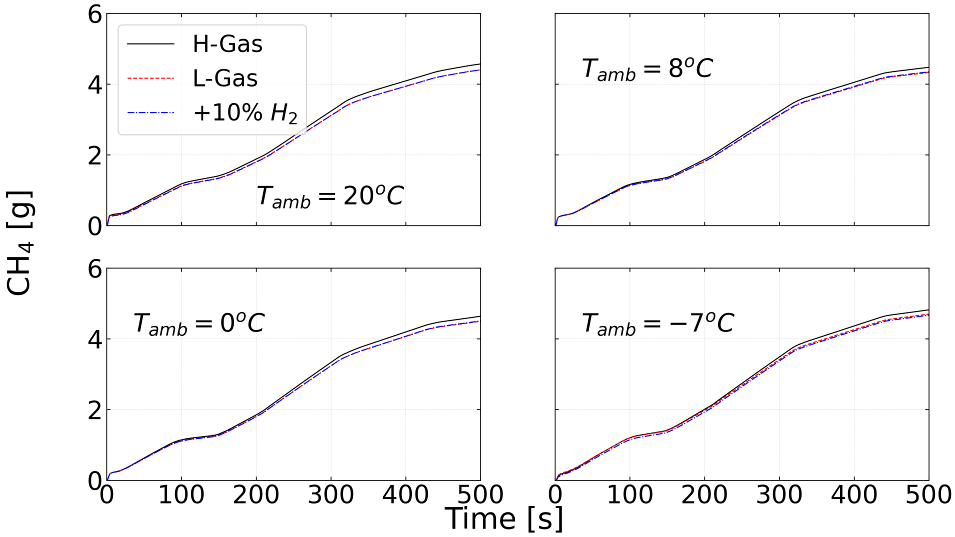

FIGURE 4.32: Comparison of cumulative mass of CH$_4$ for H-Gas, L-Gas and 10% H$_2$ enriched natural gas for different ambient temperatures.

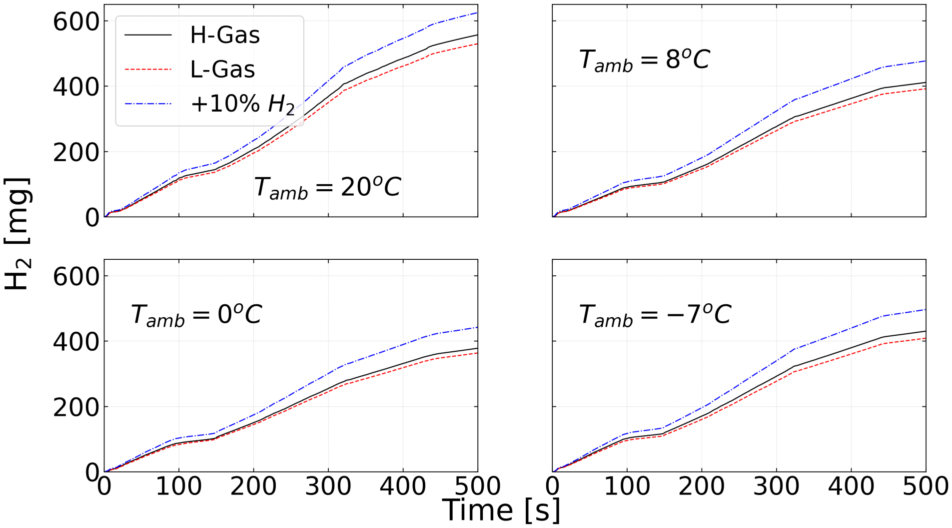

FIGURE 4.33: Comparison of cumulative mass of H_2 for H-Gas, L-Gas and 10% H_2 enriched natural gas for different ambient temperatures.

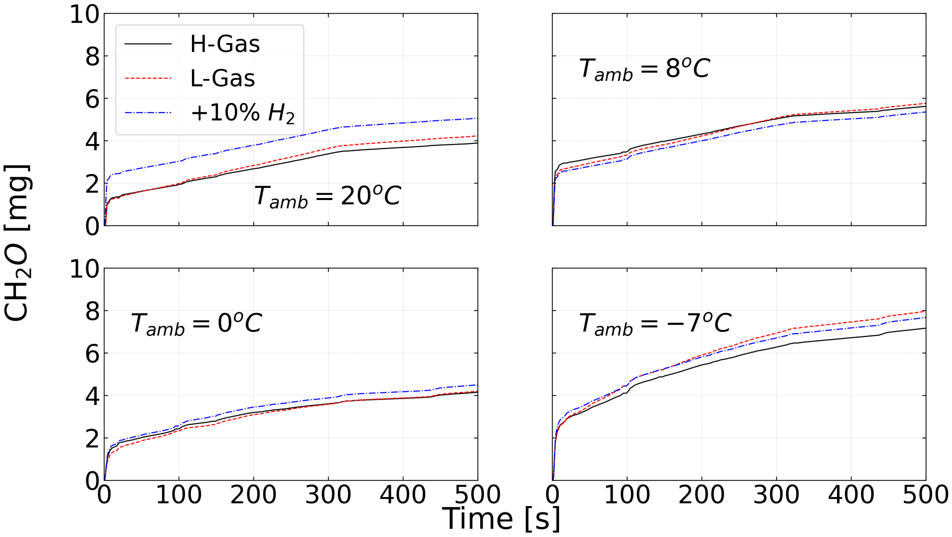

FIGURE 4.34: Comparison of cumulative mass of CH_2O for H-Gas, L-Gas and 10% H_2 enriched natural gas for different ambient temperatures.

The predicted engine-out CO_2 mass per kilometre for the different natural gas compositions is compared to the Euro 6 emission limit of 95g/km in left side of the Figure 4.35. The Euro 6 emission limit is valid for tailpipe emissions, while here we consider engine-out emissions. The CO_2 emissions of 96g/km are achieved using 10% H2-enriched natural gas at 20°C ambient temperature and are closest to the Euro 6 emission limit. The highest CO_2 emissions are predicted for H-Gas because of the higher C:H ratio of the fuel. For decreasing ambient temperature, the CO_2 mass per kilometre is increasing to 112g/km because of higher fuel consumption.

The predicted engine-out NO_x mass per kilometre in the right side of Figure 4.35, is significantly higher for all investigated natural gas fuels compared to the Euro 6 emission limit. This highlights the necessity of an additional after-treatment system to reduce the tail-pipe NO_x emissions. The highest NO_x emissions of 0.7g/km are produced at 20°C ambient temperature using the 10% H_2 enriched natural gas fuel because it burns at higher combustion temperatures. Generally, the NO_x emissions decrease with decreasing ambient temperature, while additional fuel injection at -7°C ambient temperature increases NO_x emissions again. The lowest NO_x emissions of 0.35g/km are predicted at 0°C ambient temperature using L-Gas fuel.

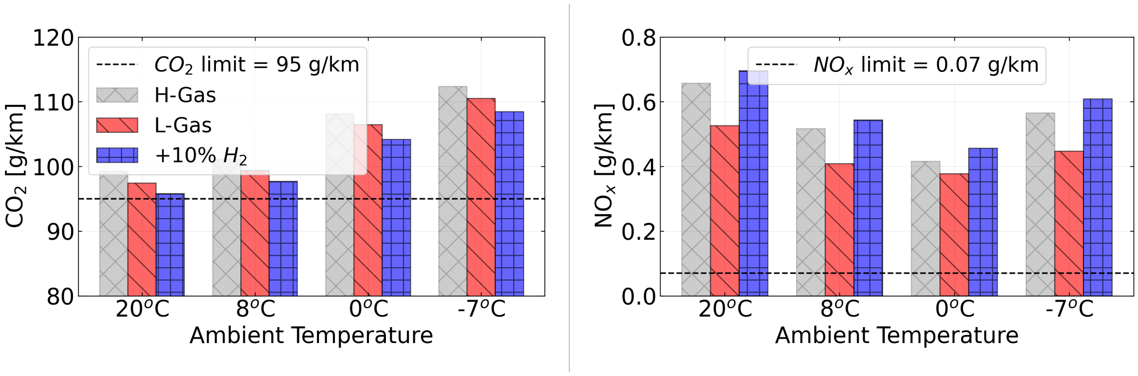

FIGURE 4.35: Comparison of (left) CO_2 (right) NO_x mass per kilometre for H-Gas, L-Gas and 10% H2-enriched natural gas for different ambient temperatures, where the dashed line shows the Euro 6 emission target for CO_2.

The predicted CH_4 mass per kilometre in left side of Figure 4.36 is significantly increased for all investigated natural gas fuels and ambient temperatures compared to the Euro 6 emission limits. For L-Gas and 10% H_2 enriched natural gas the CH_4 emissions are reduced by 50mg/km compared to H-Gas for all ambient temperatures. Further, the need of an after-treatment system for CH_4 emissions is evident from the high CH_4 masses in the exhaust manifold to achieve the Euro 6 emission limits of 10mg/km. The increase of CH_4 mass with decreasing ambient temperature indicates higher conversion rates of the after-treatment catalyst are required at low ambient temperature. This requires sophisticated catalyst heating strategies at low ambient temperatures to reach the high temperatures needed for efficient catalyst operation. At ambient temperature of 20°C, 8°C and 0°C all investigated fuels show lower CH_2O emissions as shown in right side of Figure 4.36 compared to Euro 6 emission limit of 5mg/km. At -7 °C ambient temperature, the predicted CH_2O emissions increase because of lower combustion efficiency. The highest CH_2O emissions of 5.2mg/km are predicted for L-Gas at -7°C ambient temperature.

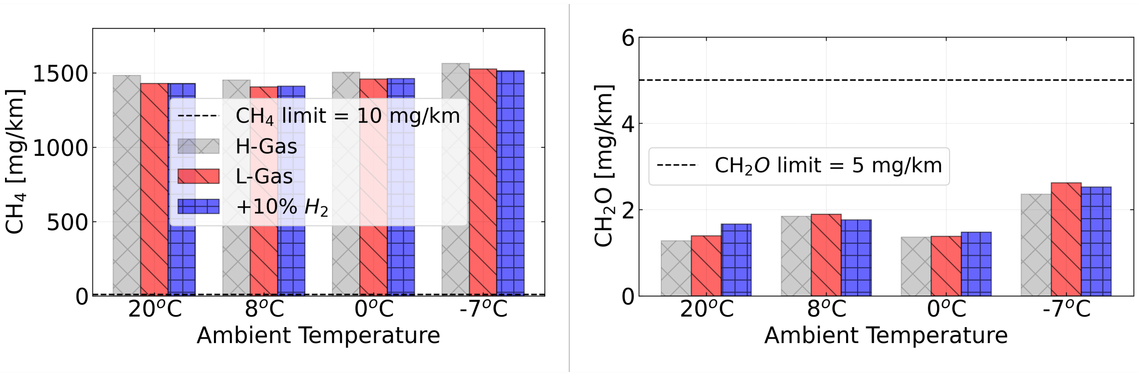

FIGURE 4.36: Comparison of (left) CH_4 (right) CH_2O mass per kilometre for H-Gas, L-Gas and 10% H2-enriched natural gas for different ambient temperatures, where the dashed line shows the Euro 6 emission target for CH_4.

Effect of air-fuel ratio on engine-out emissions at different ambient temperatures

In this subsection, the toolchain is applied to investigate the effect of air–fuel ratio variation on exhaust emissions. Lean combustion is widely adopted in SI engines to reduce fuel consumption and exhaust output [98]. Under lean conditions, NO_x emissions can be substantially lowered owing to reduced peak combustion temperatures, while engine efficiency may be improved. Consequently, the influence of lean operation on performance and engine-out emissions is assessed under cold-start conditions, with the air–fuel ratio varied at $\lambda = 1.0$, $\lambda = 1.3$, and $\lambda = 1.6$.

The simulated indicated torque is presented in Figure 4.37. Increasing λ from 1.0 to 1.3 permits stable operation at comparable torque levels, even under low ambient temperatures. However, further raising λ to 1.6 provides stable operation only at 20°C, while at reduced ambient conditions the engine response becomes erratic. In particular, torque losses are observed during the first cruise and the second idling phase at around 100 seconds. At 0°C and –7°C, the target torque cannot be achieved during the later cruise phases of the cold-start cycle.

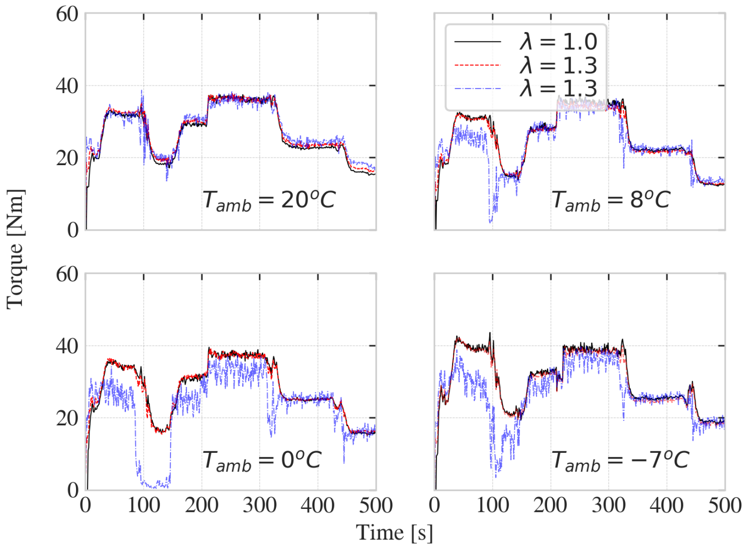

FIGURE 4.37: Comparison of cumulative CO_2 mass for λ=1.0, λ=1.3 and λ=1.6 for transient cold start at 20^{o}C, 8^{o}C,, for λ=1.0, λ=1.3 at 0^{o}C and -7^{o}C ambient temperatures.

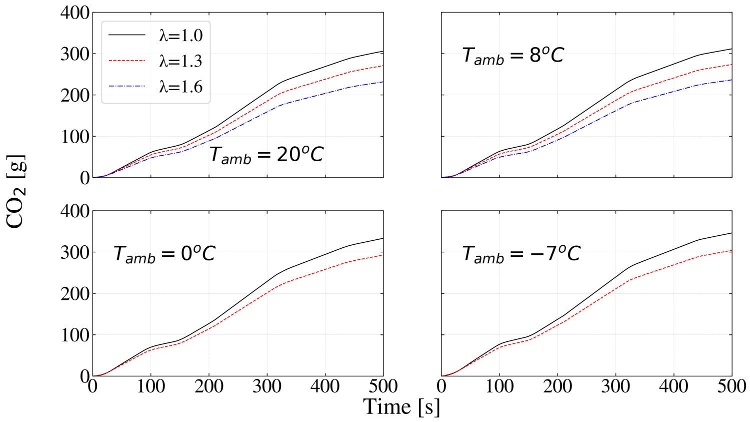

FIGURE 4.38: Comparison of torque for λ=1.0, λ=1.3 and λ=1.6 for transient cold start at 20^{o}C, 8^{o}C,, for λ=1.0, λ=1.3 at 0^{o}C and -7^{o}C ambient temperatures.

A comparison of exhaust emissions is carried out for $\lambda = 1.0$ and $\lambda = 1.3$ across 20°C, 8°C, 0°C, and –7°C. Since the predicted torque for $\lambda = 1.6$ at 0°C and –7°C is considerably lower than the experimental values, the intended speed/distance profile cannot be reproduced, and therefore emissions under these conditions are not evaluated. The simulated cumulative CO_2 mass for different λ values is depicted in Figure 4.38. With leaner mixtures, total CO_2 decreases: at 20°C, the accumulated mass is 305 g, 270 g, and 231 g for $\lambda = 1.0$,

$\lambda = 1.3$, and $\lambda = 1.6$, respectively. For $\lambda = 1.6$ at 20°C and 8°C, the simulated CO_2 corresponds to 77 g/km and 78 g/km. Thus, operation at $\lambda = 1.6$ makes it possible to comply with the Euro 6 CO_2 target of 95 g/km at both 20°C and 8°C.

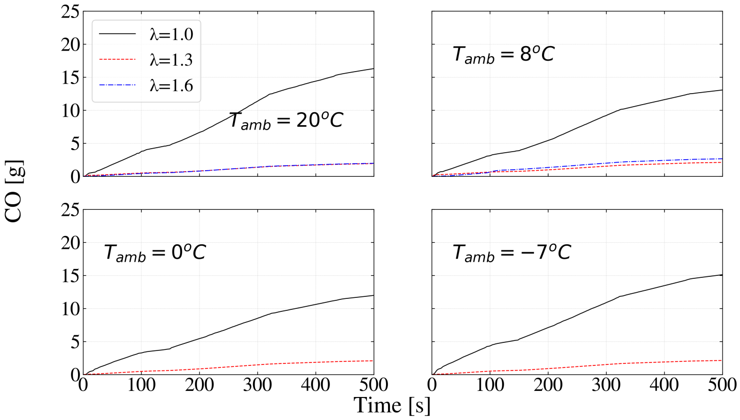

FIGURE 4.39: Comparison of cumulative CO mass for λ=1.0, λ=1.3 and λ=1.6 for transient cold start at 20^{o}C, 8^{o}C,, for λ=1.0, λ=1.3 at 0^{o}C and -7^{o}C ambient temperatures.

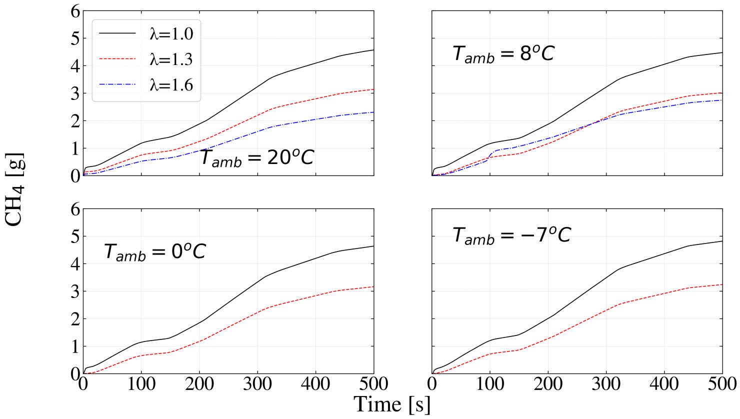

FIGURE 4.40: Comparison of cumulative CH_4 mass for λ=1.0, λ=1.3 and λ=1.6 for transient cold start at 20^{o}C, 8^{o}C,, for λ=1.0, λ=1.3 at 0^{o}C and -7^{o}C ambient temperatures.

Under stoichiometric operation, CH_4 mass amounts to 5.2 g at 20°C and rises to 5.9 g at –7°C. Raising λ to 1.3 reduces CH_4 to 4.1 g at both 20°C and –7°C. Figure 4.40 shows a pronounced increase in cumulative CH_4 for $\lambda = 1.6$ at 8°C, mainly attributed to reduced combustion efficiency during the first cruise and second idling phase when torque declines.

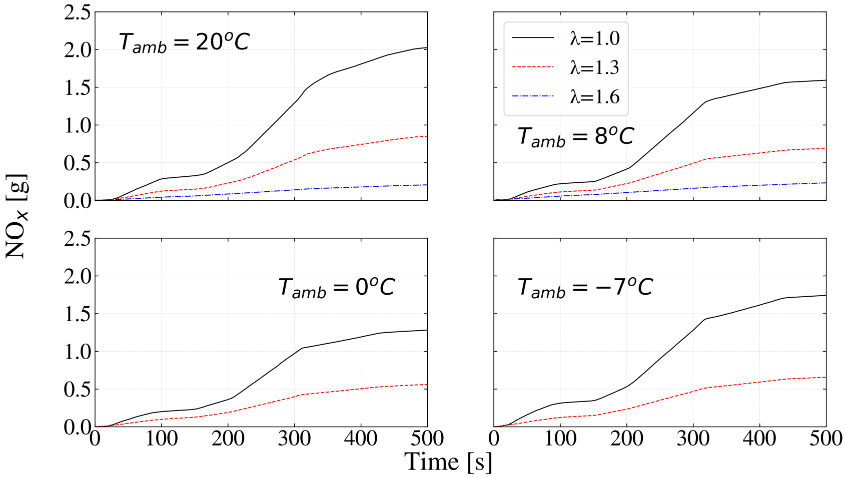

FIGURE 4.41: Comparison of cumulative NO_x mass for λ=1.0, λ=1.3 and λ=1.6 for transient cold start at 20^{o}C, 8^{o}C, for λ=1.0, λ=1.3 at 0^{o}C and -7^{o}C ambient temperatures.

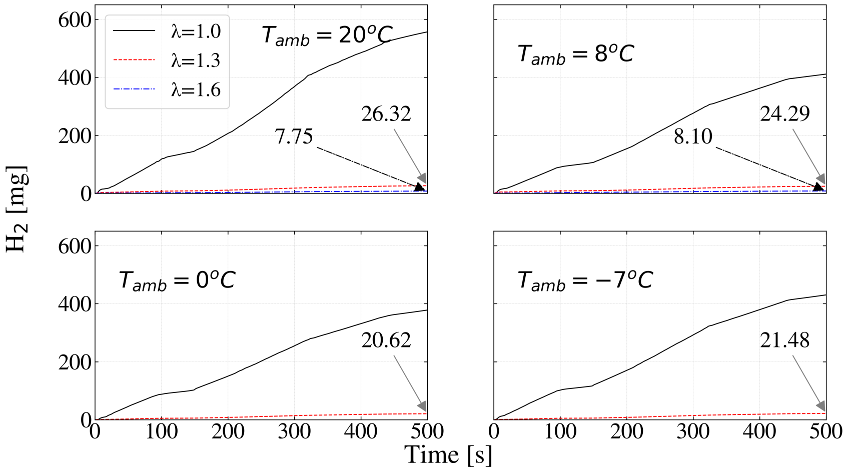

FIGURE 4.42: Comparison of cumulative H_2 mass for λ=1.0, λ=1.3 and λ=1.6 for transient cold start at 20^{o}C, 8^{o}C, for λ=1.0, λ=1.3 at 0^{o}C and -7^{o}C ambient temperatures.

The variation of λ also has a strong influence on NO_x, as illustrated in Figure 4.41. For stoichiometric operation at 20°C, NO_x reaches 2.0 g. At 0°C, it decreases to 1.3 g, while at –7°C it increases again. At $\lambda = 1.3$, NO_x is reduced to 1.0 g at 20°C, with the lowest value of 0.55 g recorded at 0°C. Increasing λ to 1.6 reduces NO_x further, partly as a result of unstable combustion in the initial phases.

The cumulative H_2 emissions are shown in Figure 4.42. It shows a 556 mg peak under stoichiometric operation at 20°C. Increasing λ to 1.3 and 1.6 substantially lowers H_2 to around 50 mg for 20°C and 8°C. Notably, at $\lambda = 1.6$ and 8°C, the H_2 mass remains unaffected by erratic combustion. For stoichiometric conditions and 20°C ambient temperature, CH_2O mass reaches 10 mg and decreases at 8°C, 0°C, and –7°C. Raising λ to 1.3 leads to a marked reduction of CH_2O below 1 mg at 20°C. A similar reduction is observed at 8°C, 0°C, and –7°C. However, at $\lambda = 1.6$ and 8°C, CH_2O emissions rise again owing to poor combustion efficiency, in a manner similar to CH_4. The increase is most evident during the second idling phase at 100 seconds of the cold start.

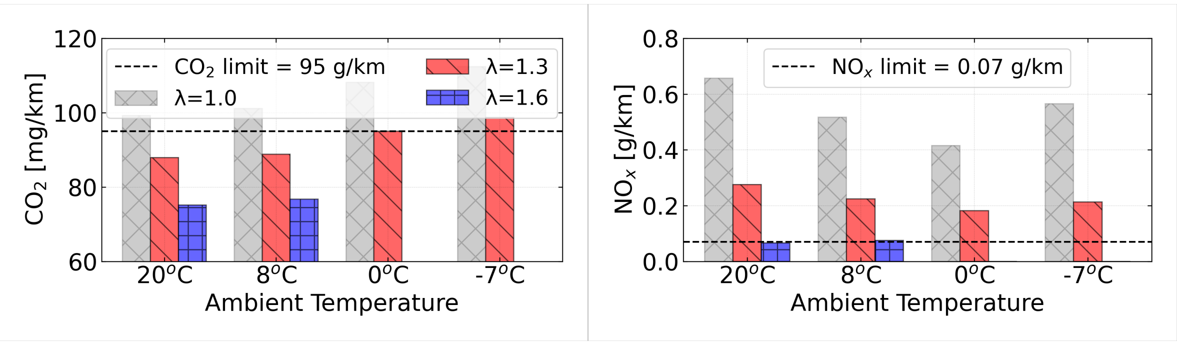

FIGURE 4.43: Comparison of in CO_2 mass per kilometre for λ=1.0, 1.3 and 1.6 for transient cold start at 20^{o}C, 8^{o}C, 0^{o}C and -7^{o}C ambient temperatures. The dashed line shows the Euro 6 emission target for CO_2.

The predicted CO_2 emissions gram per kilometre for the different relative air–fuel ratios are compared with the Euro 6 limit of 95 g/km in left side of the Figure 4.43. Increasing λ to 1.3 reduces CO_2 output by 10–14 g/km, such that emissions fall below the Euro 6 threshold at 20°C, 8°C, and 0°C. A further increase to $\lambda = 1.6$ lowers CO_2 even more compared with $\lambda = 1.3$, predicting values of 75 g/km at 20°C. However, under 8°C conditions, the required torque cannot be achieved, and therefore these results are not representative.

The corresponding NO_x emissions gram per kilometre is shown in B of Figure 4.43. At $\lambda = 1.3$, reductions of 0.24–0.38 g/km are obtained, with the lowest value of 0.18 g/km occurring at 0°C, since reduced ambient temperature lowers combustion temperature. Raising λ to 1.6 provides an additional decrease, allowing the Euro 6 limit of 0.07 g/km to be met at 20°C. Nonetheless, for colder conditions, the necessary torque is not achieved, so the predicted NO_x values cannot be considered reliable.

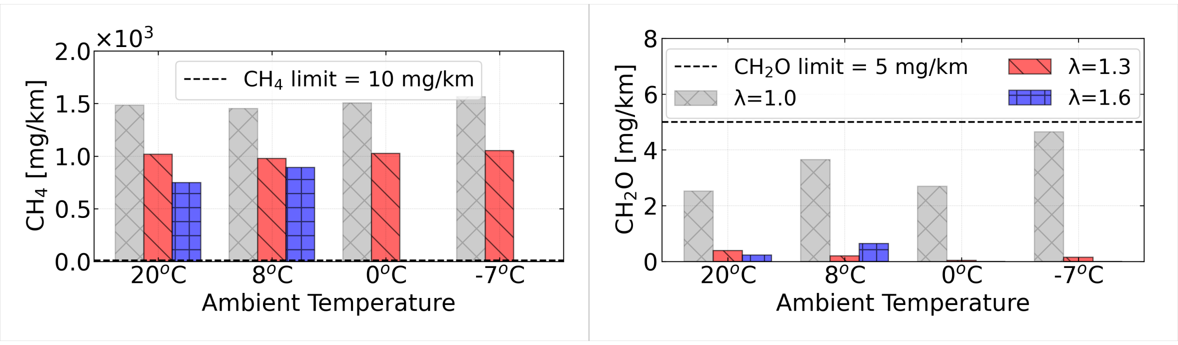

FIGURE 4.44: Comparison of CH_4 mass per kilometre for λ=1.0, 1.3 and 1.6 for transient cold start at 20°C, 8°C, 0°C and -7°C ambient temperatures. The dashed line shows the Euro 6 emission target for CH_4.

The predicted CH_4 rate milligram per kilometre is shown in left of the Figure 4.44 indicate a decrease of 450–550 mg/km when operating with $\lambda = 1.3$. The minimum CH_4 output of 990 mg/km is observed at 8°C. With $\lambda = 1.6$, emissions are further reduced to 780 mg/km at 20°C. However, erratic engine operation at 8°C leads to reduced combustion efficiency, resulting in higher unburned CH_4 release.

The CH_2O emissions rate milligram per kilometre is shown in right of the Figure 4.44, reach their highest levels for all ambient temperatures under stoichiometric conditions. Increasing λ to 1.3 significantly lowers CH_2O, bringing it below the Euro 6 limit. At $\lambda = 1.6$, CH_2O is further reduced at 20°C. In contrast, at 8°C an increase is observed due to reduced combustion efficiency, resembling the trend seen for CH_4. This effect is most pronounced during the second idling phase of the cold start.

4.4.7 Summary

This study examines the WLTP cold-start behaviour of a CNG engine under varying ambient temperatures, fuel compositions, and air-fuel ratios. To this end, engine performance and exhaust emissions, including CO_2, CO, NO_x, CH_4, CH_2O, and H_2, are assessed during the WLTP cold-start cycle for different ambient temperatures:20°C, 8°C, 0°C, and-7°C. The WLTP cold-start cycle considered in this work lasts 8.33 minutes and has been simplified for CNG engine test bench implementation. The simulation with the tabulated chemistry model achieves a runtime of 8.00 minutes, fulfilling real-time requirements. The model's outcomes highlight the influence of ambient temperature, gas composition, and air-fuel ratio on engine-out emissions.

- During the initial 100 seconds, fuel enrichment combined with low cylinder wall temperatures lowers combustion efficiency, leading to significant increases in CO and CH_4 levels.

- Reducing ambient temperature from 20°C to –7°C raises CO_2 and CH_4 mass at the end of cold start phase. Increased friction losses at low temperatures result in higher fuel consumption, thereby elevating CO_2 output, while flame quenching on cold cylinder walls contributes to additional CH_4 release. Conversely, CO and NO_x emissions decline at 8°C and 0°C due to reduced combustion temperatures.

- H-gas, having the highest C:H ratio, produces the greatest CO_2 mass by the end of the driving cycle. Natural gas blended with 10% H_2 offers the largest reduction in CO_2 output, achieving the Euro 6 limit of 95 g/km at 20°C.

- L-gas, with the lowest Wobbe index, results in the smallest NO_x mass because of its lower combustion temperatures. However, enriching the gas with 10% H_2 increases NO_x, as higher combustion temperatures are induced.

- Operating with $\lambda = 1.3$ markedly lowers CO, NO_x, CH_4, and CH_2O across all tested ambient conditions (20°C, 8°C, 0°C, and –7°C), while maintaining stable engine operation even at low temperatures.

- The Euro 6 CO_2 target of 95 g/km is attainable at $\lambda = 1.3$ for ambient conditions of 20°C, 8°C, and 0°C. In addition, NO_x, CH_4, and CH_2O emissions are substantially reduced. Employing an optimised after-treatment system tailored for lean operation could further enhance the efficiency of the overall system.

- Increasing λ to 1.6 causes unstable operation, particularly at 8°C, 0°C, and –7°C. This instability manifests as torque drops during the early cruise phase and the second idling phase. Consequently, CH_4 and CH_2O rise considerably by the end of the cold start. Therefore, the λ-operation at 1.6 does not appear advantageous for the investigated CNG engine.

4.5 Simulation of off-road CNG engine under NRTC

This section applies and assesses the developed simulation toolchain by simulating the SI engine operated during cold start conditions under the NRTC driving cycle in cold-start conditions at ambient temperatures of 10^{O}C and 25^{O}C. for agricultural tractor car applications using CNG as fuel. The objective is to evaluate the model's ability to reproduce transient variations in combustion, performance, and emissions during the critical cold-start phase, which significantly influences overall cycle emissions and fuel consumption in regulatory testing. For these simulations, the SRM incorporates turbulence modelling using the k–ϵ formulation described in the earlier section. Model predictions are validated against experimental transient data. The experimental reference data and simulation data used in this study were obtained from the published journal article [26].

4.5.1 Engine specifications

The experiments were conducted on a medium-duty prototype gas engine developed from the Deutz AG TCD four-cylinder, 3.6L04 diesel engine [99, 100]. Details of the engine specifications are shown in Table 4.12. For the natural gas operation, a gas dosing unit with a custom developed gas mixer was installed in the air pathway of the engine.

TABLE 4.12: Specification of engine parameters of SI engine.

Parameter	**Unit**	**Value**
Bore	mm	98
Stroke	mm	120
Rod Length	mm	137.0
Compression Ratio	–	11:1

4.5.2 Reference experimental data

The reference engine was operated during cold start conditions under the NRTC driving cycle. Figure 4.45 defines operating points used for the model defines operating points used for model training at steady-state conditions, along with a span of points defining the conditions during the NRTC cycle. Figures 4.46-4.47 shows the reference speed and torque profiles and relative air-fuel ratio during the NRTC cycle.

4.5.3 Surrogate fuel and tabulated chemistry

The natural gas composition of the reference and the surrogate fuel is outlined in Table 4.13. The properties of the surrogate model closely match the properties of the real fuel. The model

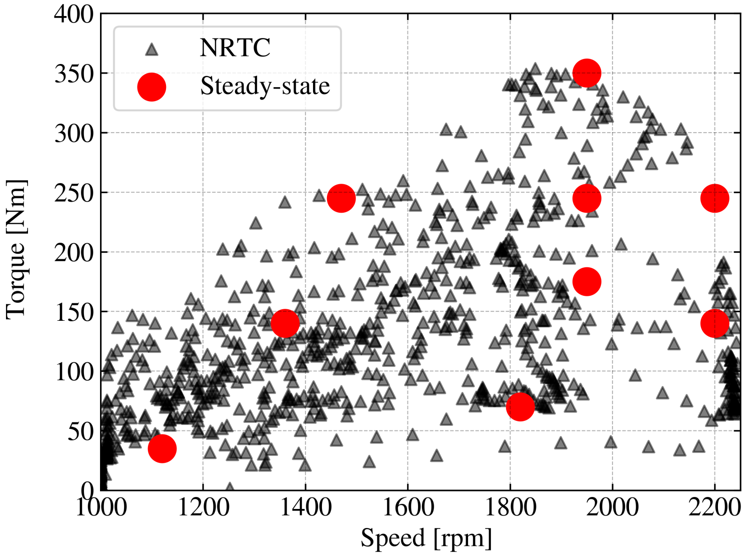

FIGURE 4.45: Steady-state OPs for model training and NRTC OPs.

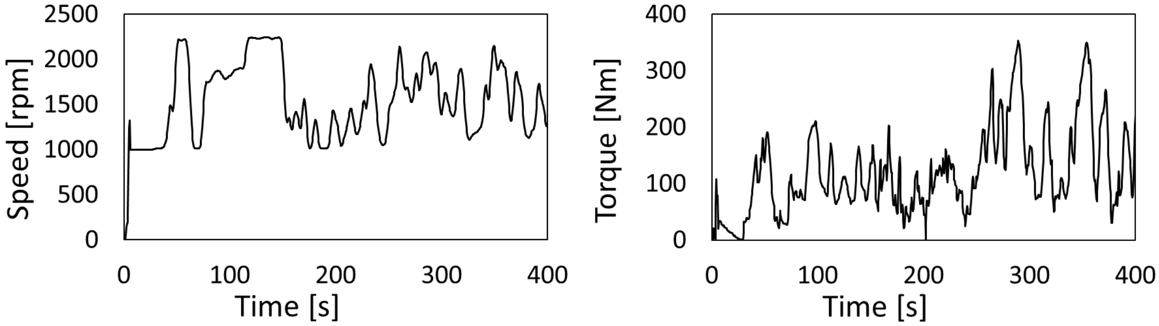

FIGURE 4.46: Reference speed and torque profiles of the NRTC cycle for cold-start phase analysis.

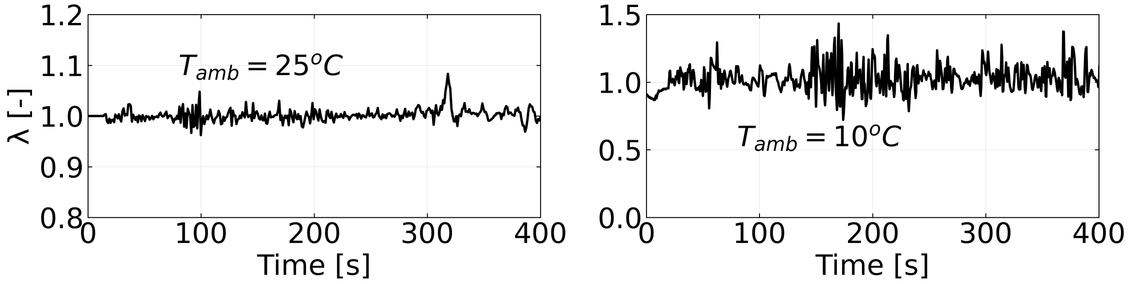

FIGURE 4.47: Relative air-fuel ratio during the NRTC cycle for 25^{o}C and 10^{o}C.

is used in the form of CPV, which was derived from the reaction mechanism from [94]. The model includes an improved nitrogen-hydrocarbon chemistry and is validated for ignition delay time, laminar flame speed and speciation. The reaction mechanism consists of 172 species and 2697 reactions. More information regarding CPV generation is found in a source article [26]

TABLE 4.13: Natural gas composition of the reference and surrogate fuel.

Component	Experiment (%)	Surrogate (%)
CH_4	93.7	93.7
C_2H_6	3.6	3.6
N_2	0.98	0.98
CO_2	0.97	0.97
H_2	0.19	0.19
n-C_4H_{10}	0.16	0.16
AFR_{st}	16.58	16.74
ρ (kg/m^3)	0.71	0.71
LHV (MJ/kg)	48.44	48.94
W_s (MJ/m^3)	47.37	46.72

4.5.4 SRM configuration and training operating points

The SRM is set up with 200 particles. The steady-state model training uses 250 stochastic cycles to account for the cyclic variation during actual engine operation. The cyclic variation model of [14] is used in this work. The model implies a Gaussian distribution for the spark timing (θ spark) and the turbulence frequency (u′). The standard deviation for θ spark is set to 2.28 [CAD] and 0.0035 for u′ [m/s]. Woschni heat transfer model [74] is applied with C_1=2.28 and C_2=0.0035, and piston surface area multiplier set to 1.5. The crevice volume is set to 4% of the cylinder clearance volume, accounting for trapped unburned mass during the compression and combustion phases and release during the expansion stroke. The k-ϵ turbulence model parameters are outlined in Table 4.14. The scalar mixing time factor C_Φ is set to 1.

The turbulent flame propagation model and early flame propagation model parameters b_1 and K are set as 2.6 and 5.0, respectively, which will be the same for all steady state and transient operating conditions. The model parameter ηc of the early flame propagation model is adjusted for different operating conditions.

The steady-state operating points are outlined in Table 4.15. The table additionally includes the standard deviation of spark timing (σ_{ST}) and the correction parameter (η_c) of the

TABLE 4.14: k-ε turbulence model parameters.

Parameter	Value
C_μ	3.5
$C_{\varepsilon,2}$	2.0
$C_{\varepsilon,1}$	1.0
C_ε	0.09

early flame kernel model which were adjusted to match the in-cylinder pressure of the experiments. The standard deviation of the spark timing is increasing for higher torque. The comparison of steady-state points with driving cycle torque is shown in Figure 4.45.

TABLE 4.15: Steady-state operating point model training.

ID	Speed [rpm]	Torque [Nm[	σ_{ST} [°CA]	η_C [mm]
OP1	1950	350	1.1	16.5
OP2	1950	245	1.1	16.0
OP3	1950	175	2.1	18.0
OP4	2200	245	1.1	16.0
OP5	2200	140	2.1	18.0
OP6	1400	70	2.1	18.0
OP7	1400	245	1.1	15.5
OP8	1400	210	1.1	15.5
OP9	1950	35	4.3	21.0

4.5.5 Reference model results at steady state conditions

The simulation results of in-cylinder pressure and RoHR for OP1 are shown in A and B of Figure 4.48. For the rest of the OP's steady-state results, please refer [101]. The profiles of the experiment and simulation are averaged for 250 cycles. Overall, the simulation closely predicts the combustion of the experiments. The comparison of engine-out CO_2 and CO emissions of the steady-state operating points are shown in Figure 4.49. The predicted CO_2 emissions are closely matching with the experiments. The predicted CO emissions shows a lower level of prediction in simulations at all operating points. The predicted NO_x and CH_4 emissions are shown in Figure 4.50 A and B, respectively, which shows the closest match for low-load and mid-load operating points, while for OP6, OP7 and OP8, the simulation NO_x is too low.

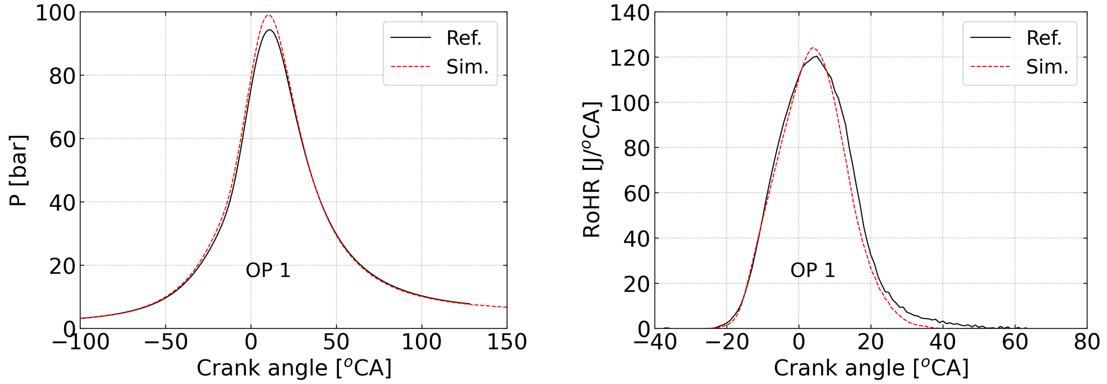

FIGURE 4.48: Comparison of reference and simulated pressure (on left side), and RoHR on right side, for OP1 from Table 4.15.

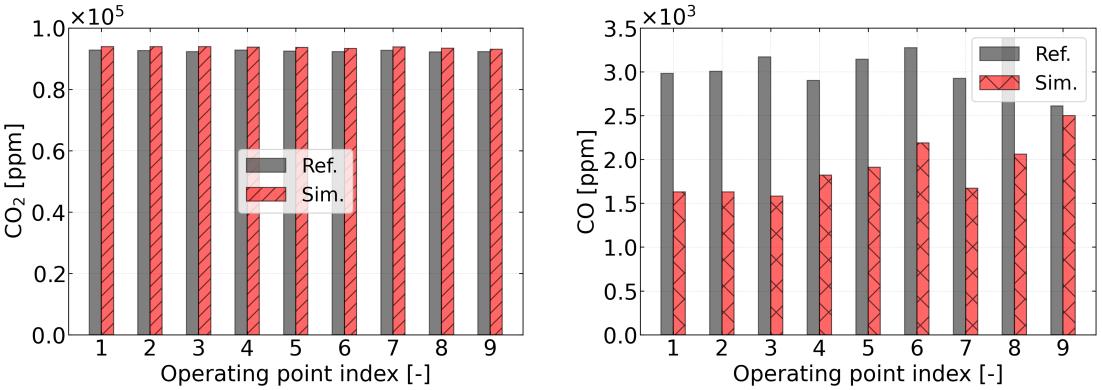

FIGURE 4.49: Comparison of reference and simulation CO_2 (on left side), CO on right side) concentrations for selected steady state OPs.

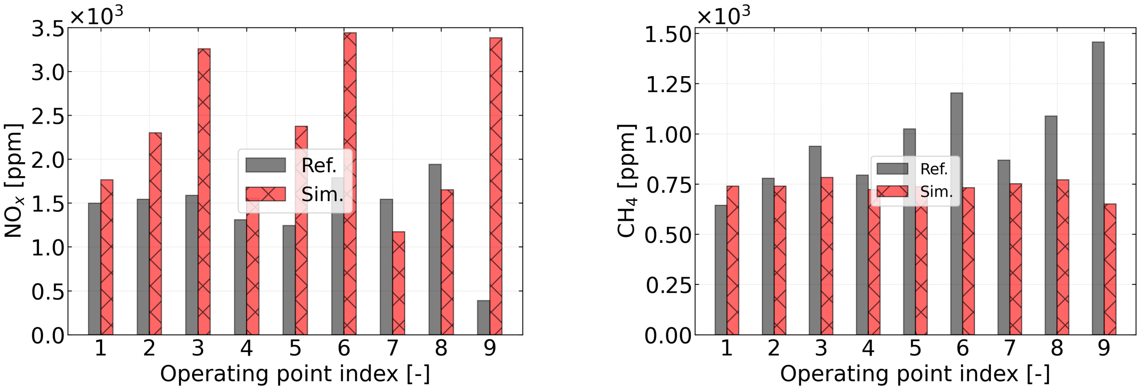

FIGURE 4.50: Comparison of reference and simulation NO_x (on left side), CH_4 (on right side), for selected steady state OPs.

4.5.6 Transient engine simulations

The simulation toolchain is validated for transient cold start experiments at 25^{o}C, and 10^{o}C ambient temperature. The cylinder wall temperature of the engine model changes depending on the load of the engine and the oil temperature, as shown in Figure 4.51. At the beginning, the wall temperature is equal to the ambient temperature. During the first acceleration and cruise phase, the engine oil heats up and the wall temperature increases. As the ambient temperature decreases, the wall temperature decreases, and the lowest wall temperature is predicted for 10^{o}C ambient temperature. Relative air-fuel ratio, it is found that the simulated values from the transient simulations, which are shown in Figure 4.52, accurately match the experiments.

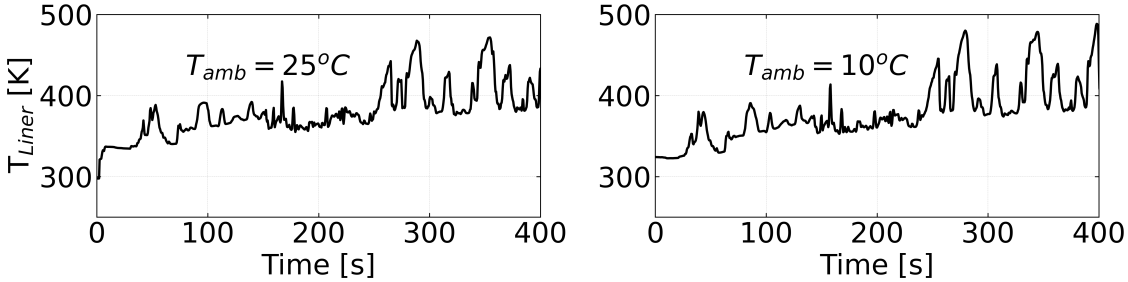

FIGURE 4.51: Cylinder liner temperatures for 25^{o}C, and 10^{o}C ambient temperatures.

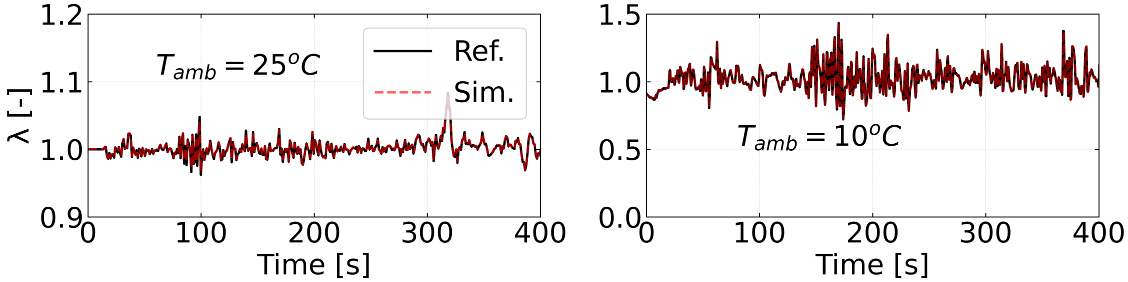

FIGURE 4.52: Comparison of experiment and simulation relative air-fuel ratio for transient cold start at 25^{o}C, 10^{o}C ambient temperatures.

The predicted fuel mass flow is shown in Figure 4.53. For the 25^{o}C simulated fuel mass flow matches with experimental fuel mass flow. For the 10^{o}C ambient temperature simulation fuel mass flow is over predicted. The simulated indicated mean effective torque is shown in Figure 4.54 compared against break torque from experiment. The simulated indicative torque is higher compared to break torque.

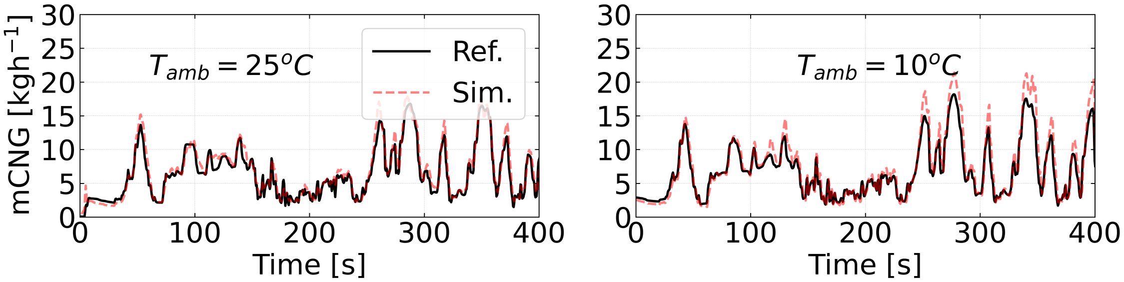

FIGURE 4.53: Comparison of experiment and simulation natural gas mass flow at 25^{o}C, 10^{o}C ambient temperatures.

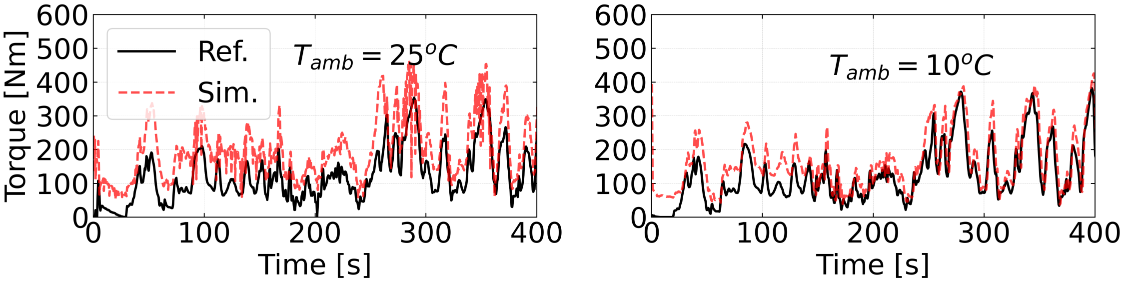

FIGURE 4.54: Reference and experimental torque at 25^{o}C, 10^{o}C ambient temperatures.

The predicted CO_2 is shown in Figure 4.55. At ambient temperatures 25^{o}C and 10^{o}C it is under-predicted. As the ambient temperature decreases, CO_2 increases due to more fuel being injected to overcome frictional losses due to cold-engine oil. The predicted NO_x (Figure 4.57) is overall higher than the experiment for 25^{o}C. For the 10^{o}C ambient temperature, the predicted NO_x for the first 50s, from 75s to 100s, 250s to 280s of the driving cycle is in line with the experiment. For the remaining part of the driving cycle, $NO_x$is lower than in the experiment. Overall the trend of NO_x prediction by the engine model for 10^{o}C is lower than the experiment because of the lower cylinder temperatures. The overall CO (Figure 4.56) prediction for ambient temperature of 25^{o}C is under-predicted by the engine model. For ambient temperature 10^{o}C, CO is oscillating and predicted with frequent peaks due to irregular engine operation. CH_4 (Figure 4.58 for both ambient temperatures 25^{o}C, 10^{o}C is not predicted well. Possibly a stronger flame quenching effect during these phases causes increased unburned CH_4 emissions, which is not predicted by the engine model. As the engine model does not include of a flame-wall quenching model, it is unable to simulate this effect. The simulations also reveal higher unburned CH_4 emissions during the whole driving cycle at 10^{o}C ambient temperature, which may be a result of flame quenching on the cylinder walls.

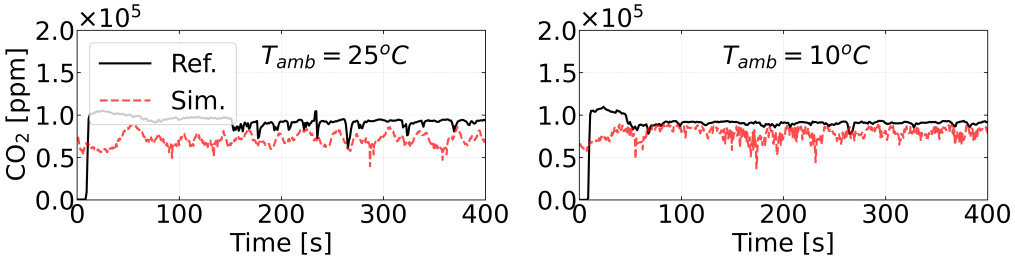

FIGURE 4.55: Comparison of experiment and simulation CO_2 for transient cold start at 25^{o}C, 10^{o}C ambient temperatures.

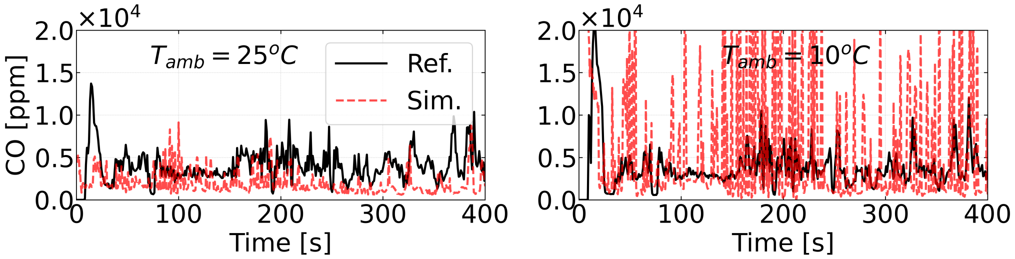

FIGURE 4.56: Comparison of experiment and simulation CO for transient cold start at 25^{o}C, 10^{o}C ambient temperatures.

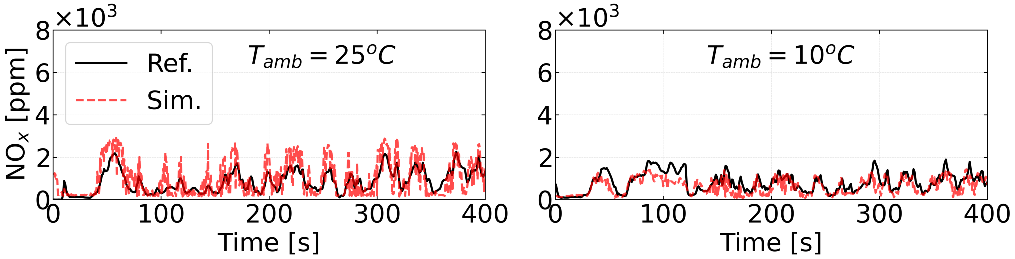

FIGURE 4.57: Comparison of experiment and simulation NO_x for transient cold start at 25^{o}C, 10^{o}C ambient temperatures.

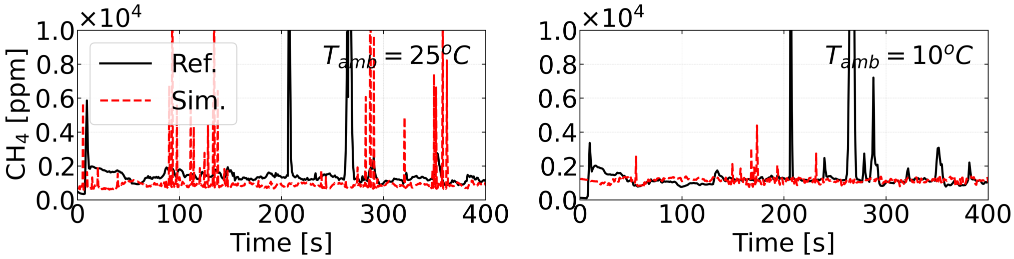

FIGURE 4.58: Comparison of experiment and simulation CH_4 for transient cold start at 25^{o}C, 10^{o}C ambient temperatures.

Cumulative emissions after the driving cycle duration 7min, the total emissions for CO_2, NO_x are shown in Figure 4.59. For CO and CH_4 masses are shown in Figure 4.60. Increase in ambient temperature from 10^{o}C to 25^{o}C resulted in a decrease in total CO_2 produced. Predicted cumulative NO_x is increased as the ambient temperature increases. Cumulative predicted CO is decreased as the ambient temperature decreases. Cumulative predicted CH_4 is decreased with increase in ambient temperature from 10^{o}C to 25^{o}C, as the temperature increases consequently increased fuel consumption, the fuel remaining in exhaust emissions decreases.

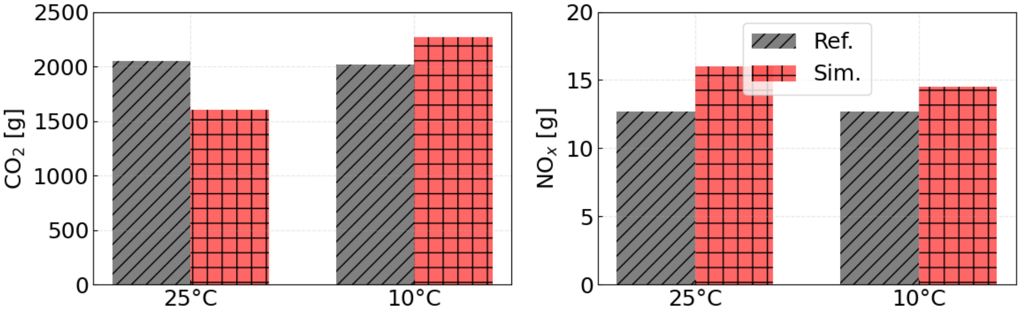

FIGURE 4.59: Comparison of experiment and simulation cumulative CO_2 and CO for transient cold start at 25^{o}C, 10^{o}C ambient temperatures.

4.5.7 Summary

This study analyses the NRTC cold start behaviour of a CNG-powered heavy-duty agricultural engine under ambient conditions of 25^{o}C and 10^{o}C. The assessment focuses on engine performance and exhaust emissions including CO_2, CO, NO_x, and CH_4. Simulations are executed using the simulation toolchain developed in this work. Simulations refer to the simplified NRTC cold start cycle tailored for the CNG test bed that spans 400 seconds.

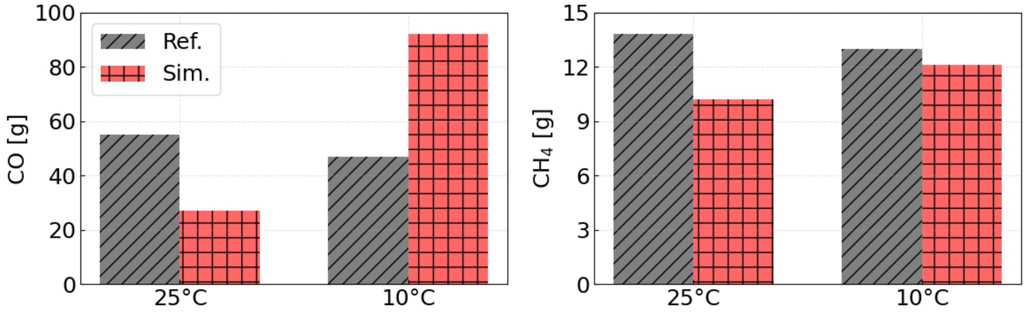

FIGURE 4.60: Comparison of experiment and simulation cumulative NO_x and CH_4 for transient cold start at 25^oC, 10^oC ambient temperatures.

- A reduction in ambient temperature from 25^oC to 10^oC leads to increased frictional losses and elevated fuel consumption. Due to lower combustion temperatures, CO and CH_4 emissions show a decreasing trend at $25^oC$and 10^oC, respectively.
- CH_4 emissions exhibit a slight rise with decreasing ambient temperature. However, the simulation does not fully reproduce the experimental trend. Integrating flame-wall quenching in the model could enhance the performance.
- Predicted NO_x emissions exceed experimental values overall, but the gap narrows as ambient temperature declines. Lower cylinder temperatures at 10^oC contribute to reduced NO_x.
- The shift from 25^oC to 10^oC results in a modest increase in CO_2 mass, attributed to higher fuel demand caused by cold-induced oil friction losses.

4.6 Co-simulations of ammonia-biodiesel engine and SCR

Reducing pollutant emissions from IC engines requires simultaneous optimisation of in-cylinder combustion and exhaust after-treatment. These subsystems are closely coupled - changes in combustion influence exhaust composition, temperature, and flow rates, which directly impact after-treatment systems. Traditional modelling approaches often treat these domains separately, limiting the ability to evaluate integrated performance and optimise both systems together.

In this work, the developed toolchain was adopted for coupled simulations of engine and aftertreatment systems via the FMI standard [102]. Specifically, the methodology was applied to study the Selective Catalytic Reduction (SCR) catalyst connected to the ammonia-biodiesel fuelled engine. The primary aim is to provide a flexible, modular toolchain capable of transient, physics-and chemistry-based co-simulation of engine and after-treatment systems. The framework is device-agnostic. While a SCR unit is used here as a demonstration case, the same approach can be applied to other systems, such as Diesel Oxidation Catalysts (DOC), Three-Way Catalysts (TWC), or particulate filters. The content of the section is based on the published results [103, 25].

4.6.1 Toolchain architecture

The co-simulation toolchain architecture is schematically illustrated in Figure 4.61 [103, 25]. The after-treatment system is modelled in [63] using a 1D Catalytic Reactor Model (CRM) representing SCR catalyst [104]. The CRM solves mass and heat transport along the catalyst channel, heat conduction through the substrate, and surface reaction kinetics. In this study, the surface chemistry included 23 gas-phase species, 31 surface species, and 118 irreversible reactions. FMI technology allows the SRM and CRM to be compiled into FMUs. The FMUs are connected in MATLAB/Simulink. At each simulation time step, the SRM provides the CRM with exhaust gas pressure, temperature, mass flow rate, and species concentrations such as NO, NO_x, NH_3, CO, CO_2, H_2, H_2O, C_3H_6. The CRM returns back-pressure and outlet composition if required for closed-loop operation. The workflow of using the coupled SRM and CRM follows three steps.

- Independent calibration of SRM and CRM using experimental datasets as reference.
- FMU generation for each model.
- Execution of co-simulation, exchanging synchronised data at a defined time step.

4.6.2 Test case definition

To demonstrate the capability of the developed toolchain, it was applied to a single-cylinder Lifan C186F CI engine modified for dual-fuel operation with ammonia-biodiesel. Both fuels were directly injected into the cylinder - ammonia via a Gasoline Direct Injection (GDI) injector at 100 bar, and biodiesel via a common rail (CR) injector at 1500 bar. The modified cylinder head, with injector placement and angles, is shown in 4.62.

Following the workflow from the previous sub-section, first, the SRM was calibrated using measured in-cylinder pressure traces and exhaust gas composition [105]. For the demonstration, a steady-state operating point at 1500 rpm, 5 bar Indicated Mean Effective Pressure (IMEP), and an Ammonia Energy Share (AES) of 21% was selected. Biodiesel was injected at -17.1^o ATDC and ammonia at -14.9^oATDC. The the surface chemistry mechanism for the SCR model was trained against experimental data from Fe-ZSM-5 SCR catalyst. Subsequently, both SCR and CRM models were converted into FMU framework and applied

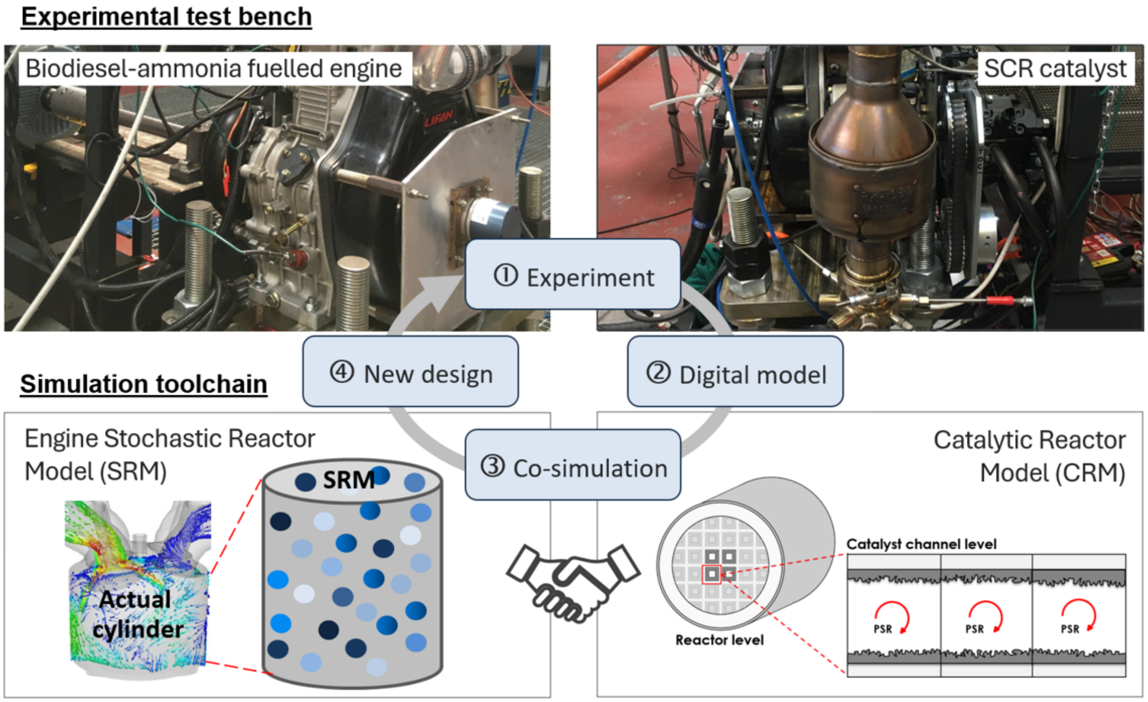

FIGURE 4.61: Virtual representation of the real-world engine-SCR system through the FMI-based coupling of the SRM and CRM [103, 25].

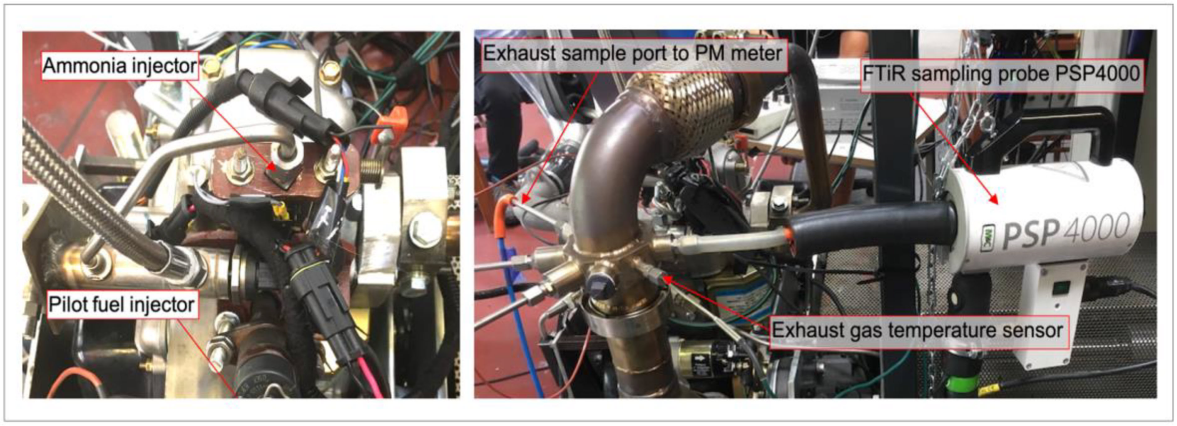

FIGURE 4.62: Modified cylinder head with dual injectors for ammonia and biodiesel [105].

in co-simulations. During the co-simulation model's execution, species concentration in exhaust gas predicted by the SRM were supplied via FMI to the CRM model.

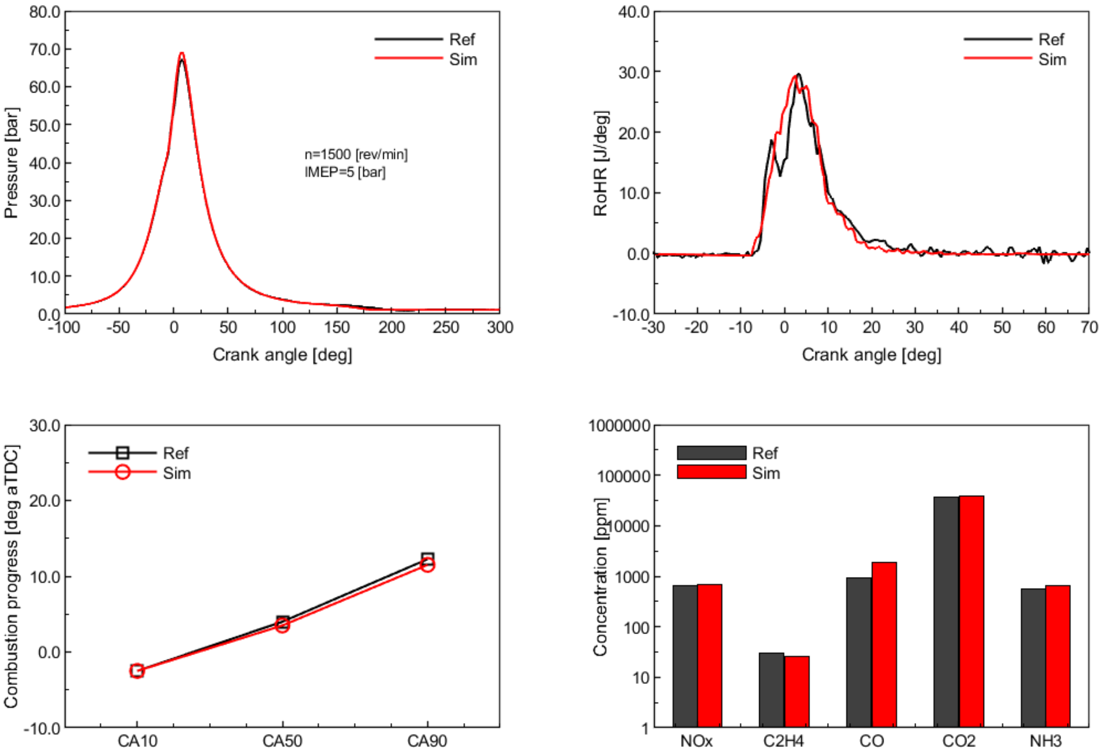

FIGURE 4.63: Example co-simulation result showing SRM-predicted in-cylinder pressure and RoHR histories, and emissions along-with measured data at the demonstration operating point[25].

4.6.3 Exemplary results

The SRM working within the co-simulation toolchain reproduced in-cylinder pressure, RoHR, and combustion phasing with good agreement to experimental data, with only minor deviations in the premixed combustion peak (-5^o to -1^o ATDC). Similarly, good agreement is observed for exhaust emissions (4.63).

The SCR simulation predicted a baseline NO_x conversion of 90.1% and an NH_3 conversion of 51.6% at the given inlet temperature (550 K) and composition. These values were in line with literature trends for Fe-ZSM-5 catalysts [106].

To illustrate the flexibility of the toolchain, a brief sensitivity analysis was performed by varying catalyst length, diameter and catalyst loading. Increasing the catalyst length by 50% increased NO_x conversion to 94.6%, while reducing the length by 30% reduced conversion significantly. Similar trends were observed for the diameter-its increasing by 30% increased NO_x conversion by a few percentage points, while decreasing by 30% reduced conversion significantly. Increasing catalyst loading by 30% improved NO_x conversion by 3.8%, while reducing it by 30% reduced efficiency by 8%.

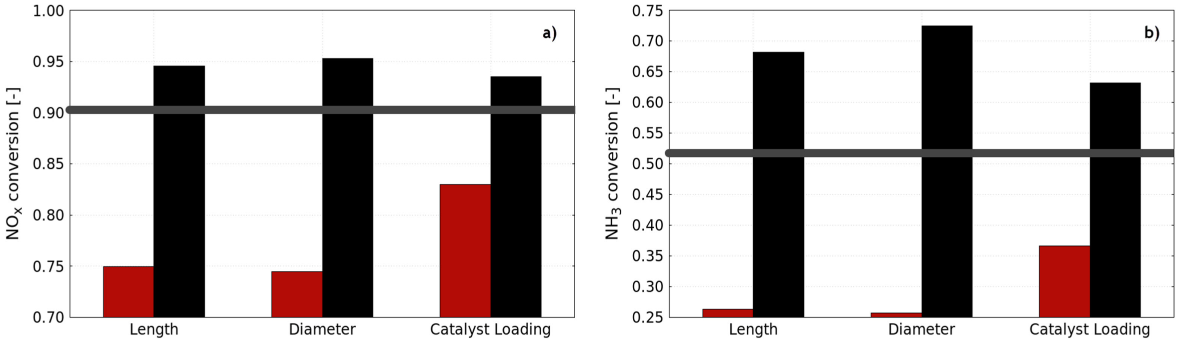

FIGURE 4.64: Effect of catalyst length, diameter, and loading variation on NO$_x$ and NH$_3$ conversion [25].

While NO$_x$ reduction was effective, notable ammonia slip was observed. This was attributed partly to competing reactions involving CO and unburned hydrocarbons in the exhaust. In practice, this could be addressed by integrating an ammonia slip catalyst downstream.

4.6.4 Summary

This work investigated numerically, using the developed toolchain, the impact of the SCR catalyst's properties on ammonia reduction under engine-relevant operating conditions. The framework supported full chemistry on both the engine and catalyst sides. The engine model employing the SRM provided for the SCR input species concentration along with temperature, pressure and mass flow. The obtained results for the SCR show a good NO$_x$ and NH$_3$ conversion efficiency. Sensitivity analysis of length, diameter, and catalyst loading was performed using the virtual catalyst, providing critical insights into their influence on catalytic performance for NO-SCR systems. Increasing the size and amount of active material results in an increase in NO$_x$ conversion. Overall, further investigations are required to understand the high ammonia slip.

The study shows that the developed toolchain can be directly coupled with a detailed after-treatment model via FMI/FMU. The coupling supports full transient chemistry on both engine and catalyst sides without excessive computational cost. The approach is modularthe SCR FMU could be replaced with any other after-treatment FMU without major modifications in the toolchain. This forms a foundation for digital twin applications, real-time simulation, and integrated engine after-treatment optimisation.

4.7 ANN-based simulations of driving cycle

This section presents the simulation results from an ANN meta-model developed to simulate beyond real-time capability. The developed toolchain employing the physical SRM works in real time. However, in some applications or optimisation tasks and workflows, it would be beneficial to run faster than real-time. This is achieved by applying the ANN-based meta-model, which significantly reduces simulation time while maintaining acceptable accuracy. Comparative analyses quantify the trade-off between speed and precision, thereby highlighting the feasibility of deploying an ANN-based fast-running meta-model for real-time control development.

In this study, the ANN-based model was trained using the complete input–output dataset obtained from transient SRM simulations of a CI engine that were presented in section 4.3. The input features were time-resolved engine parameters such as engine speed and load, injection timing, and air-path variables. The outputs captured relevant metrics from combustion and emission species. The model architecture is explained in Section 3.7. All the ANN settings were shown in Table 4.16. The surrogate model was evaluated using the same driving cycle dataset, and the predictions were compared to the results from the original SRM-based modelling.

TABLE 4.16: ANN configuration.

Parameter	**Value**
Input Features	8
Hidden Layers	3
Neurons per Layer	[64, 128, 64]
Activation Function	ReLU
Output Features	5
Optimizer	Adam
Learning Rate	0.001
Loss Function	MSE
Batch Size	32
Epochs	500
Early Stopping	Patience = 20
Dropout Rate	0.2
Normalization	Min-Max Scaling

A comparison of the results obtained from the simulation toolchain and the ANN meta-model is illustrated in the Figure 4.65 for six primary variables over the span of 1800 seconds. SRM-based results and ANN-based results exhibit a strong reproduction of trends over the complete driving cycle. There are minor discrepancies during rapid transition periods, but the ANN model surrogate captures the critical dynamics reliably and rigorously. The ANN-based simulations took less than 10s for the complete driving cycle.

The results in Figure 4.65 show that the maximum in-cylinder pressure and exhaust emissions predicted by the ANN-based model agree with the original data used for training the ANN, and simulated by the physics-based modelling employing the SRM. The difference between the two sets of results, in terms of metrics such as Mean Absolute Error (MAE), Mean Squared Error (MSE),and R^2 score, is less than 5% for all cases. This highlights the ability of the trained ANN model to replicate the behaviour of the SRM with high accuracy. Table 4.17 summarises the quality of the obtained result

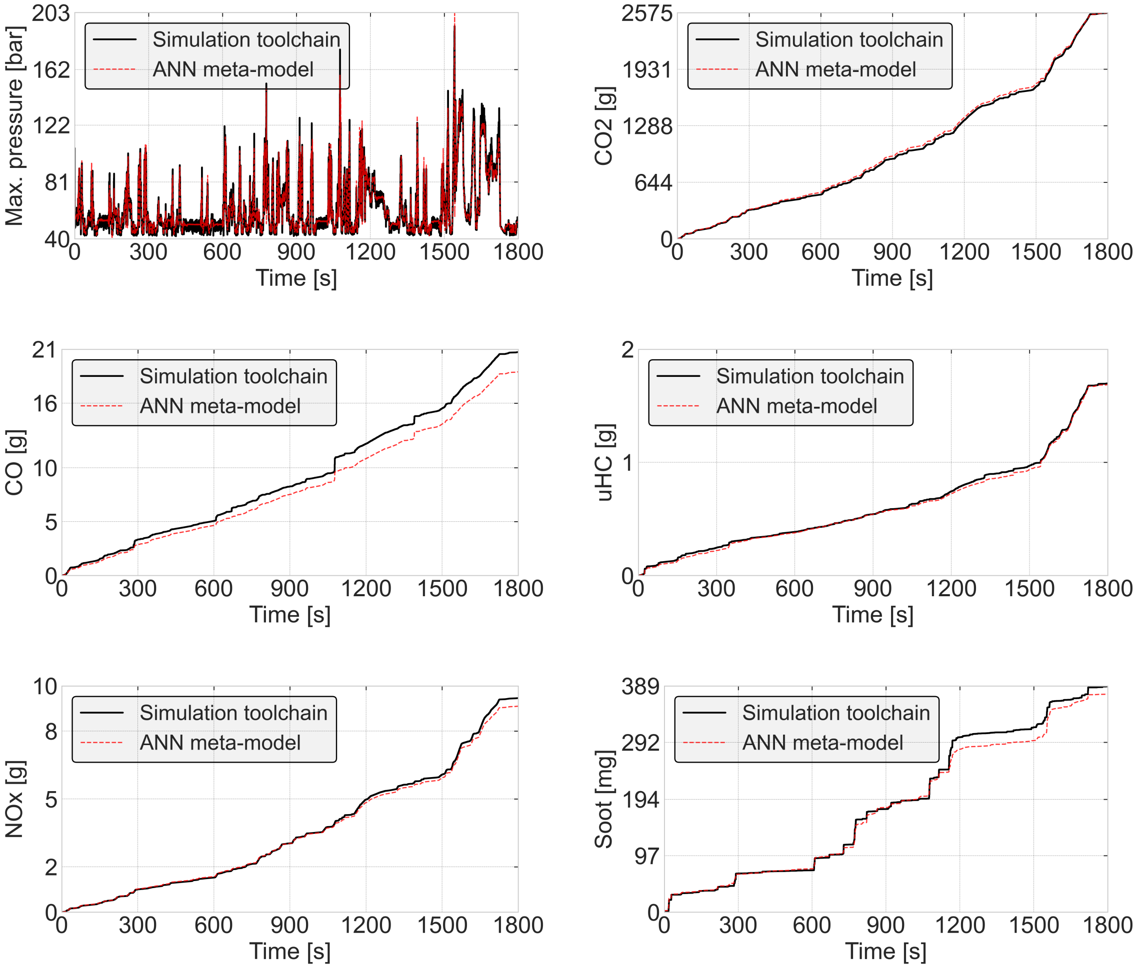

FIGURE 4.65: Comparison between results obtained with the ANN model and the physical model employing the SRM.

TABLE 4.17: Performance metrics of the ANN model in reference to the SRM based results.

Output Variable	**MSE**	**MAE**	**R^2 Score**
Max pressure [bar]	0.0023	0.038	0.984
CO_2 [g]	0.0011	0.025	0.991
CO [g]	0.0009	0.021	0.987
NO_x [g]	0.0015	0.030	0.989
uHC [g]	0.0018	0.033	0.986
Soot [mg]	0.0009	0.021	0.987

4.7.1 Summary

The applied ANN model employed a feed-forward network with three hidden layers and used ReLU activation. It was optimised with the Adam algorithm, with early stopping and dropout regularisation to better generalise. The performance evaluation showed very good agreement between ANN predictions and SRM outputs. Error metrics, when comparing the ANN-based results with the source SRM-based results, were below 5% across the combustion and emissions metrics together. It should be mentioned that in the current workflow, the ANN-based model is trained using the results from the physics-based simulations of the driving cycle that employ the SRM. Hence, the ANN cannot work without the SRM at this stage. The ANN-based model could support simulations targeted at testing other submodels and their control algorithms if they could be simulated faster than real-time, and not requiring changes in the modelling of the in-cylinder processes. In such circumstances, the ANN, once trained, could eliminate the need to rerun the full simulation toolchain, saving computational resources, as for instance simulating the complete WLTP using the ANN takes below 10s. Nevertheless, because of the aforementioned limits, at this stage this modelling approach is considered preliminary and requires further development and improvements.

Chapter 5

Summary

The work introduces a real-time framework for simulating engine performance parameters, exhaust emissions, and fuel effects of SI and CI engines under transient conditions of actual driving cycles, such as WLTP and NRTC. The framework is a unified toolchain that integrates 0D SRM with tabulated chemistry for combustion and pollutant formation into MiL and HiL platforms using the FMI/FMU standard. Such frameworks are of interest to the automotive industry as they help reduce the costs and time involved in costly experimental and prototyping work. The focus has been placed on enabling real-time transient simulations through the seamless integration of the 0D SRM into standardised co-simulation environments, such as MiL/HiL, and cross-platform simulations, features which were not available earlier. This bridges the gap between physical modelling accuracy and practical applicability in engine development workflows for real-time transient simulations.

The existing SRM was adapted to accommodate continuous changes of engine operating parameters such as speed, load, fuel injection strategy, and valve timing, allowing transient simulations. Then, the model was extended to make key engine performance parameters at each cycle, such as maximum cylinder pressure, IMEP, torque, exhaust emissions, and several others, available for the outer-level software to support closed-loop control and system-level analysis. Next, an FMI/FMU wrapper was developed around the SRM solver, compliant with the FMI 2.0 co-simulation standard. It interfaced with the legacy Fortran SRM code, ensuring compatibility with platforms such as MATLAB/Simulink, dSPACE ASM, VEOS, and SCALEXIO. The FMU wrapper includes a dedicated real-time mode to support deterministic execution and synchronised data exchange with external control systems. A port and name resolution mechanism was developed to facilitate FMI-based coupling with third-party engine models. Port definitions are standardised via modelDescription.xml, enabling automatic signal mapping and seamless integration. Subsequently, an integration process was implemented to embed the engine model into MiL and HiL environments. For MiL, standardised signal interfaces were defined to exchange control and plant data. Communication protocols, data types, and execution rates were aligned with control system requirements. For HiL, synchronisation between FMU internal states and external signals was ensured to maintain consistent behaviour under real-time constraints. As a result of all these works, a novel physics-based driving cycle simulator has been developed. The capacity of the tool has been further extended by developing a twin framework that allows the coupling of engine-related processes with the frameworks for exhaust aftertreatment models to work in a co-simulation. Finally, a feedforward ANN-based meta-model of the driving cycle simulator, which acts as a surrogate model, has been developed. The model uses the output performance parameters and emission results from the physical simulator employing the SRM as input and training data. It was designed for ultra-fast execution and embedded within the toolchain.

The developed toolchain was applied in both stand-alone mode and integrated MiL/HiL environments for CI and SI engines under transient driving conditions of WLTP and NRTC to validate its performance and versatility. Application for CI engines dealt with predicting driving-cycle to driving-cycle variability in exhaust emissions, including NO_x, soot, unburned hydrocarbons and CO from a diesel-fuelled engine. The study demonstrated that the number of repeated runs significantly affects the statistical stability of emission predictions. For the WLTP driving cycle, 15 simulations were sufficient to achieve a stable mean for CO_2, CO, and NO_x, while HC required 25 runs and soot required 35 runs. The obtained results lie within accuracy windows reported in the literature, which are 15%, 30%, 40%, 50%, and 60% for CO_2, CO, NO_x, HC, and soot, respectively.

Application for SI engines focused on the analysis of engine behaviour during the cold-start phase of the driving cycle. The results obtained from a CNG engine operated under the WLTP across different ambient temperatures, fuel qualities, and air-fuel ratios revealed strong dependencies between start-up conditions and exhaust composition. Low ambient temperatures increased CO_2 and CH_4 emissions due to higher fuel demand and flame extinction, while reducing NO_x at intermediate cold temperatures due to lower combustion temperatures. H-gas fuels yielded the highest CO_2, whereas 10% H_2 enrichment enabled compliance with Euro 6 CO_2 limits at 20°C. Lean operation at $\lambda = 1.3$ reduced multiple pollutants and maintained stable operation, but $\lambda = 1.6$ caused instability and elevated CH_4 and CH_2O at low ambient temperatures.

Similar investigations were performed for the heavy-duty agricultural CNG engine operated under NRTC cold-start conditions. The lowering of the ambient temperature from 25°C to 10°C increased fuel consumption through higher friction losses, modestly raising CO_2 emissions. Predicted CH_4 showed a slight rise with cooling, though model accuracy could improve with flame-wall quenching effects included. NO_x predictions were higher than experimental data but trended correctly, with colder starts producing less NO_x due to reduced combustion temperatures. These results confirm the model's capability to capture temperature-dependent cold-start trends while highlighting areas for refinement.

The capability of the developed toolchain for co-simulation with aftertreatment systems was verified based on the coupling with an SCR model applied to simulating an ammonia-biodiesel-fuelled engine, resulting in a virtual test bench. Specifically, the work focused on investigating numerically the impact of the properties of SCR catalyst on ammonia reduction under engine-relevant operating conditions. Results show a good NO_x and NH_3 conversion efficiency. Sensitivity analysis of length, diameter, and catalyst loading was performed using the virtual catalyst, providing critical insights into their influence on catalytic performance for NO-SCR systems. Increasing the size and amount of active material results in an increase in NO_x conversion. Overall, further investigations are required to understand the high ammonia slip. In this work, the framework supported full chemistry on both the engine and catalyst sides. The modular design allows substitution of the FMU-based SCR with other aftertreatment models, making the approach suitable for digital twin applications and integrated optimisation of engine after-treatment systems. Furthermore, linking the engine and after-treatment models with a vehicle longitudinal dynamics model would allow studying how the whole powertrain behaves over transient cycles, moving closer to a complete virtual vehicle setup.

The feature of the developed toolchain with regard to applicability to MiL/HiL platforms was verified based on its application to the dSPACE system. Exemplary simulations were performed for SI engines operated under WLTP. The model setup was sourced from the dSPACE library and featured a six-cylinder gasoline engine with port fuel injection. The results obtained for the same engine setup from these two different approaches (MiL/HiL) agree well with each other with regard to simulated maximum pressure and exhaust emissions. Overall, the integration with FMI/FMU standards enabled real-time execution in MiL and HiL environments, where the model maintained synchronisation with external control systems without computational overruns. The results visualised in the configurationDesk from dSPACE validate the integration and operational accuracy of the simulation framework under simulated driving cycle conditions.

An ANN-based meta-model of the driving cycle simulation replicates the reference results with an accuracy window below 5% across combustion-related metrics, such as maximum in-cylinder pressure and IMEP and exhaust emissions, such as CO_2, CO, NO_x, HC, and soot, with simulation time reduced to a fraction of real-time. In the workflow reported in this thesis, the model is trained using the results from the physics-based simulator of the driving cycle that employs the SRM. Hence, the ANN-based meta-model cannot work without the SRM running before. As for now, it could support simulations targeted at testing other sub-models and their control algorithms if they could be simulated faster than real-time, and for an unchanged model of the in-cylinder processes. Hence, at this stage, this modelling approach is considered preliminary and requires further development and improvements.

Through simulation campaigns, this work demonstrates the capability of the simulation toolchain, employing the SRM integrated via FMU/FMI technology into MiL/HiL platforms, in simulating engine performance parameters and fuel effects under transient driving conditions for SI and CI engines. The integration with FMI/FMU standards enables seamless interoperability and real-time execution in MiL and HiL environments. Coupling with after-treatment models, such as SCR catalyst, further extends the framework's capability, which may serve as a virtual test bench. The developed toolchain provides a robust and scalable approach for real-time predictive simulations, making it directly applicable in both research and industrial engine development contexts.

Nomenclature

Abbreviations

ANN — Artificial Neural Network
ASM — Automotive Simulink Models
CA50 — Combustion Centre
CI — Compression Ignition
CNG — Compressed Natural gas
CPV — Combustion Progress Variable
DLL — Dynamic-link library
DOC — Diesel oxidation catalyst
ECU — Electronic control unit
EGR — Exhaust Gas Recirculation
EV — Electric Vehicles
EVO — Exhaust Valve Opening
FMI — Functional Mock-up Interface
FMU — Functional Mock-up Unit
H-Gas — High-caloric Gas
HiL — Hardware-in-the-Loop
IC — Internal Combustion
L-Gas — Low-caloric Gas
LHV — Lower heating value
MDF — Mass density function
MiL — Model-in-the-Loop
MPC — Model predictive control
NRTC — Non-road Transient Cycle
PAH — Polycyclic Aromatic Hydrocarbons
PaSPFR — Partially Stirred Plug Flow Reactor
PDF — Probability Density Dunction
PM — Particulate Matter
RoHR — Rate of Heat Release
SCR — Selective Catalytic Reduction
SDK — Software Development Kit
SI — Spark-Ignition
SRM — Stochastic Reactor Model
VEOS — Virtual ECU and ethernet open system
WLTP — Worldwide harmonised Light vehicles test Procedure

Symbols

Symbol	Meaning	Unit
ε	Dissipation of turbulent kinetic energy	m^2/s^3
ϕ	Equivalence ratio	–
$\phi(t)$	Joint vector of the local scalar variables	–
λ	Lambda (air-fuel ratio indicator)	–
τ_{turb}	Turbulent mixing time	s
τ_{mix}	Scalar mixing time	s
ω_i	Chemistry source/sink term for species i	1/s
ψ	Realization of the random variables	–
C	Reaction progress variable	–
C_r	Source term of reaction progress variable ($\mathrm{d}C/\mathrm{d}t$)	1/s
C_r	Mixing time constant	s
c_p	Specific heat capacity at constant pressure	J/kg·K
E_r	Activation energy of reaction r	J/mol
E_v	Activation energy of reaction v	J/kg
h	Enthalpy	J/kg
h_r	Enthalpy of reaction r	J/kg
$h_{r,\max}$	Max value of minimum heat release state	J/kg
h_g	Heat transfer coefficient	$W/m^2 \cdot K$
H	Heat of combustion	J/kg
k_r	Reaction rate constant of reaction r	1/s
k	Mean kinetic energy	J/kg
k	Chemical equilibrium constant	–
L_k	Lumped species reaction rate	$mol/m^3 \cdot s$
m	Mass	kg
$\dot{m}$	Mass flow rate	kg/s
n_r	Number of reactions in the scheme	–
n_s	Number of chemical species	–
p	Pressure	Pa
R	Universal gas constant	J/mol·K
s_l	Laminar flame speed	m/s
s_t	Turbulent flame speed	m/s
T	Temperature	K
T_a	Ambient temperature	K
T_u	Unburnt state temperature	K
T_b	Burnt state temperature	K

t	Time	s
$\tilde{V}$	Volume	m^3
$\dot{\tilde{V}}$	Volume flow rate	m^3/s
W_i	Molar mass of species i	g/mol
Y_i	Mass fraction of species i	–

List of Publications

This section contains a list of publications resulting from the work carried out during the course of the doctoral study and used in this thesis. The articles and conference contributions are grouped into those associated with the thesis subject and others, not involved directly.

Publications related to thesis

[1] Reddy Babu Siddareddy, Tim Franken, Michał Pasternak, Larisa Leon de Syniawa, et al. Real-time simulation of cng engine and after-treatment system cold start part 1: Transient engine-out emission prediction using a stochastic reactor model. *SAE International Journal of Advances and Current Practices in Mobility*, 5(6):2421–2443, 2023. doi: 10.4271/2023-01-0183. URL `https://doi.org/10.4271/2023-01-0183`.

[2] Reddy Babu Siddareddy, Michał Pasternak, Larisa Leon de Syniawa, Vivien Guenther, Lars Seidel, Fabian Mauss, Grzegorz Przybyła, and Wojciech Adamczyk. Simulations of the scr catalyst in ammonia-biodiesel fuelled ci engine using virtual test bench with detailed chemistry. *Renewable Energy*, 2025. doi: 10.1016/j.renene.2025.123169. URL `https://doi.org/10.1016/j.renene.2025.123169`.

[3] Mario. Picerno, Sung-Yong Lee, Michał Pasternak, Reddy Babu Siddareddy, Tim Franken, Fabian Mauss, and Jacob. Andert. Real-time emission prediction with detailed chemistry under transient conditions for hardware-in-the-loop simulations. *Energies*, 15 (1):261, 2022. doi: 10.3390/en15010261. URL `https://doi.org/10.3390/en15010261`.

[4] Reddy Babu. Siddareddy, Tim. Franken, Michał Pasternak, and Fabian Mauss. Parametric study of a stochastic reactor model for real-time transient driving cycle engine-out emissions prediction. In *Proceedings of the European Combustion Meeting*, Rouen, France, 2023.

[101] Reddy Babu Siddareddy, Tim Franken, Larisa Leon de Syniawa, and Michał others Pasternak. Simulation of cng engine in agriculture vehicles. part 1: Prediction of cold start engine-out emissions using tabulated chemistry and stochastic reactor model. Technical Paper 2023-24-0006, SAE International, 2023. URL `https://doi.org/10.4271/2023-24-0006`.

[6] Reddy Babu Siddareddy, Michał Pasternak, Larisa Leon de Syniawa, Vivien Guenther, Lars Seidel, Fabian Mauss, Grzegorz Przybyła, and Wojciech Adamczyk. Simulations of the scr catalyst in ammonia-biodiesel fuelled ci engine using virtual test bench with detailed chemistry. In *8th International Conference on Contemporary Problems of Thermal Engineering (CPOTE 2024)*, Poland, 2024.

[7] Larisa Leon de Syniawa, Reddy Babu Siddareddy, Johannes Oder, Tim Franken, et al. Real-time simulation of cng engine and after-treatment system cold start. part 2: Tailpipe emissions prediction using a detailed chemistry based moc model. Technical Paper 2023-01-0364, SAE International, 2023. URL `https://doi.org/10.4271/2023-01-0364`.

[8] Larisa Leon de Syniawa, Reddy Babu Siddareddy, Sasha Prehn, Vivien Guenther, et al. Simulation of cng engine in agriculture vehicles. part 2: Coupled engine and exhaust gas aftertreatment simulations using a detailed twc model. Technical Paper 2023-24-0112, SAE International, 2023. URL `https://doi.org/10.4271/2023-24-0112`.

[9] Michał Pasternak, Reddy Babu Siddareddy, Larisa Leon de Syniawa, Vivien Guenther, Michał Picerno, Jacob Andert, Tim Franken, Fabian Mauss, and Wojciech Adamczyk. Plant modelling of engine and aftertreatment systems for x-in-the-loop simulations with detailed chemistry. In *13th CONAT Congress*, Brașov, Romania, 2024. doi: 10.1007/978-3-031-77627-4_14. URL `https://doi.org/10.1007/978-3-031-77627-4_14`.

[10] Reddy Babu Siddareddy, Michał Pasternak, Tim Franken, Fabian Mauss, and Wojciech Adamczyk. Virtual development of ammonia-hydrogen engine digital twin. CYPHER Workshop on "Digital Twins for the Decarbonization of hard-to-abate industries", 2024. (Poster).

Other publications

[1] Michał Pasternak, Grzegorz Przybyła, Reddy Babu Siddareddy, Michał Lewandowski, Karl Bjørgen, Fabian Mauss, Ebrahim Nadimi, Grzegorz Peczkis, Min-min Zhou, and Wojciech Adamczyk. Development of ammonia-biodiesel fueled agricultural tractor: Aspects of retrofitting a compression ignition engine to direct ammonia injection. *Energy*, 2025. doi: 10.1016/j.energy.2025.136255. URL `https://doi.org/10.1016/j.energy.2025.136255`.

[2] Michał Pasternak, Grzegorz Przybyła, Wojciech Adamczyk, Reddy Babu Siddareddy, and Fabian Mauss. Numerical study of combustion in a compression ignition engine with direct ammonia and biodiesel injection for agriculture applications. In *2nd Symposium on Ammonia Energy*, Orléans, France, 2023. (Presentation).

[3] Tim Franken, Reddy Babu Siddareddy, Michał Pasternak, Lars Seidel, and Fabian Mauss. Virtual co-optimization of ammonia-hydrogen blends and medium-duty gas engines for agriculture applications. In *2nd Symposium on Ammonia Energy*, Orléans, France, 2023.

[4] Fabian Mauss, Michał Pasternak, Reddy Babu Siddareddy, and Tim Franken. The ammonia slip – no emission trade off in ci engines. In *3rd Symposium on Ammonia Energy*, Shanghai, China, 2024. (Presentation).

[5] Michał Pasternak, Reddy Babu Siddareddy, Tim Franken, and Fabian Mauss. Prediction of ammonia/hydrogen flame regimes under transient ic engine conditions. In *4th Symposium on Ammonia Energy*, Minneapolis, Minnesota, USA, 2025. (Submitted presentation).

Bibliography

[1] Mika Takahashi. Hydrogen internal combustion engines 2025-2045: Applications, technologies, market status and forecasts, 2024. URL `https://www.idtechex.com/en/research-report/hydrogen-internal-combustion-engines/1030`.

[2] Zongyu Yue and Haifeng Liu. Advanced research on internal combustion engines and engine fuels. *Energies*, 16(16):5940, August 2023. ISSN 1996-1073. doi: 10.3390/en16165940. URL `http://dx.doi.org/10.3390/en16165940`.

[3] Noboru Uchida, Angelo Onorati, Ricardo Novella, Avinash Kumar Agarwal, Amir FN Abdul-Manan, André Casal Kulzer, Silvana Di Iorio, Victor Gordillo, Michael Günthner, Ashutosh Jena, Tommaso Lucchini, Raul Payri, Apostolos Pesyridis, Bianca Maria Vaglieco, and Hardikk Valera. E-fuels in ic engines: A key solution for a future decarbonized transport. *International Journal of Engine Research*, March 2025. ISSN 2041-3149. doi: 10.1177/14680874251325296. URL `http://dx.doi.org/10.1177/14680874251325296`.

[4] Rolf D. Reitz. Ijer editorial: The future of the internal combustion engine. *International Journal of Engine Research*, 21(1):3–10, September 2019. ISSN 2041-3149. doi: 10.1177/1468087419877990. URL `http://dx.doi.org/10.1177/1468087419877990`.

[5] European Union. Worldwide harmonised Light-duty vehicles Test Procedure (WLTP) and Real Driving Emissions (RDE), 2017. URL `https://tinyurl.com/EUDRC`. EUR-Lex.

[6] TransportPolicy.net. International: Nonroad: Nrtc test. `https://www.transportpolicy.net/standard/international-nonroad-nrtc-test/`, n.d. Accessed July 2025.

[7] Stephen B. Pope. Pdf methods for turbulent reactive flows. *Progress in Energy and Combustion Science*, 11(2):119–192, 1985. ISSN 0360-1285. doi: 10.1016/0360-1285(85)90002-4. URL `http://dx.doi.org/10.1016/0360-1285(85)90002-4`.

[8] Michal Pasternak, Fabian Mauss, Cathleen Perlman, and Harry Lehtiniemi. Aspects of 0d and 3d modeling of soot formation for diesel engines. *Combustion Science and Technology*, 186(10–11):1517–1535, September 2014. ISSN 1563-521X. doi: 10.1080/00102202.2014.935213. URL `http://dx.doi.org/10.1080/00102202.2014.935213`.

[9] Andrea Matrisciano, Anders Borg, Cathleen Perlman, Harry Lehtiniemi, Michal Pasternak, and Fabian Mauss. Soot source term tabulation strategy for diesel engine simulations with srm. In *SAE Technical Paper Series*, volume 1 of *ICE2015*. SAE International, September 2015. doi: 10.4271/2015-24-2400. URL `http://dx.doi.org/10.4271/2015-24-2400`.

[10] Tim Franken, Andrea Matrisciano, Rafael Sari, Álvaro Fogué Robles, Javier Monsalve-Serrano, Dario Lopez Pintor, Michal Pasternak, Antonio Garcia, and Fabian Mauss. Modeling of reactivity controlled compression ignition combustion using a stochastic reactor model coupled with detailed chemistry. In *SAE Technical Paper Series*, ICE2021. SAE International, September 2021. doi: 10.4271/2021-24-0014. URL `http://dx.doi.org/10.4271/2021-24-0014`.

[11] Michal Pasternak, Fabian Mauss, Christian Klauer, and Andrea Matrisciano. Diesel engine performance mapping using a parametrized mixing time model. *International Journal of Engine Research*, 19(2):202–213, July 2017. ISSN 2041-3149. doi: 10.1177/1468087417718115. URL `http://dx.doi.org/10.1177/1468087417718115`.

[12] Tim Franken, Arnd Sommerhoff, Werner Willems, Andrea Matrisciano, Harry Lehtiniemi, Anders Borg, Corinna Netzer, and Fabian Mauss. Advanced predictive diesel combustion simulation using turbulence model and stochastic reactor model. In *SAE Technical Paper Series*, ANNUAL. SAE International, March 2017. doi: 10.4271/2017-01-0516. URL `http://dx.doi.org/10.4271/2017-01-0516`.

[13] Michal Pasternak, Fabian Mauss, Gábor Janiga, and Dominique Thévenin. Self-calibrating model for diesel engine simulations. In *SAE Technical Paper Series*, ANNUAL. SAE International, April 2012. doi: 10.4271/2012-01-1072. URL `http://dx.doi.org/10.4271/2012-01-1072`.

[14] Corinna Netzer, Michal Pasternak, Lars Seidel, Frédéric Ravet, and Fabian Mauss. Computationally efficient prediction of cycle-to-cycle variations in spark-ignition engines. *International Journal of Engine Research*, 21(4):649–663, June 2019. ISSN 2041-3149. doi: 10.1177/1468087419856493. URL `http://dx.doi.org/10.1177/1468087419856493`.

[15] Paul D. Walker. Model-based development and calibration of automotive engine control systems. *Control Engineering Practice*, 19(9):962–969, 2011. doi: 10.1016/j.conengprac.2011.05.002.

[16] Tianjun Zheng, Amir Khajepour, Shuaibing Chen, and Bakhtiar Litkouhi. A model-in-the-loop simulation framework for vehicle control system development. *IEEE Transactions on Vehicular Technology*, 67(5):3885–3899, 2018. doi: 10.1109/TVT.2018.2794458.

[17] Werner Damm, Bernhard Josko, Jens Oehlerking, and Thomas Peikenkamp. Hardware-in-the-loop and real-time simulation for automotive applications. *ATZ Worldwide*, 110(9): 28–33, 2008. doi: 10.1007/BF03223447.

[18] dSPACE. Fmi for pc-based simulation, dspace, 2024. URL `https://www.dspace.com/`.

[19] Martin Rindarøy, Håvard Nordahl, Severin Sadjina, Stian Skjong, and Marianne Hagaseth. Adding higher-level semantics to functional mock-up units for easier, faster, and more robust co-simulation connections. *Software and Systems Modeling*, 24(2):471–487, January 2025. ISSN 1619-1374. doi: 10.1007/s10270-024-01244-3. URL `http://dx.doi.org/10.1007/s10270-024-01244-3`.

[20] Modelica Association. *Functional Mock-up Interface Specification, Version 3.0.1*, 2023. URL `https://fmi-standard.org/docs/3.0.1/`. Accessed: 2025-09-13.

[21] OpenModelica. *Functional Mock-up Interface (FMI)*, 2025. URL `https://openmodelica.org/doc/OpenModelicaUsersGuide/v1.25.0/fmitlm.html`. Accessed: 2025-09-13.

[22] Martin Krammer, Helmut Martin, Zoran Radmilovic, Simon Erker, and Michael Karner. Standard compliant co-simulation models for verification of automotive embedded systems. In *2015 Forum on Specification and Design Languages (FDL)*, pages 1–8, 2015.

[23] Johannes Ultsch, Julian Ruggaber, Andreas Pfeiffer, Christina Schreppel, Jakub Tobolář, Jonathan Brembeck, and Daniel Baumgartner. Advanced controller development based on efmi with applications to automotive vertical dynamics control. *Actuators*, 10(11):301, November 2021. ISSN 2076-0825. doi: 10.3390/act10110301. URL `http://dx.doi.org/10.3390/act10110301`.

[24] Reddy Babu Siddareddy, Tim Franken, Michal Pasternak, Larisa Leon de Syniawa, Johannes Oder, Hermann Rottengruber, and Fabian Mauss. Real-time simulation of cng engine and after-treatment system cold start part 1: Transient engine-out emission prediction using a stochastic reactor model. *SAE International Journal of Advances and Current Practices in Mobility*, 5(6):2421–2443, April 2023. ISSN 2641-9645. doi: 10.4271/2023-01-0183. URL `http://dx.doi.org/10.4271/2023-01-0183`.

[25] Reddy Babu Siddareddy, Michał Pasternak, Larisa León de Syniawa, Vivien Guenther, Lars Seidel, Fabian Mauss, Grzegorz Przybyła, and Wojciech Adamczyk. Simulations of the scr catalyst in ammonia-biodiesel fuelled ci engine using virtual test bench with detailed chemistry. *Renewable Energy*, 251:123169, October 2025. ISSN 0960-1481. doi: 10.1016/j.renene.2025.123169. URL `http://dx.doi.org/10.1016/j.renene.2025.123169`.

[26] Reddy Babu Siddareddy, Tim Franken, Larisa Leon de Syniawa, Michal Pasternak, Sascha Prehn, Bert Buchholz, and Fabian Mauss. Simulation of cng engine in agriculture vehicles. part 1: Prediction of cold start engine-out emissions using tabulated chemistry and stochastic reactor model. In *SAE Technical Paper Series*, ICE2023. SAE International, August 2023. doi: 10.4271/2023-24-0006. URL http://dx.doi.org/10.4271/2023-24-0006.

[27] Mario Picerno, Sung-Yong Lee, Michal Pasternak, Reddy Siddareddy, Tim Franken, Fabian Mauss, and Jakob Andert. Real-time emission prediction with detailed chemistry under transient conditions for hardware-in-the-loop simulations. *Energies*, 15:261, 12 2022. doi: 10.3390/en15010261. URL https://doi.org/10.3390/en15010261.

[28] UNECE. Worldwide harmonized transient cycle (whtc). https://unece.org/worldwide-harmonized-transient-cycle, 2016. Accessed: 2024-11-01.

[29] Federico Borghi, Marek Pasternak, and Markus Kraft. High-fidelity transient simulation of internal combustion engines for control-oriented applications. In *Proceedings of the ASME Internal Combustion Engine Division*, 2020.

[30] Lino Guzzella and Christopher H. Onder. *Introduction to Modeling and Control of Internal Combustion Engine Systems*. Springer Berlin Heidelberg, 2010. ISBN 9783642107757. doi: 10.1007/978-3-642-10775-7. URL http://dx.doi.org/10.1007/978-3-642-10775-7.

[31] Lars Eriksson and Lars Nielsen. *Modeling and Control of Engines and Drivelines*. Wiley, February 2014. ISBN 9781118536186. doi: 10.1002/9781118536186. URL http://dx.doi.org/10.1002/9781118536186.

[32] Johan Wahlström and Lars Eriksson. Modelling diesel engines with a variable-geometry turbocharger and exhaust gas recirculation by optimization of model parameters for capturing non-linear system dynamics. *Proceedings of the Institution of Mechanical Engineers, Part D: Journal of Automobile Engineering*, 225(7):960–986, May 2011. ISSN 2041-2991. doi: 10.1177/0954407011398177. URL http://dx.doi.org/10.1177/0954407011398177.

[33] Andrea Matrisciano, Tim Franken, Laura Catalina Gonzales Mestre, Anders Borg, and Fabian Mauss. Development of a efficient tabulated chemistry solver for internal combustion engine optimization using stochastic reactor models. *Applied Sciences*, 10(24):8979, December 2020. ISSN 2076-3417. doi: 10.3390/app10248979. URL http://dx.doi.org/10.3390/app10248979.

[34] Tim Franken, Corinna Netzer, Fabian Mauss, Michal Pasternak, Lars Seidel, Anders Borg, Harry Lehtiniemi, Andrea Matrisciano, and Andre Casal Kulzer. Multi-objective optimization of water injection in spark-ignition engines using the stochastic reactor

model with tabulated chemistry. *International Journal of Engine Research*, 20(10):1089–1100, June 2019. ISSN 2041-3149. doi: 10.1177/1468087419857602. URL http://dx.doi.org/10.1177/1468087419857602.

[35] Angelo Onorati and Gianluca Montenegro. 1D and multi-d modeling techniques for IC engine simulation, April 2020.

[36] Masoud Aliramezani, Charles Robert Koch, and Mahdi Shahbakhti. Modeling, diagnostics, optimization, and control of internal combustion engines via modern machine learning techniques: A review and future directions. *Progress in Energy and Combustion Science*, 10 2021. doi: 10.1016/j.pecs.2021.100967. URL https://www.researchgate.net/publication/355483456.

[37] Michal Pasternak, Fabian Mauss, Marc Sens, Michael Riess, Andreas Benz, and Karl Georg Stapf. Gasoline engine simulations using zero-dimensional spark ignition stochastic reactor model and three-dimensional computational fluid dynamics engine model. *International Journal of Engine Research*, 17(1):76–85, December 2015. ISSN 2041-3149. doi: 10.1177/1468087415599859. URL http://dx.doi.org/10.1177/1468087415599859.

[38] Angelo Onorati and Gianluca Montenegro. *1D and multi-D modeling techniques for IC engine simulation*. SAE International, Warrendale, April 2020.

[39] Thomas Gal, Robin Schmelcher, Antonino Vacca, Francesco Cupo, Marco Chiodi, and André Casal Kulzer. Modeling of hydrogen combustion from a 0d/1d analysis to complete 3d-cfd engine simulations. *Energies*, 17(22):5543, November 2024. ISSN 1996-1073. doi: 10.3390/en17225543. URL http://dx.doi.org/10.3390/en17225543.

[40] Alfio Quarteroni, Paola Gervasio, and Francesco Regazzoni. Combining physics-based and data-driven models: advancing the frontiers of research with scientific machine learning. *Mathematical Models and Methods in Applied Sciences*, 35(04):905–1071, March 2025. ISSN 1793-6314. doi: 10.1142/s0218202525500125. URL http://dx.doi.org/10.1142/S0218202525500125.

[41] Dimitrios C. Rakopoulos and Evangelos Giakoumis. Review of thermodynamic diesel engine simulations under transient operating conditions, 4 2006. URL https://saemobilus.sae.org/content/2006-01-0884.

[42] Xianyu Meng, Xi Li, Jialei Chen, Yongyan Fu, Chu Zhang, Muhammad Shahzad Nazir, and Tian Peng. An innovative nox emissions prediction model based on random forest feature selection and evolutionary reformer. *Processes*, page 107, 1 2025. doi: 10.3390/pr13010107. URL https://doi.org/10.3390/pr13010107.

[43] Andrea Marinoni, Matteo Tamborski, Tarcisio Cerri, Gianluca Montenegro, Gianluca D'Errico, Angelo Onorati, Emanuele Piatti, and Enrico Ernesto Pisoni. 0d/1d thermo-fluid dynamic modeling tools for the simulation of driving cycles and the optimization of ic engine performances and emissions. *Applied Sciences*, 11:8125, 9 2021. doi: 10.3390/app11178125. URL `https://doi.org/10.3390/app11178125`.

[44] Mario Picerno, Sung-Yong Lee, Michal Pasternak, Reddy Siddareddy, Tim Franken, Fabian Mauss, and Jakob Andert. Real-time emission prediction with detailed chemistry under transient conditions for hardware-in-the-loop simulations. *Energies*, page 261, 12 2022. doi: 10.3390/en15010261. URL `https://doi.org/10.3390/en15010261`.

[45] Ruomiao Yang, Yuchao Yan, Xiaoxia Sun, Qifan Wang, Yu Zhang, Jiahong Fu, and Zhentao Liu. An artificial neural network model to predict efficiency and emissions of a gasoline engine. *Processes*, page 204, 1 2022. doi: 10.3390/pr10020204. URL `https://doi.org/10.3390/pr10020204`.

[46] Vaibhav Ahire, Mahesh Shewale, and Ali Razban. A review of the state-of-the-art emission control strategies in modern diesel engines. *Archives of Computational Methods in Engineering*, 1:3, 1 2021. doi: 10.1007/s11831-021-09558-x. URL `https://doi.org/10.1007/s11831-021-09558-x`.

[47] Armin Norouzi, Hamed Heidarifar, Mahdi Shahbakhti, Charles Robert Koch, and Hoseinali Borhan. Model predictive control of internal combustion engines: A review and future directions. *Energies*, 14:6251, 10 2021. doi: 10.3390/en14196251. URL `https://doi.org/10.3390/en14196251`.

[48] Simon Thrane Hansen, Cláudio undefinedngelo Gonçalves Gomes, Masoud Najafi, Torsten Sommer, Matthias Blesken, Irina Zacharias, Oliver Kotte, Pierre R. Mai, Klaus Schuch, Karl Wernersson, Christian Bertsch, Torsten Blochwitz, and Andreas Junghanns. The fmi 3.0 standard interface for clocked and scheduled simulations. *Electronics*, 11 (21):3635, November 2022. ISSN 2079-9292. doi: 10.3390/electronics11213635. URL `http://dx.doi.org/10.3390/electronics11213635`.

[49] Jingxi Zhang, Carsten Ellwein, Malte Heithoff, Judith Michael, and Andreas Wortmann. Digital twin and the asset administration shell: An analysis of the three types of aass and their feasibility for digital twin engineering. *Software and Systems Modeling*, 24(3): 771–793, January 2025. ISSN 1619-1374. doi: 10.1007/s10270-024-01255-0. URL `http://dx.doi.org/10.1007/s10270-024-01255-0`.

[50] Thomas Guilbaud, Carlo Fiorina, Stefano Lorenzi, Alessandro Scolaro, Federico Carminati, Donovan Maire, and Andreas Pautz. Investigating the functional mock-up interface

as a coupling framework for the multi-fidelity analysis of nuclear reactors. *Progress in Nuclear Energy*, 169:105022, April 2024. ISSN 0149-1970. doi: 10.1016/j.pnucene.2023.105022. URL `http://dx.doi.org/10.1016/j.pnucene.2023.105022`.

[51] Andreas Bergsten and Richard Mikelöv. Evaluating the reliability of fmi co-simulation for validation, 6 2023.

[52] Muhammad Usman Awais, Peter Palensky, Wolfgang Mueller, Edmund Widl, and Atiyah Elsheikh. Distributed hybrid simulation using the hla and the functional mock-up interface. In *IECON 2013 - 39th Annual Conference of the IEEE Industrial Electronics Society*, page 7564–7569. IEEE, November 2013. doi: 10.1109/iecon.2013.6700393. URL `http://dx.doi.org/10.1109/IECON.2013.6700393`.

[53] Jae-Hyuk Kim, Yoon-Seok Lee, Hyun-Jun Kim, and Byung-Moon Han. A new reactive-power sharing scheme for two inverter-based distributed generations with unequal line impedances in islanded microgrids. *Energies*, 10(11):1800, November 2017. ISSN 1996-1073. doi: 10.3390/en10111800. URL `http://dx.doi.org/10.3390/en10111800`.

[54] Jonathan Nibert, Marc Herniter, and Zachariah Chambers. Model-based system design for mil, sil, and hil. *World Electric Vehicle Journal*, 5(4):1121–1130, December 2012. ISSN 2032-6653. doi: 10.3390/wevj5041121. URL `http://dx.doi.org/10.3390/wevj5041121`.

[55] Zoé Magalhães, André Murilo, and Renato V. Lopes. Development and evaluation with mil and hil simulations of a lqr-based upper-level electronic stability control. *Journal of the Brazilian Society of Mechanical Sciences and Engineering*, 41(8), July 2019. ISSN 1806-3691. doi: 10.1007/s40430-019-1808-6. URL `http://dx.doi.org/10.1007/s40430-019-1808-6`.

[56] Bo-Chiuan Chen, Yuh-Yih Wu, Hsien-Chi Tsai, and Bo-Liang Chen. Development of engine model using modulization method for ems verification through mil and hil. In *SAE Technical Paper Series*, ANNUAL. SAE International, April 2014. doi: 10.4271/2014-01-1097. URL `http://dx.doi.org/10.4271/2014-01-1097`.

[57] Yixin Chen, Jeffrey Pfeiffer, and Ken Simpson. Engine plant model development for hil system and application to on-board diagnostic verification. In *SAE Technical Paper Series*, ANNUAL. SAE International, April 2011. doi: 10.4271/2011-01-0457. URL `http://dx.doi.org/10.4271/2011-01-0457`.

[58] José Albeiro Valencia Chica and Adalberto Gabriel Díaz Torres. Evaluation of two strategies nmpc into hil applied to the operation of an internal combustion engine. *International Journal on Interactive Design and Manufacturing (IJIDeM)*, 12(1):355–392, May 2017.

ISSN 1955-2505. doi: 10.1007/s12008-017-0400-5. URL `http://dx.doi.org/10.1007/s12008-017-0400-5`.

[59] Corinna Netzer, Lars Seidel, Michal Pasternak, Christian Klauer, Cathleen Perlman, Frederic Ravet, and Fabian Mauss. Engine knock prediction and evaluation based on detonation theory using a quasi-dimensional stochastic reactor model. In *SAE Technical Paper Series*, ANNUAL. SAE International, March 2017. doi: 10.4271/2017-01-0538. URL `http://dx.doi.org/10.4271/2017-01-0538`.

[60] Tim Franken. *Multi-Objective Optimization of Stochastic Engine Models*. PhD thesis, BTU Cottbus - Senftenberg, Oct 2023. URL `https://opus4.kobv.de/opus4-btu/files/6633/Doktorarbeit_Franken.pdf`.

[61] Tim Franken and Fabian Mauss. Development of methodology for predictive diesel combustion simulation using 0d stochastic reactor model. In *SAE Technical Paper Series*, ANNUAL. SAE International, April 2016. doi: 10.4271/2016-01-0566. URL `http://dx.doi.org/10.4271/2016-01-0566`.

[62] Martin Tunér, Michał Pasternak, Fabian Mauss, and Henry Bensler. A pdf-based model for full cycle simulation of direct injected engines. In *SAE Technical Paper Series*, SFL. SAE International, June 2008. doi: 10.4271/2008-01-1606. URL `http://dx.doi.org/10.4271/2008-01-1606`.

[63] LOGE AB. LOGEsoft, LOGEengine, LOGEcat. `http://www.logesoft.com`, 2024.

[64] Andrea Matrisciano. *Development of an efficient solver for detailed kinetics in reactive flows*. PhD thesis, Chalmers University of Technology, 2021.

[65] Norbert Peters. *Turbulent Combustion*. Cambridge University Press, August 2000. ISBN 9780511612701. doi: 10.1017/cbo9780511612701. URL `http://dx.doi.org/10.1017/CBO9780511612701`.

[66] Hemanth. Kolla, J. W. Rogerson, N. Chakraborty, and N. Swaminathan. Scalar dissipation rate modeling and its validation. *Combustion Science and Technology*, 181(3): 518–535, February 2009. ISSN 1563-521X. doi: 10.1080/00102200802612419. URL `http://dx.doi.org/10.1080/00102200802612419`.

[67] Simon Bjerkborn, Karin Frojd, Cathleen Perlman, and Fabian Mauss. A monte carlo based turbulent flame propagation model for predictive si in-cylinder engine simulations employing detailed chemistry for accurate knock prediction. *SAE International Journal of Engines*, 5(4):1637–1647, September 2012. ISSN 1946-3944. doi: 10.4271/2012-01-1680. URL `http://dx.doi.org/10.4271/2012-01-1680`.

[68] Michal Pasternak, Fabian Mauss, Marc Sens, Michael Riess, Andreas Benz, and Karl Georg Stapf. Gasoline engine simulations using zero-dimensional spark ignition stochastic reactor model and three-dimensional computational fluid dynamics engine model. *International Journal of Engine Research*, 17(1):76–85, December 2015. ISSN 2041-3149. doi: 10.1177/1468087415599859. URL `http://dx.doi.org/10.1177/1468087415599859`.

[69] Christoph Bossung. Turbulenzmodellierung für quasidimensionale motorprozessrechnung, 2017. URL `http://elib.uni-stuttgart.de/handle/11682/9188`.

[70] David C. Wilcox. *Turbulence Modeling for Cfd*. Dcw Industries, 3 edition, January 2006.

[71] Robert L. Curl. Dispersed phase mixing: I. theory and effects in simple reactors. *AIChE Journal*, 9(2):175–181, March 1963. ISSN 1547-5905. doi: 10.1002/aic.690090207. URL `http://dx.doi.org/10.1002/aic.690090207`.

[72] Johannes Janicka, W. Kolbe, and Wolfgang Kollmann. Closure of the transport equation for the probability density funcfion of turbulent scalar fields. *Journal of Non-Equilibrium Thermodynamics*, 4(1), 1979. ISSN 1437-4358. doi: 10.1515/jnet.1979.4.1.47. URL `http://dx.doi.org/10.1515/jnet.1979.4.1.47`.

[73] Michal Pasternak. *Simulation of the diesel engine combustion process using the stochastic reactor model*. Logos Verlag Berlin, Berlin, Germany, September 2016.

[74] Eugen-Georg Woschni. A universally applicable equation for the instantaneous heat transfer coefficient in the internal combustion engine. In *SAE Technical Paper Series*, GMDMEETING. SAE International, February 1967. doi: 10.4271/670931. URL `http://dx.doi.org/10.4271/670931`.

[75] European Commission. Regulation (EU) 2017/1151 on Emission Type Approval of Light Passenger and Commercial Vehicles. `https://eur-lex.europa.eu/legal-content/EN/TXT/?uri=CELEX:32017R1151`, 2017. Official Journal of the European Union.

[76] Peter Mock, John German, Anup Bandivadekar, and Ineke Riemersma. From Laboratory to Road: A Comparison of Official and "Real-World" Fuel Consumption and CO2 Values for Cars in Europe and the United States. Technical report, International Council on Clean Transportation (ICCT), 2014. URL `https://theicct.org/publication/from-laboratory-to-road-2014-update`.

[77] U.S. Environmental Protection Agency. Epa nonregulatory nonroad duty cycles. `https://www.epa.gov/moves/epa-nonregulatory-nonroad-duty-cycles`, 2025. Accessed July 2025.

[78] Evangelos G. Giakoumis. Non-road engines. In *Driving and Engine Cycles*, pages 285–314. Springer, 2016. doi: 10.1007/978-3-319-49034-2_5. URL `https://link.springer.com/chapter/10.1007/978-3-319-49034-2_5`.

[79] Andreas Mayer, Andreas Ulrich, Jacek Czerwinski, Norbert Heeb, and Markus Kasper. Emission Control for Non-Road Diesel Engines in the EU and USA. In *SAE Technical Paper Series*. SAE International, 2008. doi: 10.4271/2008-01-1804.

[80] Andrea Massimo Marinoni, Angelo Onorati, Giacomo Manca Di Villahermosa, and Simon Langridge. Real driving cycle simulation of a hybrid bus by means of a co-simulation tool for the prediction of performance and emissions. *Energies*, 16(12):4736, June 2023. ISSN 1996-1073. doi: 10.3390/en16124736. URL `http://dx.doi.org/10.3390/en16124736`.

[81] Lijun Hao, Wei Chen, Lei Li, Jianwei Tan, Xin Wang, Hang Yin, Yan Ding, and Yunshan Ge. Modeling and predicting low-speed vehicle emissions as a function of driving kinematics. *Journal of Environmental Sciences*, pages 109–117, 8 2016. doi: 10.1016/j.jes.2016.05.037.

[82] Navid Balazadeh, Sandeep Munshi, Mahdi Shahbakhti, and Gordon McTaggart-Cowan. Predicting transient performance of a heavy-duty gaseous-fuelled engine using combined phenomenological and machine learning models. *International J of Engine Research*, 26(7):1070–1087, 7 2025. doi: 10.1177/14680874241305732.

[83] XiaoHang Fang, Fengyu Zhong, Nick Papaioannou, Martin H Davy, and Felix CP Leach. Artificial neural network (ann) assisted prediction of transient no_x emissions from a high-speed direct-injection (hsdi) diesel engine. *International J of Engine Research*, 23(7): 1201–1212, 2022. doi: 10.1177/14680874211013254.

[84] Zhiming Gao, Jim Conklin, Stuart Daw, and Veerathu Chakravarthy. A proposed methodology for estimating transient engine-out temperature and emissions from steady-state maps. *Proceedings of the Institution of Mechanical Engineers, Part D: Journal of Automobile Engineering*, 223(11):1417–1430, 2009. doi: 10.1243/14680874JER05609.

[85] Newton Paciornik, Michael Gillenwater, Riccardo De Lauretis, Daniela Romano, Suvi Monni, and Stephen M. Ogle. 2019 refinement to the 2006 ipcc guidelines for national greenhouse gas inventories: Chapter 3 – uncertainties. `https://www.ipcc-nggip.iges.or.jp/public/2019rf/pdf/1_Volume1/19R_V1_Ch03_Uncertainties.pdf`, 2019. IPCC Task Force on National Greenhouse Gas Inventories.

[86] Monica Crippa, Diego Guizzardi, Federico Pagani, and et al. Ghg emissions of all world countries – 2022 report. `https://edgar.jrc.ec.europa.eu/report_2022`, 2022. Emissions Database for Global Atmospheric Research (EDGAR), European Commission.

[87] Momir Sjeric, Darko Kozarac, and Ormuz Krunoslav. Cycle-simulation turbulence modelling of ic engines. *International Journal of Automotive Technology*, 17(1):51–61, 2016. doi: 10.1007/s12239-016-0004-2.

[88] François Chollet. Keras. `https://keras.io`, 2015.

[89] Martín Abadi, Ashish Agarwal, Paul Barham, Eugene Brevdo, Zhifeng Chen, Craig Citro, Greg S. Corrado, Andy Davis, Jeffrey Dean, Matthieu Devin, Sanjay Ghemawat, Ian Goodfellow, Andrew Harp, Geoffrey Irving, Michael Isard, Yangqing Jia, Rafal Jozefowicz, Lukasz Kaiser, Manjunath Kudlur, Josh Levenberg, Dan Mane, Rajat Monga, Sherry Moore, Derek Murray, Chris Olah, Mike Schuster, Jonathon Shlens, Benoit Steiner, Ilya Sutskever, Kunal Talwar, Paul Tucker, Vincent Vanhoucke, Vijay Vasudevan, Fernanda Viégas, Oriol Vinyals, Pete Warden, Martin Wattenberg, Martin Wicke, Yuan Yu, and Xiaoqiang Zheng. Tensorflow: Large-scale machine learning on heterogeneous systems. `https://www.tensorflow.org/`, 2015. Software available from tensorflow.org.

[90] Fabian Pedregosa, Gael Varoquaux, Alexandre Gramfort, Vincent Michel, Bertrand Thirion, and Olivier Grisel. Scikit-learn: Machine learning in Python. *Journal of Machine Learning Research*, 12:2825–2830, 2011.

[91] Diederik P. Kingma and Jimmy Ba. Adam: A method for stochastic optimization, 2014. URL `https://arxiv.org/abs/1412.6980`.

[92] Johannes Oder. Verbrennungssteuerung eines cng-di-motors mittels hochlastabgasrückführung, 2021. URL `https://opendata.uni-halle.de//handle/1981185920/64956`.

[93] AiF Project, Funding Number 20756 BR, 2022. Simulation of the cold start behaviour of exhaust aftertreatment systems for natural gas engines, 2022. URL `https://opendata.uni-halle.de//handle/1981185920/64956`.

[94] Krishna P. Shrestha, Sven Eckart, Ayman M. Elbaz, Binod R. Giri, Chris Fritsche, Lars Seidel, William L. Roberts, Hartmut Krause, and Fabian Mauss. A comprehensive kinetic model for dimethyl ether and dimethoxymethane oxidation and no interaction utilizing experimental laminar flame speed measurements at elevated pressure and temperature. *Combustion and Flame*, 218:57–74, August 2020. ISSN 0010-2180. doi: 10.1016/j.combustflame.2020.04.016. URL `http://dx.doi.org/10.1016/j.combustflame.2020.04.016`.

[95] Tim Franken, Fabian Mauss, Lars Seidel, Maike Sophie Gern, Malte Kauf, Andrea Matrisciano, and Andre Casal Kulzer. Gasoline engine performance simulation of water injection and low-pressure exhaust gas recirculation using tabulated chemistry. *International Journal of Engine Research*, 21(10):1857–1877, 2020. doi: 10.1177/1468087420933124. URL `https://doi.org/10.1177/1468087420933124`.

[96] Andrea Matrisciano, Michal Pasternak, Xiaoxiao Wang, Oleksiy Antoshkiv, Fabian Mauss, and Peter Berg. On the performance of biodiesel blends - experimental data and simulations using a stochastic fuel test bench. *SAE Technical Paper*, 4 2014. doi: 10.4271/2014-01-1115. URL `https://doi.org/10.4271/2014-01-1115`.

[97] Alessio Dulbecco, Stephane Richard, Olivier Laget, and Philippe Aubret. Development of a quasi-dimensional k-k turbulence model for direct injection spark ignition (disi) engines based on the formal reduction of a 3d cfd approach. In *SAE Technical Paper Series*, FFL. SAE International, October 2016. doi: 10.4271/2016-01-2229. URL `http://dx.doi.org/10.4271/2016-01-2229`.

[98] Shuofeng Wang, Changwei Ji, Bo Zhang, and Xiaolong Liu. Lean burn performance of a hydrogen-blended gasoline engine at the wide open throttle condition. *Applied Energy*, 136:43–50, December 2014. ISSN 0306-2619. doi: 10.1016/j.apenergy.2014.09.042. URL `http://dx.doi.org/10.1016/j.apenergy.2014.09.042`.

[99] Sascha Prehn, Volker Wichmann, Horst Harndorf, and Wolfgang Beberdick. *Development and investigation of a gas engine for agricultural machinery*, page 64–76. Springer Fachmedien Wiesbaden, 2018. ISBN 9783658215835. doi: 10.1007/978-3-658-21583-5_5. URL `http://dx.doi.org/10.1007/978-3-658-21583-5_5`.

[100] Sascha Prehn, Volker Wichmann, Marcel Kaspera, Tony David Lassak, and Horst Harndorf. Entwicklung und Untersuchung eines Gasmotors für Landmaschinen – Phase 1. `https://opac.dbu.de/ab/DBU-Abschlussbericht-AZ-29980-01.pdf`, 2015. [Accessed 11-08-2025].

[101] Reddy Babu Siddareddy, Tim Franken, Larisa Leon de Syniawa, Michal Pasternak, Sascha Prehn, Bert Buchholz, and Fabian Mauss. Simulation of cng engine in agriculture vehicles. part 1: Prediction of cold start engine-out emissions using tabulated chemistry and stochastic reactor model. In *SAE Technical Paper Series*, ICE2023. SAE International, August 2023. doi: 10.4271/2023-24-0006. URL `http://dx.doi.org/10.4271/2023-24-0006`.

[102] Torsten Blochwitz, Martin Otter, Martin Arnold, Constanze Bausch, Christoph Clauß, Hilding Elmqvist, Andreas Junghanns, Jakob Mauss, Manuel Monteiro, Thomas Neidhold, Dietmar Neumerkel, Hans Olsson, Jörg-Volker Peetz, and Susann Wolf. The

functional mockup interface for tool independent exchange of simulation models. In *Proceedings of the 8th International Modelica Conference*, pages 105–114, 03 2011. ISBN 978-91-7393-096-3. doi: 10.3384/ecp11063105.

[103] Michał Pasternak, Reddy Babu Siddareddy, Larisa León de Syniawa, Vivien Guenther, Mario Picerno, Jakob Andert, Tim Franken, Fabian Mauss, and Wojciech Adamczyk. *Plant Modelling of Engine and Aftertreatment Systems for X-in-the-Loop Simulations with Detailed Chemistry*, page 151–163. Springer Nature Switzerland, November 2024. ISBN 9783031776274. doi: 10.1007/978-3-031-77627-4_14. URL `http://dx.doi.org/10.1007/978-3-031-77627-4_14`.

[104] Larisa Leon de Syniawa, Reddy Babu Siddareddy, Johannes Oder, Tim Franken, Vivien Guenther, Hermann Rottengruber, and Fabian Mauss. Real-time simulation of cng engine and after-treatment system cold start part 2: Tail-pipe emissions prediction using a detailed chemistry based moc model, 4 2023.

[105] ACTIVATE. Ammonia as carbon free fuel for internal combustion engine driven agricultural vehicle, 2024. URL `https://ammoniaengine.org`.

[106] Junhua Li, Ronghai Zhu, Yisun Cheng, Christine K. Lambert, and Ralph T. Yang. Mechanism of propene poisoning on fe-zsm-5 for selective catalytic reduction of nox with ammonia. *Environmental Science amp; Technology*, 44(5):1799–1805, February 2010. ISSN 1520-5851. doi: 10.1021/es903576d. URL `http://dx.doi.org/10.1021/es903576d`.